Organic Electronic Devices for Sensing and Imaging Applications

by

Kwang Hyup An

A dissertation submitted in partial fulfillment
of the requirements for the degree of
Doctor of Philosophy
(Mechanical Engineering)
in The University of Michigan
2009

Dissertation Committee:

Assistant Professor Kevin P. Pipe, Co-Chair
Assistant Professor Max Shtein, Co-Chair
Associate Professor Jinsang Kim
Associate Professor Katsuo Kurabayashi

To my Lord, Jesus Christ

And

To my beloved wife, Hyunjin

ACKNOWLEGEMENTS

For the five years in Ann Arbor, many people have helped me in continuing and finishing my studies, both physically and mentally. Foremost, I would like to thank my advisors, Kevin Pipe and Max Shtein, for introducing me to the great topic of organic electronics that I had never imagined before; for their dedicated and patient guidance; for making slides and giving presentations; and their thoughtful advise and support throughout my dissertation. I would also like to thank my doctoral committee members, Professor Jinsang Kim, for his kind and pertinent discussions, and Katsuo Kurabayashi, for her helpful guidance on my work.

I have enjoyed my time in 2211B G. G. Brown with Abhishek Yadav, Paddy Chan, and Huarui Sun, which actually made my work proceed quickly. We had numberless, invaluable discussions that allowed me to have insight into physics. Gunho Kim, whom recently joined, also contributes to the scholastic atmosphere of the room. I also would like to thank all past and present lab members for making it an enjoyable journey, including Shaurjo Biswas, Mark Hendryx, Yansha Jin, Steve Morris, Denis Nothern, Brendan O'Connor, and Yiying Zhao. Through valuable discussions with Brendan, I could reach decisions that were indispensible to my research; and thanks to Yiying, I could easily transition into research in electronic organics.

There are also many collaborators who gave me practical assistance; Hsien-Yeh Chen helped me coat parylene, Haiping Sun taught me how to use the EMAL equipment, and Sangjo Choi gave me great help in initiating the Dyadic Green's function formulation. I would also like to thank Myungsu Kim, Myungkyu Kang, Sehyun Ahn, and Chelsea Chen. Most of all, Woong Hee Lee and Bong Sup Shim are good friends who shared food, golf ball, and faith, as well as extensively broadening my scientific understanding.

I cannot help but to mention the members of the Korean Presbyterian Church of Ann Arbor, including Paster Sun Myung Rew and many other people who support me with their prayers.

Kayla An, my adorable daughter, started her life with my doctoral study from Fall 2004, and has been filling my heart with endless joy through the whole period of my studies. Jaina An is another delight to me, relieving me of all my stresses. I believe they are great presents from God. Most of all, I appreciate my wife, Hyunjin Lim, for her sacrifice, endless support, and encouragement. I'd like to thank God for bringing her into my life.

Lastly, I want to thank God for giving me a chance to study and allowing me to finish my work. I hope to continue all my work within God's amazing plan, loving God and others.

TABLE OF CONTENTS

LIST OF FIGURES

capping layer thickness and in-plane wave vector (k_x). As the capping layer thickness increases, surface plasmons (near $k_x/2\pi = 4$) at the organic/metal and metal/capping surfaces start to couple, leading to increased electric field strength and efficient energy transfer from decaying excitons. (b) Similar phenomena occur when the metal cathode thickness changes. (c) Energy coupling rates to leaky (①) and surface plasmon modes (②), as a function of capping layer thickness. The energy coupling efficiency between surface plasmons at exterior interface and dye placed near the metal is assumed to be 2%. While the coupling to leaky radiation oscillates with the capping layer thickness because of optical interference effects, the symmetry introduced via the capping layer is responsible for the monotonically increasing of the SPP outcoupling. (d) A similar calculation as a function of cathode metal thickness. The figure of merit characterizes the fraction of energy transferred into cathode SPP modes (②) (versus leaky radiative emission (①) through the cathode). While leaky radiation shows an exponential decay due to metal absorption, coupling to SPP modes shows an optimal point as a result of the two competing mechanism of field resonance and metal absorption. ……...45

Figure 3.5 (a) Three device structures for convenient energy transfer measurement, using an archetypal OLED structure as a common substrate, but observed from the side opposite the substrate (from the top). Device I is a bare OLED, with no capping layer, resulting in an SPP mode that is confined only at the interior metal interface as shown in the (red) electric field (E_z). Devices II and III have a 150 nm thick capping layer of α-NPD, leading to a strong electric field at both interior and exterior surfaces of the metal film (blue color electric field). DCM2, a red-emitting dye, is doped into the α-NPD outer layer with 5% mass ratio for Device II and III. The accurate position of the doped region within the capping layer is shown. While Device II has dye doped region far from the metal electrode, Device III has dye-doped region adjacent to the metal layer. ……47

Figure 3.6 Measurement of energy transfer. a) A photograph of the energy transfer devices deposited onto a common substrate, operating under forward bias, imaged from the top (silver electrode side). The pathways labeled Ⓐ,Ⓑ, and Ⓒ are tied to the light emission through the top of each Device I,II, and III. Pathway Ⓓ is the bottom light emission to the ITO side, which remains essentially constant among the three devices. In Device III, the evanescent SPP fields efficiently couple energy into DCM2 dye through a resonant near-field process, leading to strong dye emission (Ⓒ) – seen as orange light. Device II shows 6-hold enhanced emission of green light (Ⓑ) compared to Device I (Ⓐ). The increased energy content in SPP modes at the exterior metal surface is scattered

LIST OF APPENDICES

ABSTRACT

Organic semiconductor compounds are Van der Waals bonded and can be deposited as thin films onto a variety of substrates without the lattice-matching constraints of conventional covalently-bonded semiconductors, enabling novel device form factors. While electronic devices based on organic materials have an increasing presence in display, lighting, and photovoltaic applications, sensor applications have been relatively unexplored. In fact, organic semiconductors offer unique properties which make them particularly desirable for sensing and imaging and which are impossible or difficult to realize in inorganic semiconductors. This work focuses on developing novel organic-based devices that function as imaging tools, including integrated surface plasmon-emitting devices, active organic devices integrated with scanning probe cantilevers, and tunable organic photodetectors. The fundamental physical mechanisms for excitonic energy coupling in thin film heterostructures, which enable the operation of these devices, are discussed in detail.

Although thin film organic semiconductors typically have a larger resistivity than inorganic semiconductors, their lower refractive index provides several electrical and optical advantages for device design. Furthermore, the large binding energy of excitons in organic materials (on the order of 1eV) results in relatively long lifetimes, which can facilitate efficiently coupling of exciton energy to surface plasmons at a nearby metal interface. This thesis describes how to utilize the strong excitonic energy

coupling to surface plasmons in thin-film organic optoelectronic devices to transfer energy across a thick metal film, from electrically pumped molecular excitons on one side to molecular excitons on the opposite side. This demonstration and analysis of plasmon-mediated energy transfer from electrically pumped dipoles represents a significant advancement from prior work in which plasmon-mediated exciton coupling was demonstrated only for optically-pumped excitons and which is far less suitable for use in integrated optoelectronic devices. The observed exciton transfer mechanism can be applied to, for example, a solid-state electrically-pumped sensor with nanoscale resolution, or multi-modal imaging of nanomaterials and biological systems. Surface plasmon resonances in electrically-pumped devices can potentially be engineered to create sensitive biochemical reaction detectors, based on the inherent electrical sensitivity of the devices to the exciton decay rate (which in turn responds to nearby chemical species).

In order to increase the spatial resolution of organic-based imaging devices, the fabrication of organic LEDs and organic photodetectors of submicron size on the tips of scanning probe cantilevers is described. The small working area is defined by focused ion beam milling, and the devices are used for simultaneous high-resolution optical imaging and topography measurements. These probe designs serve as a high-resolution platform for applying various energy transfer mechanisms to sensor and energy conversion device applications.

The high optical density of organic materials due to their narrow excitonic energy transition levels enables a thin photodetector with high quantum efficiency. An organic photodetector with spectral response tunable across the visible spectrum is demonstrated by means of engineering the optical microcavity within the device. Such

mechanically flexible and tunable photodetectors are expected to find applications in microfluidics and portable sensing devices, as well as colorimeters. Combining the tunable organic photodetector with the above scanning probe platform, simultaneous fluorescence and topography microscopy can potentially be achieved with high spatial resolution, with numerous applications in cell biology.

The innovative design and fabrication methods for organic materials and devices described here have significant promise for the fields of materials science, chemistry, and biology. The results of this work indicate that organic electronics offer a convenient and useful platform for sensing and imaging applications. The physics of thin film devices, including excitonic energy transfer, waveguided mode control, and microcavity effects are anticipated to also be very helpful in developing and improving displays, solid-state lighting, solar cells, and other devices.

CHAPTER 1

INTRODUCTION

1.1 Optical sensing and microscopy

The interactions of chemical and biochemical species are of great importance in the life sciences, where understanding of reactions is important for diagnostic and therapeutic applications. To observe these interactions, investigators have applied a variety of microscopic techniques; among these, fluorescence microscopy is widely used by chemists, biologists, and materials scientists.

To observe chemical interactions on the small length scales over which they occur in living systems such as cells, conventional microscopy is not suitable, since its resolution is set by the diffraction limit. For visible wavelength illumination, this corresponds to a resolution of several hundred nanometers – much larger than typical cell structures such as ribosomes (~20 nm or membrane pores that mediate intercellular transport (~10-100 nm). Several techniques have been developed to overcome the diffraction limit, such as a total internal reflection fluorescence microscopy (TIRFM) [7], surface plasmon microscopy (SPM) [84], and scanning near-field optical microscopy (SNOM) [12]. Total internal reflection microscopy uses a prism to bend light into high incident angles in a glass slide underneath a sample, creating an evanescent field that is highly concentrated in the sample near the glass surface. Because this field is composed of evanescent (rather than propagating) components, the field excites only the parts a

sample that are within 100 nm of the sample-substrate interface, resulting in nanoscale resolution in the direction normal to the surface. In TIRFM (**Fig. 1.1**), the evanescent field is used to excite fluorescent markers near a sample's surface that characterize molecular events such as cell adhesion, binding of cells, and membrane dynamics. TIRFM can be used to observe the fluorescence of a single molecule, making it an important tool for biophysics and quantitative biology.

Surface plasmon microscopy also uses total internal reflection to generate evanescent fields for high spatial resolution, but additionally utilizes a thin metal film under the sample to excite surface plasmons. Surface plasmons are collective fluctuation in electron density at a metal-dielectric interface, and the wave propagates along the metal-dielectric interface with the field highly confined near the interface. A recent study on surface plasmon microscopy [95] has shown that the effective refractive index at the interface can be as large as 102 near the surface plasmon resonance frequency, resulting in nanometer scale resolution. Considering Abbe's diffraction limit of resolvable feature size of $\lambda/2n_{eff}$ [14]), the result obtained by Smolyaninov [95] and co-workers (50 nm resolution) is not surprising.

Another type of microscopy that can surpass the diffraction limit to achieve nanometer scale spatial resolution is scanning near-field optical microscopy (SNOM), in which an aperture-based [12] or apertureless [109] probe interacts with a sample through a volume of space that is smaller than the incident light wavelength in all three dimensions. However, the long distance of delivery of light to the probe tip makes the system complex and expensive. The optical loss in metal cladding of aperture tip makes a heating problem, limiting the optical power of the probe and restraining the signal intensity. Furthermore, the signal detection far from the tip gives a low signal-to-noise

ratio (SNR), necessitating a lock-in amplifier.

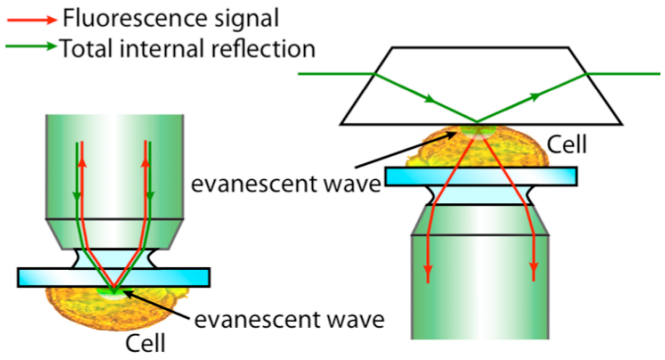

Figure 1.1 Two configurations for conventional total internal reflection fluorescence microscopy (TIRFM). Green lines indicate the excitation light that experiences total internal reflection at the glass-sample interface. Red lines show the detected fluorescence signal from the bio molecules.

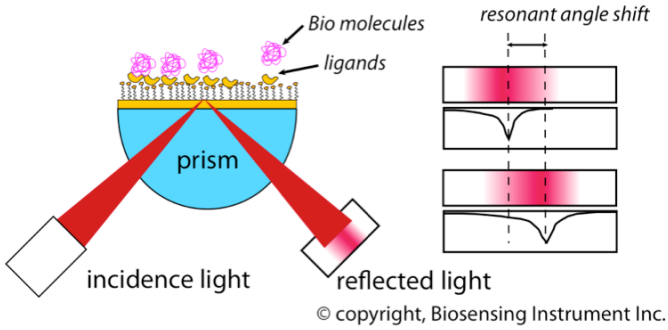

Figure 1.2 Conventional reflection measurement setup for surface plasmon resonance sensor.

There are other types of detectors capable of high spatial resolution that do not need fluorescent labels such fluorescence dyes for staining biomaterials. A surface-plasmon resonance (SPR) detector is a widely used label-free sensing tool for sensing bio- and chemical-reactions. Surface plasmon resonance is very sensitive to local changes in both refractive index and thickness (such as occur during binding events in the sample), leading to measurable changes in reflected light intensity during bio- and chemical-reactions. **Figure 1.2** schematically illustrates the conventional SPR detection scheme, where several optical components and a two-dimensional detector are used. When bio

molecules react with the ligands that are attached to metal surface, not only an effective refractive index of the part above the metal film, but also the thickness of the high index material on the metal increase. In consequence, the resonance condition for the surface plasmon changes. This altered condition can be measurable through the reflection signal where the dip in the reflection curves on the two-dimensional detector is altered as shown in **Fig. 1.2**.

However, the complex and bulky optical components involved in conventional SPR detectors (e.g. light source, lenses, filters, and photodetectors) considerably increase system cost and prevent system miniaturization. In the thesis, we will describe my contributions to the state of the art in high-resolution microscopy and sensing techniques and tools, utilizing organic electronic materials.

1.2 Organic optoelectronic devices, their advantages for sensing & microscopy

The mechanical, chemical, electrical, and optical properties of thin film organic semiconductors provide unique advantages for integrated sensing and microscopy. Significant progress in devices such as organic light emitting devices (OLEDs) and organic solar cells has been made in recent years following the first demonstration of a heterojunction OLED by Tang and VanSlyke [100] and the first demonstration of a 1% efficient, bi-layer organic solar cell by Tang [99].

Organic thin films are based on Van der Waals-bonded molecular organic compounds and can be deposited onto a variety of substrates without the lattice-matching constraints (or brittleness) of conventional covalently-bonded semiconductors. There exists a large library of organic materials with highly tuned electronic and optical properties; this library is continually expanding as researchers synthesize new materials

with tuned absorption, emission, and carrier transport properties for solar cell, lighting, and transistor applications [86].

Although organic semiconductors typically have much larger resistivity than inorganic semiconductors, their low refractive index provides several advantages in electrical and optical properties. The large binding energy of excitons in organic materials (on the order of 1 eV) results in relatively long lifetimes, which can facilitate efficient coupling of exciton energy to surface plasmons at a nearby metal interface. The various possible exciton-exciton and exciton-plasmon coupling mechanisms lend themselves to many useful applications in lighting and energy harvesting devices, as well as electrically pumped sensors described in this work. Further, because optical absorption is closely tied to the excitonic transition, the optical density of many organic semiconductors is very high and spectrally narrow (e.g. a typical absorption coefficient is 10^5 cm^{-1}), facilitating selective and sensitive detection.

The most commercially developed organic devices are OLEDs, which are used for flat panel and mobile display applications and solid-state lighting (SSL). OLEDs offer superior color quality compared to other SSL technologies, as well as competitive power efficiency, mechanical flexibility, and the potential for low-cost fabrication over large (m^2) areas. White OLED efficiencies of 90 lm/W have recently been demonstrated [82] using a carefully selected emitting layer with a high-index substrate and periodic outcoupling structures, overcoming fluorescent tube efficiency of 60-70 lm/W. Alternatively, forward-biased organic heterostructure devices can be engineered to strongly couple radiating dipole energy to surface plasmon modes in the metal electrodes. An organic plasmon-emitting diode similar in structure to an OLED was recently demonstrated [48]. As discussed in later chapters, such devices offer the potential for

controlled interaction with a sample through resonant plasmon-mediated energy transfer.

Organic photovoltaic (OPV) devices represent another large area of organic device research in which significant advancements have been made. OPVs offer the potential of low cost device fabrication over large areas, but are not yet cost-competitive with inorganic technologies due to low conversion efficiencies. A power efficiency of 5.6% was recently reported for a polymer-based solar cell in a tandem configuration [46], and 6% was claimed for a small molecule based solar cell by Heliatec Inc. (Germany).

Organic photodetectors (OPDs) [78][80] have also received attention for applications such as image scanners [60], artificial eyes [105], and microfluidic sensors [40][71]. With the advantage of device flexibility, easy integration ability, and low cost materials, OPDs are broadening their applications, focusing the re-searches in high speed and high sensitivity devices. However, there are only a few studies on achieving wavelength selectivity which is quite useful for fluorescence detectors and image sensors.

1.3 The scope of our work

Making use of the above advantages of organic molecules, we can extend the applications of organic electronics to the sensing and imaging applications, improving the existing optical microscopy systems and sensing tools. In this regard, we have developed an excitonic energy transfer device, an integrated active organic scanning probe for near-field optical microscopy, and a tunable photodetector.

An excitonic energy transfer device is useful for illuminating the fluorescence dye only adjacent (within 100 nm) of a metal surface, which is similar to the principle of TIRFM. However, in the present work, the excitonic energy transfer device is based on a device in which energy is transferred from electrically pumped excitons across a thick

metal film to the opposite side via surface plasmon coupling. This represents a significant advancement over prior work, in which the plasmon-mediated coupling was demonstrated only for optically pumped excitons [4] and which therefore was less suitable for use in integrated electronic devices. The device described here can potentially enable fluorescence microscopy of biological samples with nanometer depth resolution through surface plasmon coupling [95]. Furthermore, surface plasmon resonances in such an electrically-pumped device can potentially be used to create a biochemical reaction detector based on its inherent electrical measurement of the exciton decay rate (which varies based on the presence of nearby chemical species). Such a device is anticipated to also find use in plasmonics and photonics applications.

To resolve the heating and the low SNR problems in aperture SNOM keeping the high spatial resolution, we demonstrate an electrically-pumped light source of submicrometer dimensions on a scanning probe tip. Generating the light locally instead of delivering light to the end of a pulled fiber or scattering off a metallized probe tip is considerably more efficient, eliminating heating, and considerably reduces the noise due to background illumination. To build an electrically pumped light source on the tip, we take advantage of the ability to deposit organic optoelectronic devices without lattice matching onto non-planar substrates. The small working area is defined by focused ion beam milling, allowing for the demonstrated control of the spatial distribution of the electroluminescent region on the tip in the submicron size regime. This demonstration is in contrast to prior attempts using inorganic semiconductors, subject to growth defects and different deposition conditions. Similarly, organic photodetectors of submicrometer dimensions are fabricated on the tips of scanning probe cantilevers. Placing the light detector directly in the optical near field of the sample has greatly enhanced the SNR of

the optical measurement by orders of magnitude over prior methods, showing simultaneous high-resolution (50 nm) optical imaging and topography. The device has important implications for fluorescence microscopy and excitonic energy transfer probe.

Lastly, the work presented here addresses a growing demand for integrated sens-ing and optical microscopy systems that are portable and efficient. In microfluidic systems used for point-of-care diagnostics, for example, miniaturizing the optical sensing system is known to be a bottleneck [59]. An integrated thin film color detector based on organic materials is one candidate for realizing such a sys-tem. We developed an organic photodetector with spectral response tunable across the visible spectrum by means of engineering the optical microcavity within the device. Such mechanically flexible and tunable photodetectors are expected to be suitable in the micro-fluidics and portable sensing devices, as well as colorimeters. Combining the tunable organic photodetector with the above scanning probe platform, simultaneous fluorescence and topography microscopy can potentially be achieved with high spatial resolution, with numerous applications in cell biology.

The innovative design and fabrication methods for organic materials and devices described here have significant promise for the fields of materials science, chemistry, and biology. The results of the work presented below indicate that, indeed, organic electronics offer a convenient and useful platform for sensing and imaging applications, and themselves represent significant steps in advancing the state of the art in sensing and imaging.

1.4 Organization of the thesis

In Chapter 2, analysis and modeling tools are presented for the design and char-

acterization of organic devices. For an organic LED, classical dipole models are used for optical analysis, where the calculation of electric field and Poynting vector is based on the Dyadic Green's function (DGF) formula. For modeling of electrical charge transport in devices, one-dimensional numerical methods are used to self-consistently solve continuity, drift-diffusion, and Poisson's equations. The developed simulation tools are compared to the experimental data to confirm the validity of the tools.

In Chapter 3, a device architecture is developed that utilizes surface plasmons to resonantly transfer energy from electrically-pumped molecular excitons across a metallic cathode to dye molecules in an external coating. Integrated thin film surface plasmon resonance detector is also presented based on the device in which coupled surface plasmons are excited.

In Chapter 4, an organic photodetector is described that utilizes internal optical spacers and microcavity effects to achieve spectral tuning over the entire visible wavelength range. Potential applications in integrated fluorescence microscopy are discussed.

In Chapters 5 and 6, OLEDs and OPDs deposited on scanning probe cantilevers are demonstrated for enhanced spatial resolution in imaging and sensing applications, as well as the ability to perform simultaneous optical microscopy and topography measurements.

In Chapter 7, the work is summarized and future directions are outlined, including scanning probe microscopy architectures with integrated devices for fluorescence microscopy and direct transfer of exciton energy to/from a sample in a non-radiative process.

CHAPTER 2
MODELING AND ANALYSIS OF ORGANIC OPTOELECTRONIC DEVICES

2.1 Motivation

Nominally, the active sensing devices discussed here comprise organic thin films sandwiched between two electrodes. The sensing mechanisms of interest to this work are based on the complex interactions of molecular excitons, surface plasmon polaritons, and electrical current, facilitated and controlled by the laminar structure of the sensor. To understand their operation in detail, we turn to state-of-the-art optical and electrical modeling approaches. The optical model is based on classical dipole model [21], and Dyadic Green's function [51][20]. It allows the calculation of the decay rate of molecular excitons for any given multi-layer device structure, and its theoretically achievable sensing efficiency. In the electrical model, continuity, drift-diffusion, and Poisson's equations are solved numerically for the specified multi-layer structure, using appropriate boundary conditions and heterojunction interface conditions. For sensors based on organic photovoltaic devices, transfer matrix simulations are used to predict the optical field distribution within the device, from which exciton generation and diffusion equation is solved [78][73] numerically to predict the external quantum efficiency. The models are discussed in detail below, with specific examples of how they are applied to predict and analyze the behavior of the sensors. Importantly, these models are readily applicable to

the analysis of organic optoelectronic devices in general, with applications in flat-panel displays, solar cells, lighting, etc.

2.2 Organic light-emitting device and organic surface-plasmon devices

An archetypal organic light emitting devices (OLED) consists of organic thin films (~100 nm thick) sandwiched between an anode and cathode, injecting holes and electrons, respectively [100]. For devices based on small-molecular organic semiconductors, the active organic layers usually comprise a heterostructure, with separate layers transporting electrons and holes, and in many instances additional layers in which the carriers recombine. Electron-hole recombination inside of the organic film leads to the formation of molecular (Frenkel) excitons, some of which decay radiatively.

The fraction of excitonic energy coupled out of the device as visible light can be predicted by considering in detail the optics of the multi-layer structure. **Figure 2.1** illustrates the various modes that exist in the relatively simple OLED structure, including leaky (radiation), waveguided light, surface plasmon-polaritons, and other non-radiative mode. For a conventional OLEDs and SSL, the leaky mode is maximized by suppressing the energy coupling to waveguided, surface plasmon, and other non-radiative mode.

Note that the overall thickness of the device layers is on the order of the wavelength of light (or thinner). The rate of exciton decay in the structure above, and the proportion of energy coupled to each mode are thus very sensitive to its dimensions and the positions of the interfaces. In Section 2.2.3, we analyze the behavior of an exciton near a metal interface, which allows us to predict the power coupled into the different modes in the device.

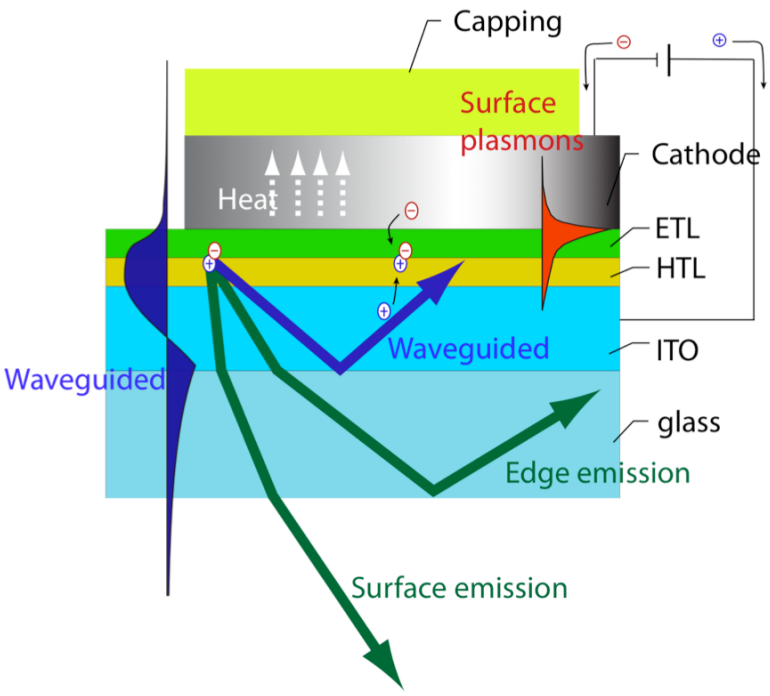

Figure 2.1 An illustration of the different power dissipation modes for electrically generated exciton at the organic heterojunction inside of an OLED [17].

2.2.1 Classical dipole model

It is well established that the electric field emanating from the oscillating dipole has a far-field and a near-field regime. The far-field from a dipole is a spherical outgoing wave ($\sim e^{ikr}/4\pi r$) that can propagate a long distance similar to the waves in TV or radio antenna. On the other side, near-field fades away quickly with $1/r^3$, confining the field near the source within several tens nanometers. It is also established that molecular excitons can be modeled as oscillating point dipoles, and that that the distance from the optically excited molecules to the metal surface affects the decay rate of the excitons [21]. The metal surface acts as a mirror for the electric field emanating from the dipoles, which creates the oscillations via optical interference. The decay rate (inverse of excited state lifetime) therefore has a periodic dependence on the exciton-metal separation for

long-range interaction, while for smaller distances the lifetime decays monotonically to zero, as shown in **Fig. 2.2b**. The increase in the dipole decay rate for small distances is due to the non-radiative transfer of energy from the excited molecule to the metal in the near-field. The abrupt change in decay rate of excited molecules when they are close to the interface is caused by the coupling of near-field with the interface (**Fig. 2.2b**).

In a bilayer OLED structure, similar mechanisms occur. The Frenkel excitons are small (e.g. ~1 nm across), and can be approximated as point-like electric dipoles, while the layers themselves comprise an optical microcavity. If one of the electrodes is ITO, a conventional anode material, the optical microcavity is said to be weak [17]; if both electrodes are metallic, the optical microcavity is said to be strong. In either case, the power dissipation of excitonic energy is affected by the microcavity structure, affecting the balance between power coupled to waveguided, surface plasmon polariton, and other non-radiative modes.

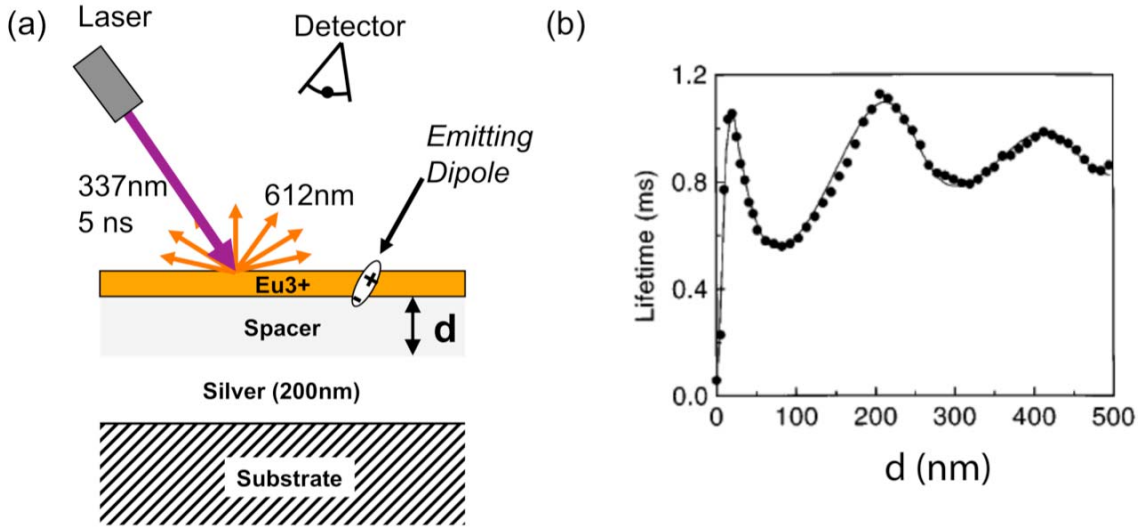

Figure 2.2 Decay rate of dipoles in Eu3+ shows oscillation as the spacer thickness d increases, where the excitons (dipoles) are optically created by 337 nm UV light [21].

Considerable theoretical work [21][31] has been done in studying how the decay rate of an exciton is modified by the presence of a metal surface or adjacent interfaces. A convenient and successful approach is to treat the emitting molecule as a classical dipole oscillator near a partially absorbing and partially reflecting surface, described by:

$$\ddot{\mu} + \omega^2 \mu = \frac{e^2}{m} E_R - b_0 \dot{\mu} \tag{2.1}$$

where ω is the oscillation frequency in the absence of all damping, m is the effective mass of the dipole, E_R is the reflected field at the dipole position, b_0 is the damping constant (inverse lifetime) in the absence of interfaces. The dipole moment μ and the reflected field E_R oscillate at the same frequency,

$$\mu = \mu_0 e^{-i(\omega+\Delta\omega)} e^{-bt/2} \tag{2.2}$$

$$E_R = E_0 e^{-i(\omega+\Delta\omega)} e^{-bt/2} \tag{2.3}$$

where $\Delta\omega$ and b are the frequency shift and the lifetime, respectively, in the presence of the adjacent interfaces. Considering that b^2 and the magnitude of $(e^2/\mu_0 m)E_0$ are negligible compared to ω^2, Eq. (2.1) can be rearranged using Eqs. (2.2) and (2.3) to give:

$$b = \frac{e^2 k_s^3}{6\pi m \omega \varepsilon}\left[1 + \frac{3q\varepsilon}{2p_0 k_s^3}\mathrm{Im}(E_0)\right] \tag{2.4}$$

where the expression in front of the bracket is the intrinsic decay rate of dipole in vacuum, E_0 is magnitude of the electric field at the dipole position, e is the electron charge, ε is the dielectric constant of the emitting layer, p_0 is the dipole moment, and k_s is the wave vector in emitting layer. The calculation of the decay rate of dipoles near interfaces is now simplified to a calculation of the electric field (E_0) at the location of the

dipole. Note that the derivation assumed that the incident wave is a plane wave. The effect of the multilayer structure can be treated as a single interface problem by calculating the effective reflection and transmission coefficients using transfer matrix approach (discussed in detail in [103]). Each plane wave is then characterized by a normalized in-plane wave vector u ($=k_x/k_0$; k_0 is wave vector in air), which is parallel to the interface.

The electric field distribution in the emissive region can be calculated in several ways: 1) using the conventional transfer matrix approach, 2) using the Hertz vector method, and 3) using Dyadic Green's function (DGF). In this study, the Hertz vector and the Dyadic Green's function approaches were utilized, producing similar results for the decay rate. The DGF method is considerably more involved, but is better suited for subsequent calculations of power flow in the entire structure, by computing the Poynting vector, which allows one to calculate the energy transfer rate for both far-field interaction and the Förster energy transfer process. The DGF method is presented in Section 2.2.2, while the Hertz vector method is described in more detail in [103].

2.2.2 Dyadic Green's function

The formulation of Dyadic Green's function is based on the treatments by [51] and Celebi [20] for multilayer thin film structures. The electric field due to an oscillating current is expressed by:

$$E(R) = i\omega\mu_0 \int G(R \mid R') \cdot J(R') d^3R' \tag{2.5}$$

where μ_0 is the magnetic permeability, $J(R')$ is the oscillation current source, and $G(R|R')$ is the Dyadic Green's function. The formulation of DGF is well established for a

multilayer stack [51], and Green's function is expressed by eigenfunctions in cylindrical coordinates:

$$M_{\substack{e\\o}n\kappa}(h) = e^{ihz}\left[\mp\frac{nJ_n(\kappa r)}{r}\begin{matrix}\sin\\\cos\end{matrix}n\phi\hat{r} - \frac{\partial J_n(\kappa r)}{\partial r}\begin{matrix}\cos\\\sin\end{matrix}n\phi\hat{\phi}\right] \tag{2.6}$$

$$N_{\substack{e\\o}n\kappa}(h) = \frac{e^{ihz}}{k_j}\left[ih\frac{\partial J_n(\kappa r)}{\partial r}\begin{matrix}\cos\\\sin\end{matrix}n\phi\hat{r} \mp inh\frac{J_n(\kappa r)}{r}\begin{matrix}\sin\\\cos\end{matrix}n\phi\hat{\phi} + \kappa^2 J_n(\kappa r)\begin{matrix}\cos\\\sin\end{matrix}n\phi\hat{z}\right] \tag{2.7}$$

where *M*, *N* is two eigenfunctions, *j* is the layer index, κ and *h* is parallel and perpendicular component of wavevector, and J_n is a Bessel function of first type of order *n*. Even and odd eigenfunctions are designated by subscripts *e* and *o*. The Green's function can be expressed now by the eigenfunctions (with the dipole source placed at *z = 0)*:

$$G_0(R\,|\,R') = \frac{i}{4\pi}\int_0^\infty d\kappa \sum_{\substack{n=0\\t=e,o}}^{\infty}\frac{2-\delta_{n0}}{\kappa h_s}\begin{cases}\left[M_{tn\kappa}(h_s)M'_{tnk}(-h_s) + N_{tn\kappa}(h_s)N'_{tnk}(-h_s)\right] & z \geq 0\\ \left[M_{tn\kappa}(-h_s)M'_{tnk}(h_s) + N_{tn\kappa}(-h_s)N'_{tnk}(h_s)\right] & z \leq 0\end{cases} \tag{2.8}$$

$$G_j(R\,|\,R') = \frac{i}{4\pi}\int_0^\infty d\kappa \sum_{\substack{n=0\\t=e,o}}^{\infty}\frac{2-\delta_{n0}}{\kappa h_s}\begin{bmatrix} c_j M_{tn\kappa}(-h_s)M'_{tnk}(h_s) + f_j N_{tn\kappa}(-h_s)N'_{tnk}(h_s)\\ +c'_j M_{tn\kappa}(h_s)M'_{tnk}(h_s) + f'_j N_{tn\kappa}(h_s)N'_{tnk}(h_s)\\ +a_j M_{tn\kappa}(-h_s)M'_{tnk}(-h_s) + b_j N_{tn\kappa}(-h_s)N'_{tnk}(-h_s)\\ +a'_j M_{tn\kappa}(h_s)M'_{tnk}(-h_s) + b'_j N_{tn\kappa}(h_s)N'_{tnk}(-h_s)\end{bmatrix} \tag{2.9}$$

where the prime denotes sources, *s* is for the source layer, *j* is for the j^{th} layer, and δ is Dirac delta function. The coefficients *c, c', f, f', a, a', b,* and *b'* in each layer should be determined by applying boundary conditions (equation 2.10 and 2.11) at each interface. For a source layer *s*, G_0 and G_j should be added to specify the electric field:

$$\hat{z}\times\left\{G_j(R\,|\,R') + \delta_j^s G_0(R\,|\,R')\right\} = \hat{z}\times\left\{G_{j+1}(R\,|\,R') + \delta_{j+1}^s G_0(R\,|\,R')\right\} \tag{2.10}$$

$$\hat{z}\times\nabla\times\left\{G_j(R\,|\,R')+\delta_j^s G_0(R\,|\,R')\right\}=\hat{z}\times\nabla\times\hat{z}\times\left\{G_{j+1}(R\,|\,R')+\delta_{j+1}^s G_0(R\,|\,R')\right\} \quad (2.11)$$

The detailed solving procedure for these equations is presented in Appendix A. Briefly, for *N+1* layers and *N* interfaces forming a multilayer stack, we have *8N* equations for *8(N+1)* unknowns. However, 4 prime coefficients of the first layer and 4 normal coefficients of the last layer are zero, assuming no incoming waves. So, the *8N* equations can be solved for the *8N* coefficients. The electric field in each layer can be calculated from Eq. 2.5, by inserting the Green's function. Using the calculated electric field distribution and Eq. 2.4, we obtain the decay rate of a dipole placed $z = 0$. For describing randomly oriented dipoles (isotropic dipoles), we calculate the decay rates for parallel and perpendicular dipoles. Taking account of two parallel principal axis and one perpendicular axis, we obtain an averaged isotropic decay rate via: $b_{iso} = b_{\perp}/3 + 2b_{//}/3$. Perpendicular dipoles generate electric field perpendicular to the interface and more easily couple to non-radiative mode. Parallel dipoles, in other hands, have better chance to be coupled to radiation (leaky) mode.

$$\frac{b_{\perp}}{b_0}=1-q+q\left\{1+\frac{3}{2}\mathrm{Re}\left[\int_0^{\infty}d\kappa\,\frac{\kappa^3}{h_s k_s^2}\left(b_s+f_s+b_s'+f_s'\right)\right]\right\} \quad (2.12)$$

$$\frac{b_{//}}{b_0}=1-q+q\left\{1+\frac{3}{4}\mathrm{Re}\left[\int_0^{\infty}d\kappa\,\frac{\kappa}{h_s}\left(c_s+a_s+c_s'+a_s'+\frac{h_s^2}{k_s^2}\left(f_s-b_s-f_s'+b_s'\right)\right)\right]\right\} \quad (2.13)$$

For the energy flow in the device, we used the divergence of the Poynting vector, whose detailed derivation is provided in Appendix A.

$$\int\nabla\cdot S\,dV=\oint S\cdot dA\approx\int S_z\,dA \quad (2.14)$$

The Poynting vector S_z can be expressed with the E-field components in cylindrical coordinates, and with some algebra, we can obtain a final form for the power flow rate for each perpendicular and parallel dipole:

$$\mathrm{Re}\left(\int S_{z,j}^{\perp}{}^{*}\,dA\right)=\frac{3q}{4}\mathrm{Re}\left[\int_0^{\infty}du\,\frac{u^3h_jk_j^*}{|h_s|^2k_s^2k_j}\left(b_s'e^{ih_jz}+f_s'e^{ih_jz}-b_se^{-ih_jz}-f_se^{-ih_jz}\right)\cdot\left(b_s'e^{ih_jz}+f_s'e^{ih_jz}+b_se^{-ih_jz}+f_se^{-ih_jz}\right)^*\right] \quad (2.15)$$

$$\mathrm{Re}\left(\int S_{z,j}^{//}{}^{*}\,dA\right)=\frac{3q}{8}\mathrm{Re}\left[\int_0^{\infty}du\left(\begin{array}{l}\frac{uh_j^*}{|h_s|^2}\left(c_s'e^{ih_jz}+a_s'e^{ih_jz}+c_se^{-ih_jz}+a_se^{-ih_jz}\right)\\ \quad\cdot\left(c_s'e^{ih_jz}+a_s'e^{ih_jz}-c_se^{-ih_jz}-a_se^{-ih_jz}\right)^*\\ +\frac{uh_jk_j^*}{k_s^2k_j}\left(b_s'e^{ih_jz}-f_s'e^{ih_jz}-b_se^{-ih_jz}+f_se^{-ih_jz}\right)\\ \quad\cdot\left(b_s'e^{ih_jz}-f_s'e^{ih_jz}+b_se^{-ih_jz}-f_se^{-ih_jz}\right)^*\end{array}\right)\right] \quad (2.16)$$

2.2.3 Applying the Dyadic Green's function to OLEDs

The decay rate of dipoles and the power flow rate (2.12-2.16) can now be calculated for a conventional organic LED, comprising an electrically pumped optical microcavity to show what is the physical meaning of the results. Consider a device structure described by this layer sequence: Al (45 nm) / α-NPD (50 nm) / Alq_3 (60 nm) / Ag (30 nm). Excitons are created at the α-NPD (50 nm) and Alq_3 interface. **Figure 2.3** shows the calculated dispersion diagram of the decay rate for the device, where we can clearly see the power dissipation modes for a range of wavelength and in-plane wave vectors. The dipole energy decays into free-space modes (i.e. is coupled into air) for $k_x<k_0$ (above the air light-line), meaning that it is a "radiation (leaky) mode." For

$k_0 < k_x < k_{org}$, the dipole energy is trapped in the organic layers by waveguided mode. For $k_x > k_{org}$, most of the energy is coupled to non-radiative modes including surface plasmons. For an Alq_3 light source whose typical emission peak is at 525 nm, the power dissipation rate versus the in-plane k-vector (k_x) is shown in **Fig. 2.3**. The peaks correspond to the leaky, waveguided, and surface plasmon modes; the total power dissipation rate is calculated by integrating the area under the curve.

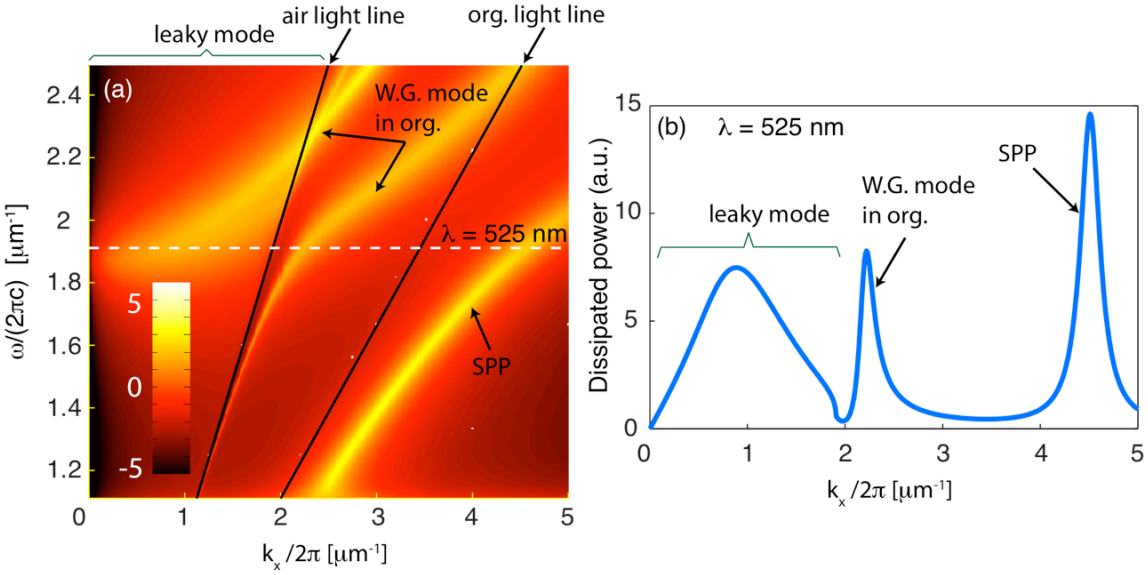

Figure 2.3 (a) The calculated decay rate of dipoles (in log scale) in a simple microcavity structure consisting of: Al (45 nm) / α-NPD (50 nm) / Alq_3 (60 nm) / Ag (30 nm). The light lines in air and in organic medium are drawn to show the leaky mode and waveguided mode regions. On the right-hand side of the diagram, a strong surface plasmon mode at metal interface is apparent. (b) A line-scan indicated by the dashed line in (a), corresponding to the dipole power dissipation rate, plotted against the in-plane wave vector component of the dipole electric field. Integrating the area for each mode, we can calculate the power dissipation ratio of each mode. The dispersion was calculated for an isotropically averaged dipole source corresponding to Alq_3 emission peaked at λ = 525 nm. The dipoles are assumed to be embedded at the organic heterojuction. Peaks correspond to leaky, waveguided, and excitation of SPP modes, as indicated.

The power flow rate calculation is performed for the same organic LED struc-

ture, and shown in **Fig. 2.4**. The diagram is presented as a function of the position and normalized in-plane wave vector for (a) perpendicular dipoles and (b) parallel dipoles. On top of the diagram, the green line corresponds to a quantitative plot of the power flow rate for the radiation is, confirming that most of the leaky mode is coming from the parallel dipole sources. This calculation is particularly useful for maximizing the outcoupling efficiency of an organic LED, since it directly gives the radiation power of the structure. The coupling of perpendicular dipoles to the non-radiative SPP is much stronger than the coupling of parallel ones.

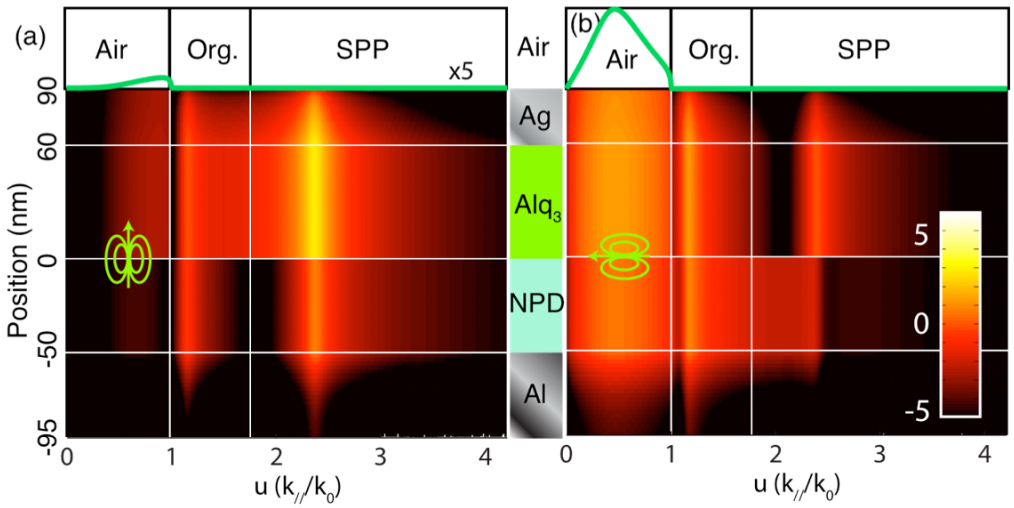

Figure 2.4 A map of the power flow rate (in log scale) as a function of the position and normalized in-plane wave vector for (a) perpendicular dipoles and (b) parallel dipoles. The layer structure is identical to that used for calculating **Fig. 2.3a**. The dipole energy is coupled to air when u ($=k_x/k_0$) < 1, and is trapped in the organic layers when 1 < u < 1.8. If u > 1.8, the energy is dissipated to a non-radiative mode of surface plasmon or to a lossy mode. The graph on top of diagram shows the radiatively coupled energy to air.

For a verification of the simulation model, we compared angle-dependent emission pattern from an OLED. The device structure is Al (60 nm) / Ni (5 nm) / CuPc (3 nm)

/ α-NPD (35 nm) / Alq_3 (45 nm) / LiF (1 nm) / Al (15 nm). The angular emission pattern is calculated based on the power flow rate toward the air, and shown in **Fig. 2.5** as a polar plot. The calculation predicts well the emission pattern of the organic LED, and which is found to be very similar to the Lambert's cosine law (*Lambertian distribution*).

The simulation tool described in this section is particularly useful in designing OLEDs aiming to achieve a high outcoupling efficiency. The structure can be optimized by changing thicknesses and materials, monitoring the power flow toward air or to glass side. The modeling procedure is equally valuable for the quantitative analysis of sensors relying on exciton-plasmon coupling. The energy coupling to surface plasmons, for example, can be maximized for a surface-plasmon emitting device, as described in Chapter 3.

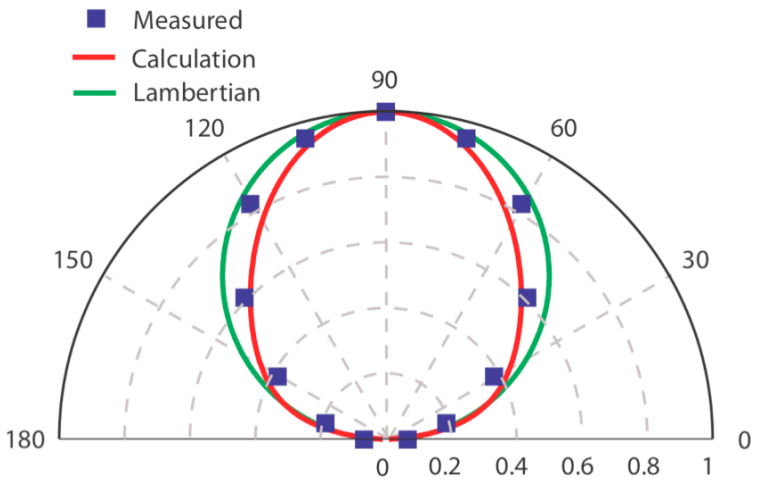

Figure 2.5 A polar plot of normalized light emission intensity for a structure consisting of Al (60 nm) / Ni (5 nm) / CuPc (3 nm) / α-NPD (35 nm) / Alq_3 (45 nm) / LiF (1 nm) / Al (15 nm), with the measured emission intensity superimposed as blue squares. The match between the calculated and measured intensity distribution is good, and close to the Lambertian (cosine) distribution.

2.2.4 Electrical charge transport model

The preceding discussion and analysis pertained to the optical aspects of the energy cascade typically taking place in an OLED or OLED-like device. However, exciton decay typically follows a charge injection and recombination process. In optimizing the overall out-coupling efficiency of an electrically pumped heterostructure device, electrical injection and recombination dynamics must be simulated. In this section, an electrical charge transport simulation is performed for a bi-layer OLED system; the analysis covers charge injection, transport, and space charge effects in the organic material [24][85]. The electrical simulation model gives access to a wide range of information for device evaluation that is not readily attainable by experiments, such as the spatial profiles of the recombination rate, charge densities, electric fields, and exciton distribution within the device.

2.2.4.1 Governing equations

The transport of charges in the organic device is described by time dependent continuity (Eqs. 2.6 and 2.7), drift-diffusion (Eqs. 2.9 and 2.10), and Poisson's (Eq. 2.8) equations:

$$\frac{\partial n}{\partial t} - \frac{1}{e}\frac{\partial J_n}{\partial x} = G - R \tag{2.6}$$

$$\frac{\partial p}{\partial t} + \frac{1}{e}\frac{\partial J_p}{\partial x} = G - R \tag{2.7}$$

$$\frac{\partial E}{\partial x} = \frac{e}{\varepsilon\varepsilon_0}\left(p - n\right) \tag{2.8}$$

where

$$J_n = e\mu_n\left(nE + \frac{kT}{e}\frac{\partial n}{\partial x}\right) \tag{2.9}$$

$$J_p = e\mu_p\left(pE - \frac{kT}{e}\frac{\partial p}{\partial x}\right) \tag{2.10}$$

Here, n, p are the electron and hole density, J_n and J_p are the electron and hole current density, G and R are the carrier generation and recombination rate, μ_n and μ_p are the electron and hole mobility, e is the magnitude of the electron charge, E is the electric field, ε is the static dielectric constant, k is Boltzmann's constant, and T is the temperature. The recombination rate is bimolecular and is expressed by $R = \gamma\, n\, p$, where the recombination coefficient γ is Langevin's coefficient [79], given by:

$$\gamma = \frac{e\left(\mu_n + \mu_p\right)}{\varepsilon\varepsilon_0} \tag{2.11}$$

These equations are spatially discretized using the Scharfetter-Gummel approach [88]; details of the discretization are illustrated in **Fig. 2.6**. The first order differential equations are integrated in time, similar to the transient method. The simulation converges in every time step toward steady state, when the sum of hole and electron current densities (which should be spatially invariant) becomes constant throughout the device.

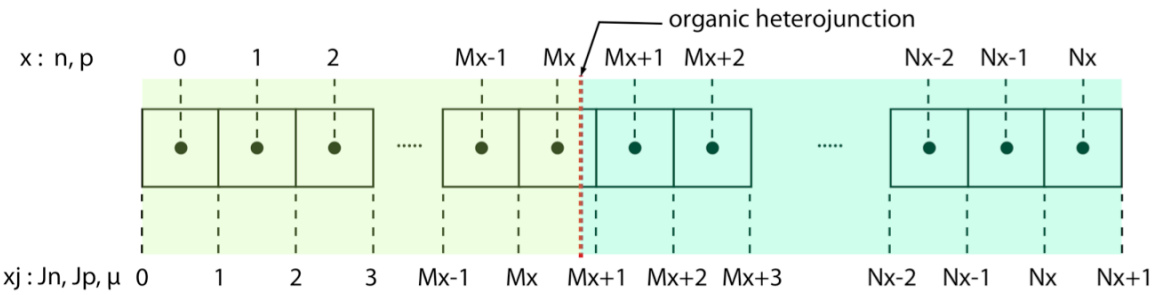

Figure 2.6 Illustration of the discretized cells used for the numerical calculation of charge transport and recombination. The carrier density values are based on the center of the cells, and the current density and electric field values are based on the interfaces.

2.2.4.2 Boundary conditions

For charge injection at the interface between the metal electrode and the organic transport layers, thermionic injection (metal to organic) and recombination (organic to metal) is considered [90]. The recombination process near the interface is analogous to Langevin's bimolecular recombination theory. The electrons and holes recombine when they approach each other and their Coulombic binding energy exceeds *kT*. Considering the thermionic emission and recombination, the current density is expressed by [98] :

$$J = A^{*}T^{2}\exp\left(-\varphi/kT\right) - enS \tag{2.12}$$

where A^{*} is the effective Richardson constant, T is the temperature, φ is the barrier height over which the carriers have to be injected, e is the electron charge, n is the charge density at the contact, and S is the surface recombination velocity. The first term on right hand side gives the injected flux into the organic layer, while the second term describes charge-image recombination at the metal interface (backflow current). From the general principles of image potential, hopping conduction, and detailed balance, the Richardson constant is given by:

$$A^* = 16\pi\varepsilon\varepsilon_0 k^2 N_0 \mu / e^2 \tag{2.13}$$

$$S(0) = 16\pi\varepsilon\varepsilon_0 (kT)^2 \mu / e^3 \tag{2.14}$$

where *S(0)* is the recombination velocity in the absence of electric field. When electric field is applied, the barrier is lowered by the Schottky effect and the first term on the right-hand side of Equation (2.12) is multiplied by $\exp\left(\sqrt{f}\right)$. The recombination velocity becomes:

$$S(E) = S(0)\left(1/\psi^2 - f\right)/4 \tag{2.15}$$

where the reduced field is given by

$$f = e^3 E / 4\pi\varepsilon\varepsilon_0 (kT)^2 \tag{2.16}$$

and

$$\psi(f) = f^{-1} + f^{-1/2} - f^{-1}\left(1 + 2f^{1/2}\right)^{1/2} \tag{2.17}$$

This is the equation for the electron injection, where the electric field and mobility are taken from the left interface of the first cell, and the charge densities are from the node of the first cell. The same procedure is applied to the hole injection in the last cell among the numerical cell elements.

2.2.4.3 Charge behavior at the organic heterojunction

At the organic/organic heterojunction interface, the differences in hole and electron mobilities, and the barrier in work functions give rise to a discontinuity in charge

densities. The situation is resolved by finding new internal boundary conditions in the form of current density across the organic-organic interface, as indicated in Appendix B. Because there is no stacked charge, no creation and no extinction of charges at the interface, continuity and Poisson's equation are applied in a same way as at the cell interfaces without modification. The drift-diffusion equation is first integrated from the last node of the left-hand side material to the interface, and similarly integrated from the heterojunction interface to the first node of the right-hand side material in order to get the internal boundary conditions. These integrations give a discontinuous hole density for the left-hand side (p-) as a function of the variables of the last cell node, while the hole density for right-hand side (p+) is composed of the variables of the first cell node. It is also assumed that the interface states are in quasi-thermal equilibrium, because the thermionic emission and backflow currents dominate over the device current. Finally, the hole current density, p, is expressed by thermionic emission and backflow currents, similar to what was done for the metal-organic interface, as a function of hole densities of surrounding interfaces and the energy barrier between the two organic layers. The two integrated equations are rearranged for the hole density, and employed for a hole boundary condition in the right-hand side material. The same procedure can be applied to the electron current density.

The electrical simulation described above is quite similar to the Crone and Smith's work [24]. External quantum efficiency is calculated combining electrical model with the optical simulation explained in the previous section. Depending on the position of the emitting dipoles, the fraction of power that is coupled to leaky mode varies greatly. The exciton density distribution calculated from the electrical model therefore allows for a more accurate estimation of the total number of photons leaving to air. The combined

model is applied to the structure design of organic LED in Chapter 5.

2.3 Organic photovoltaic devices

2.3.1 Photon-electron conversion

Basic optical modeling of organic solar cells has been treated in some detail previously, [78][73] and will be reviewed only briefly here. A relatively novel aspect of the model discussed here is the generalization of the relevant physics to include incident illumination angle [66].

A typical organic photovoltaic (PV) cell is illustrated in **Fig. 2.7**, where the device structure is analogous to that of an OLED, i.e. organic thin films sandwiched between two electrodes, one of which is typically transparent. A solar cell can be operated in forward bias, where it produced power against a load; a photodetector can be operated also in reverse bias. In calculating the quantum efficiency of an organic PV cell or a photodetector, it is useful to examine all of the photon-electron conversion processes. One convenient representation of the conversion process is illustrated in **Fig. 2.7**. Photon absorption (Step 1) is followed by excited state relaxation of the electron-hole pair forming an exciton (Step 2). The second process releases energy through phonon emission. Phonon emission during carrier relaxation is a major source of heating in solar cells made from inorganic materials such as silicon; however, limited energy bandwidth of allowed states in organic semiconductors and close matching of the energy bandgap to the incident photon by appropriate material selection reduce the unnecessary photon absorption, leading to a relatively smaller amount of phonon emission. The generated exciton is a neutral quasi-particle that exhibits lifetimes ranging from nanoseconds to micro- and milliseconds [92]. As an exciton diffuses, it can recombine through photon or

photon emission (Step 3). If the exciton diffuses (Step 4) to the interface of donor and acceptor as a Frenkel exciton, it transforms to a charge-transfer exciton at the interface, and dissociates into free charges (Step 5), provided there exists a net thermodynamic driving force for forming the charge-separated state, and provided the transition to free charges overcomes the Coulombic binding energy of the exciton, which ranges between 0.1 and 2 eV [76]. Finally the free charges diffuse to the electrodes where they are collected (Step 7). This process typically involves further energy losses through bulk Joule heating (phonon emission) and also depends on the interface resistance between the organic layer and the electrode. The free charges may also recombine before being extracted due to several possible mechanisms including impurity trap states (Step 6).

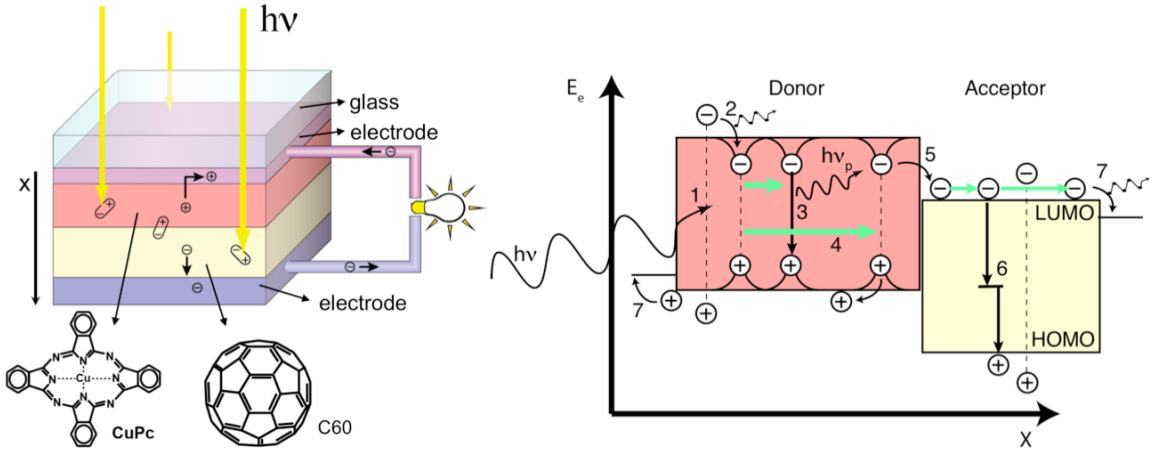

Figure 2.7 (a) An illustration of an archetypal organic photovoltaic cell, consisting of CuPc and C_{60} layers deposited onto ITO-coated glass, and covered by a metallic electrode. (b) An energy level diagram of the device, showing the basic processes involved in converting incident light into electrical energy. (Figure courtesy of Brendan O'Connor [66])

2.3.2 Optical field distribution in organic multilayer thin films

The electrical conductivity of organic optoelectronic materials is quite low com-

pared to that of inorganic semiconductors, due to narrow charge transport bands; charge transport is dominated by thermally activated hopping between highly localized sites (or traps). However, the optical absorption coefficients of organic materials are typically high ($\sim 10^5$ cm^{-1}) compared to the inorganic materials ($\sim 10^3$ cm^{-1}). Combined, these two properties dictate that the thickness of the active organic layers should be less than a few tens of nanometers. For efficient charge absorption and transport in organic PV cells, it is accepted [78] that the thickness of organic layers should be comparable to the diffusion length of the material, so that absorption efficiency and charge collection efficiency can be optimized from the standpoint of overall device efficiency. Following this reasoning, the total thickness of organic PV devices is typically less than 200 nm, which is on the order of the wavelength of visible light inside the organic layers. This fact implies that the optical field intensity distribution is non-uniform throughout the active device layers, affecting photoelectric conversion. To calculate the optical field in the organic thin film, we need to consider reflection, transmission, and refraction at every interface, keeping track of the phase changes. The transfer matrix formalism is well established for this purpose for multilayer system [35][78][73].

The materials contained within each layer can be assumed optically and electrically homogenous and isotropic, described by a wavelength-dependent complex refractive index ($\tilde{n} = n + i\kappa$); optically flat interfaces that do not scatter light are also assumed. The detailed notations are presented in **Fig. 2.8**. The incident light is modeled as an electromagnetic plane wave, and the incoherent effect of thick glass substrate is also included in the calculation.

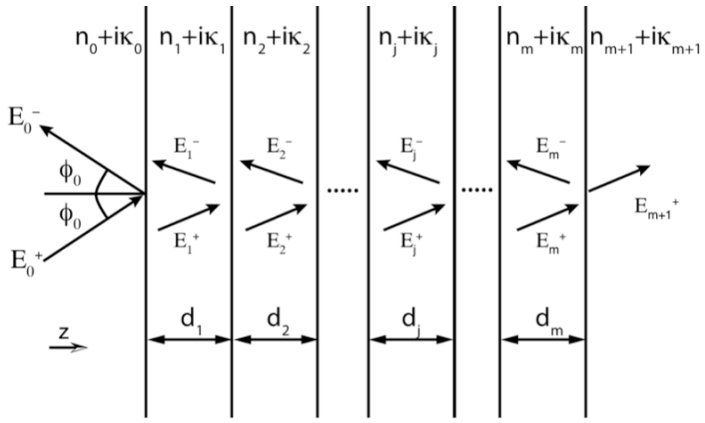

Figure 2.8 A diagram depicting multilayer thin films used in the transfer matrix formalism. Layers 0 and m+1 are considered semi-infinite media. Each layer has two electric field components propagating to the positive and negative z directions, except the layer m, where there is no incoming light (E^-_{m+1}). The layers are defined by a complex refractive index $n+i\kappa$ and a thickness d.

In modeling optical wave propagation across an interface, the optical electric field is described by interface matrix I_{jk} :

$$I_{jk} = \frac{1}{t_{jk}} \begin{bmatrix} 1 & r_{jk} \\ r_{jk} & 1 \end{bmatrix} \tag{2.18}$$

where r and t are reflection and transmission coefficients, defined differently depending on the polarization. For s-polarized light:

$$r_{jk} = \frac{q_j - q_k}{q_j + q_k} \tag{2.19}$$

$$t_{jk} = \frac{2q_j}{q_j + q_k} \tag{2.20}$$

and, for p-polarized light:

$$r_{j_k} = \frac{\tilde{n}_k^2 q_j - \tilde{n}_j^2 q_k}{\tilde{n}_k^2 q_j + \tilde{n}_j^2 q_k} \tag{2.21}$$

$$t_{j_k} = \frac{2q_j}{q_j + q_k} \tag{2.22}$$

with
$$q_j = \tilde{n}_j \cos(\phi_j) = \left[\tilde{n}_j^2 - \tilde{n}_0^2 \sin^2(\phi_0)\right]^{1/2} \tag{2.23}$$

For normal incidence (i.e. perpendicular to the device layers), considering s- or p-polarized components gives identical results. The propagation of electric field within a layer is described by the phase matrix:

$$L_{j_k} = \begin{bmatrix} e^{-i\xi_j d_j} & 0 \\ 0 & e^{i\xi_j d_j} \end{bmatrix} \tag{2.24}$$

with
$$\xi_j = \frac{2\pi}{\lambda} q_j \tag{2.25}$$

And, the total transfer matrix for the multilayer system is given by,

$$S = \begin{bmatrix} S_{11} & S_{12} \\ S_{21} & S_{22} \end{bmatrix} = \left(\prod_v^m I_{v-1,v} L_v \right) I_{m,m+1} \tag{2.26}$$

The incoming wave to the system is described by the total transfer matrix and outgoing wave:

$$\begin{bmatrix} E_0^+ \\ E_0^- \end{bmatrix} = S \begin{bmatrix} E_{m+1}^+ \\ E_{m+1}^- \end{bmatrix} \tag{2.27}$$

The total reflection and transmission coefficients are $r = E_0^- / E_0^+ = S_{21} / S_{11}$ and $t = E_{m+1}^+ / E_0^+ = 1 / S_{11}$ respectively. To compensate for the incoherence of the thick glass

substrate, we use a modified intensity at the glass-ITO interface:

$$I_{glass-ITO} = I_0 \frac{\left(1 - R_{air-glass}\right)e^{-2\pi k/\lambda}}{1 - R_{air-glass}R_{cell}e^{-2\pi k/\lambda}} \tag{2.28}$$

To find the electric field within layer *j*, we note the total transfer matrix:

$$S = S_j^- L_j S_j^+ \tag{2.29}$$

where,

$$S_j^- = \left(\prod_{v}^{j-1} I_{v-1,v} L_v\right) I_{j-1,j} \tag{2.30}$$

and

$$S_j^+ = \left(\prod_{v=j+1}^{m} I_{v-1,v} L_v\right) I_{m,m+1} \tag{2.31}$$

The electric field propagating in the positive *z* direction at the left interface of *j* layer is expressed by the incident wave,

$$t_j^+ = \frac{E_j^+}{E_0^+} = \frac{1/S_{j11}^-}{1 + \frac{S_{j12}^- S_{j21}^+}{S_{j11}^- S_{j11}^+} e^{i2\xi_j d_j}} \tag{2.32}$$

similarly, the field propagating in the negative direction at the left interface is given by:

$$t_j^- = \frac{E_j^-}{E_0^+} = t_j^+ \frac{S_{j21}^+}{S_{j11}^+} e^{i2\xi_j d_j} \tag{2.33}$$

The total electric field at an arbitrary position within layer *j* is given in terms of the electric field of the incident wave by:

$$E_x(z) = \left[E_p^-(z) + E_p^-(z)\right]\cos(\phi_j) = (t_j^+ e^{i\xi_j z} + t_j^- e^{-i\xi_j z}) E_j^+ \cos(\phi_0) \tag{2.34}$$

$$E_y(z) = E_s^+(z) + E_s^-(z) = (t_j^+ e^{i\xi_j z} + t_j^- e^{-i\xi_j z}) E_j^+ \tag{2.35}$$

$$E_z(z) = \left[E_p^+(z) + E_p^-(z)\right]\sin(\phi_j) = (t_j^+ e^{i\xi_j z} - t_j^- e^{-i\xi_j z}) E_j^+ \sin(\phi_0) \tag{2.36}$$

As an example, the resulting optical field intensity distribution is plotted for a structure in **Fig. 2.9** in the following section. The following sections describe how the PV cell photocurrent can be calculated from this distribution.

2.3.3 Calculation of external quantum efficiency

The overall efficiency is composed of absorption efficiency (η_{EQE}) and internal quantum efficiency(η_{IQE}). The η_A is simply the fraction of photons absorbed by the device, including, for example, parasitic absorption in the electrodes. The η_{IQE} is defined as the number of electron-hole pairs collected divided by the number of absorbed photon in the active materials, and can be further decomposed into a product of the efficiencies of the intermediate conversion steps:

$$\eta_{EQE} = \eta_A \eta_{IQE} = \eta_A \eta_{ED} \eta_{CT} \eta_{CC} \tag{2.37}$$

where the efficiency of photogenerated excitons diffusing to the organic interface is η_{ED}, the efficiency with which these excitons dissociate at the electron donor-acceptor interface is η_{CT}, and the efficiency of collection of the dissociated holes and electrons at the electrodes is η_{CC}.

Given the electric field intensity distribution inside the layers, we have time-averaged absorbed power:

$$Q(x) = \frac{4\pi c \varepsilon_0 \kappa_j n_j}{2\lambda} \left| E_j(x) \right|^2 \tag{2.38}$$

where c is speed of light, ε_0 is the permittivity of free space, and λ is wavelength. Absorbed power is used for generating excitons, and the generation rate is given by,

$$G(x) = \frac{\lambda}{hc} Q(x) \tag{2.39}$$

where h is Planck's constant. To calculate the collected photocurrent, the exciton distribution must be calculated first. The exciton diffusion equation is [78][73] :

$$L_D \frac{\partial^2 P}{\partial x^2} - P + \tau G = 0 \tag{2.40}$$

where L_D is the exciton diffusion length, P is the exciton density, and τ is the exciton lifetime. The equation is solved numerically in one-dimensionally discretized space by applying appropriate boundary conditions at interfaces. For a donor-acceptor (DA) interface, $P_{DA} = 0$, assuming every exciton at the interface is dissociated. For an organic-metal interface, $\partial P/\partial z = 0$, assuming ideal non-quenching condition. The photocurrent density is derived from the exciton diffusion current to the DA interface and is given by:

$$j_j = q \frac{L_D^2}{\tau} \left| \frac{\partial P}{\partial x} \right|_{x = x_{DA}} \tag{2.41}$$

where x_{DA} is the position of DA interface. Finally, the external quantum efficiency is obtained by normalizing photocurrent to the incident photon flux,

$$\eta_{EQE} = \frac{j_j / q}{(1/2) c \varepsilon_0 \left| E_0^+ \right|^2} \tag{2.42}$$

Here, we assumed charge transfer and charge collection efficiencies are assumed to be 100%. The simulation requires a pre-determined value of L_D for each material;

alternatively, the model can be used to fit experimentally obtained external quantum efficiency spectra, yielding L_D values specific to the experimental device [78][73].

As an illustration, consider analyzing an archetypal photovoltaic cell using the modeling procedure described above. Taking a typical device structure consisting of: ITO (140 nm) / CuPc (20 nm) / C_{60} (40 nm) / BCP (7 nm) / Ag (40 nm) the electric field is first calculated using the transfer matrix procedure for 600 nm incident light, shown **Fig. 2.9a**. The intensity of incident field is assumed to be unity for the calculation. In this particular case, the electric field intensity is peaked at the DA junction – an optimal situation. The corresponding exciton generation profile is shown in **Fig. 2.9b**, followed by a plot of the exciton concentration profile (**Fig. 2.9c**) that was obtained by solving the exciton diffusion equation. To confirm the validity of the simulation, the calculated external quantum efficiency spectrum is compared with experimentally obtained one in **Fig. 2.9d**. The calculation estimates the efficiency quite well over the entire range of visible wavelengths, using two fitting parameters of diffusion length of CuPc ($L_{D,CuPc}$ = 12 nm) and C_{60} ($L_{D,C60}$ = 19 nm). This validated model will be used in subsequent chapters to design tunable organic photodetectors, and to analyze their performance for variable incident angles.

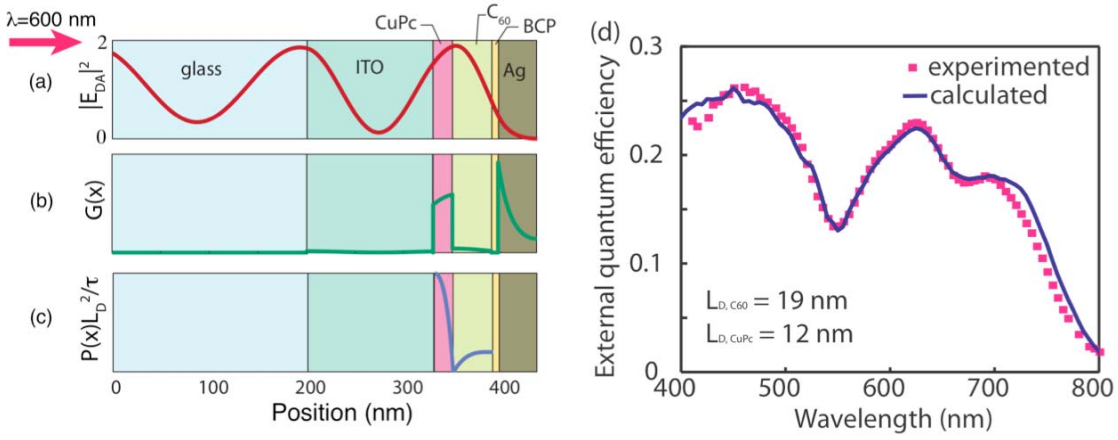

Figure 2.9 (a) Calculated electric field intensity distribution for an archetypal organic photovoltaic cell have the structure: ITO (140 nm) / CuPc (20 nm) / C_{60} (40 nm) / BCP (7 nm) / Ag (40 nm), illuminated by 600 nm monochromatic light incident from the substrate side. The intensity of incident electric field is assumed to be unity, so that constructive and destructive interference effects can be clearly seen; note that the peak in $|E|^2$ falls at DA junction – a desirable outcome that maximizes the EQE. (b) An exciton generation profile calculated from the optical field intensity. (c) The exciton concentration profile obtained by solving the exciton diffusion equation. Note that the photocurrent is calculated from the gradient of the exciton concentration curve, as indicated in Eq. 2.41. (d) A plot of the calculated external quantum efficiency (EQE), superimposed on experimentally obtained one, showing a good match using $L_{D,CuPc}$ = 12 nm and $L_{D,C60}$ = 19 nm fitting parameters.

CHAPTER 3

PLASMON-MEDIATED ENERGY TRANSFER IN ELECTRICALLY PUMPED ORGANIC DEVICES

3.1 Introduction

Surface plasmon polaritons (SPPs), commonly referred to as "surface plasmons (SPs)", are collective fluctuations of electron density at the metal surface; the field of their study and application is termed *plasmonics* [6][19][70]. Surface plasmon modes have been studied previously to improve the performance of light-emitting devices [67][33], high-resolution microscopy [84], surface characterization techniques [61], and sensors [41]. In recent work by Andrew and Barnes, surface plasmons were used to mediate energy transfer from optically-pumped dipoles across a thick metal film to fluorescent dye molecules [4], suggesting applications in efficient top light-emitting devices (LEDs), synthetic light harvesting structures, and high-resolution photochemistry near surfaces.

However, plasmon-mediated energy transfer from optically-pumped molecules is less useful for integrated optoelectronic devices than energy transfer from electrically-pumped molecules. Here we explore this latter topic, demonstrating strong plasmon-mediated transfer of energy from molecular excitons across the metallic cathode of an electrically pumped organic heterostructure. Engineering of this process can lead to new sensing and imaging applications with high SNR [112], and has the potential to improve

the performance of organic LEDs, energy harvesting devices [101][54], and plamonic devices [48].

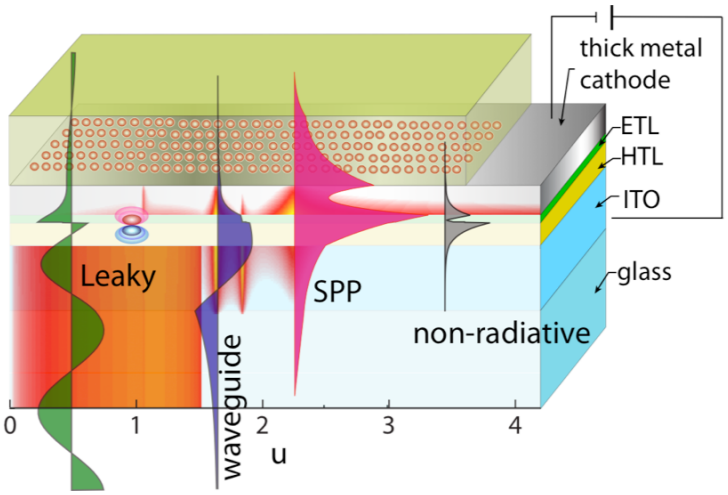

Figure 3.1 Illustration of the energy coupling of parallel-oriented excitons (excitonic dipoles) created at the interface of hole and electron transport layers. An energy flux diagram is superimposed on the corresponding layer structure (orange-red shading), indicating energy flux pathways for a normalized in-plane wave vector ($u = k_x / k_0$). For $u < 1$, the exciton energy decays through leaky light emission, which is more easily transmitted through the semitransparent ITO electrode than the thick metal electrode. Waves with $u \approx 1.63$ are guided in-plane through the device layers, and depending on the refractive index, the number might change. For $u \approx 2.24$, the emitted field strongly couples to bound surface plasmon modes at the two metal/organic interfaces. For higher u values, the energy couples to non-radiative mode. For each mode, the out-of-plane electric field is drawn. The leaky mode propagates in both directions, the waveguided mode is confined in organic and ITO layers, the surface plasmons are bound at the metal interfaces, and the non-radiative modes are highly confined inside the structure.

The energy transfer pathways for an electrically pumped organic heterostructure coated by a dye-doped dielectric film are shown in **Fig. 3.1**. Bipolar charge injection generates excitons at the junction between electron and hole transporting layers. These (donor) excitons then couple to surface plasmon polaritons (SPPs) in the metal electrode, and

the SPPs in turn excite dye molecules on the opposite side of the metal electrode. The coupling of SPPs to dye molecules on the "downstream" interface can occur by two mechanisms: 1) Evanescent coupling and 2) Absorption of propagating light scattered from SPP modes in the metal electrode by film roughness. Here we model and observe a strong dependence of the evanescent coupling strength on the relevant distances and thicknesses, and quantify the power distribution in the energy cascade taking place in the multi-layer device. A six-fold enhancement of light outcoupling efficiency is observed by appropriate designing of layer structure. This enhancement is not attributable to or attainable via optical microcavity effects alone.

In addition to elucidating the physics of the observed phenomenon, we quantify the transfer efficiency and show how the mechanism can be applied to, for example, a solid-state electrically pumped sensor with nanoscale resolution, and multi-modal imaging of nanomaterials and biological systems. Finally, we discuss the possible use of surface plasmon resonances in electrically-pumped devices to create sensitive monitors of biochemical reactions, based on the inherent electrical sensitivity of the devices to the exciton decay rate (which in turn responds to nearby chemical species).

3.2 Excitonic energy transfer across metal films

Understanding exciton-plasmon energy transfer is crucial to engineering thin-film optoelectronic devices, especially those based on organic semiconductor active layers. Consider, for example, the archetypical organic light-emitting device (OLED) structure shown in **Fig. 3.1** that consists of active organic semiconductors sandwiched between two electrodes, one of which is transparent [100]. In the most efficient OLED architectures, the organic layers compose a heterostructure that uses separate compounds to

efficiently transport electrons and holes, and to localize and maximize radiative recombination. Because the injection layers are thin, the electron-hole recombination zone (where light is emitted) is within tens of nanometers of the injecting electrodes. This proximity results in the strong and often parasitic waveguiding, as well as coupling of exciton radiative energy to non-radiative surface plasmons [22]. One approach to removing parasitic losses is to engineer the optical microcavity to place the node of the optical field inside one of the thin electrodes, using dielectric coatings on the external surface of the electrode [43]. This is an approach based on optical interference within the multiple layers, ultimately improving the optical transmission of the stack.

Considerable energy, however, is trapped in the SPP modes. To recover some of this dipole energy, electrode texturing has been employed [33]. This texturing causes the plasmon dispersion curve to be moved inside the light cone as illustrated in **Fig. 3.2**, leading to radiative outcoupling of surface plasmon energy to free-space photons. The amount of shift in the surface plasmon wave vector is determined from the grating period (λ_g). With the grating wave vector $k_g = 2\pi/\lambda_g$, the modified surface plasmon wave vector is given by $k'_{SPP} = k_{SPP} \pm k_g$ [104]. In case of random texturing, such as a uniformly rough film, the wavevector shift is thought to be random, giving uniform scattering for all wavelengths.

Another approach to enhancing the outcoupling of energy trapped in the SPP modes, which we explore here, is to engineer the device so that these modes resonantly couple to light-emitting dye molecules outside of the device (i.e. outside of the electrodes and the electrically pumped layers). The reverse process, in which external dye layers are excited by solar radiation and couple to excitons within a device through a plasmon-mediated process in a metal electrode, has been studied in organic photovoltaic devices

[54][38]. The measured energy transfer efficiency across the metal electrode was 46%. A similar energy cascade (plasmon-assisted Förster resonance energy transfer) was also demonstrated for a luminescent system by Andrew & Barnes [4], who used optically pumped molecular dyes dispersed in a polymer host. The coupling efficiency, however, was not reported. In contrast to the above two approaches, here we study the plasmon-mediated energy cascade issuing from *electrically-pumped* molecular excitons, and estimate the coupling efficiency.

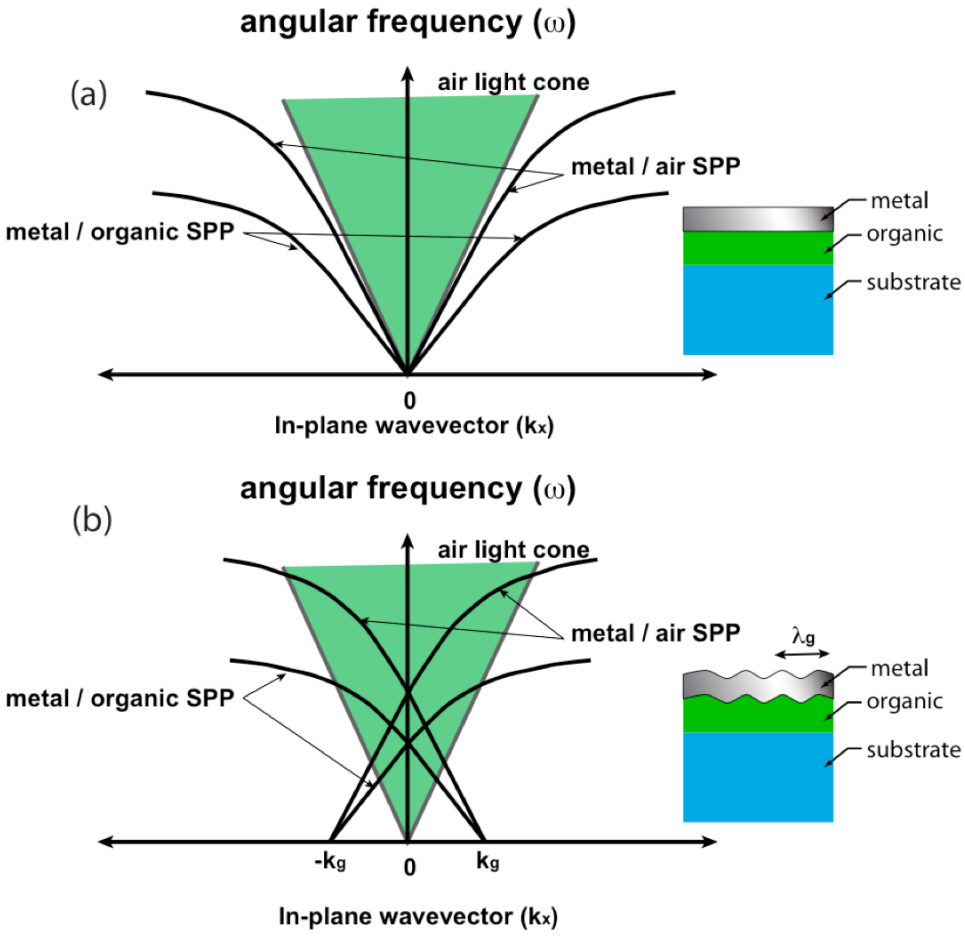

Figure 3.2 Dispersion diagram for (a) flat and (b) grating metal film on organic film. For flat metal on organic (dielectric) material, the surface plasmons on either side of the metal are outside of the light cone, which means that the surface plasmons are not outcoupled to the photons. In other hands, in a metal film with grating, the surface plasmons are shifting with grating wavevector (k_g), making the surface plasmons outcouple to light [104].

As discussed in Chapter 2, we use a classical dipole model [21] and a dyadic Green's function (DGF) approach [51] for exciton decay rate and energy flux calculations. Making critical corrections to Celebi's work [20] on the determination of DFG coefficients, we comprehensively analyze below the energy pathways of organic devices that are depicted in **Fig. 3.1**.

3.3 Modeled and measured SPP-mediated energy transfer in forward-biased organic devices

Our aim is to arrive at a device structure that maximizes SPP-mediated energy transfer from electrically-pumped molecular dipoles to dye molecules in an external coating layer. To accomplish this device optimization, we consider the influence of both the coating layer thickness (X nm) and the metal cathode thickness (Y nm). The device (**Fig. 3.3**) is based on a conventional organic light-emitting device (OLED) structure of ITO (150 nm) / α-NPD (50 nm) / Alq_3 (15 nm) / Ag (X nm) / α-NPD (Y nm), where the thickness of Alq_3 is reduced compared to conventional OLEDs in order to achieve better dipole-dipole energy transfer from the excitons to the metal, (in a mechanism very similar to Förster energy transfer). To detect the energy transfer across the thick metal film, we monitored the outcoupling of light for both pathways. One pathway is due to light energy radiated by decaying dipoles in the direction of the metal electrode, simply leaking through this electrode (① in **Fig. 3.3**) – this is termed *leaky mode*. The other pathway is due to energy coupling from decaying dipoles into SPP modes, which couple again to the dyes placed on the metallic surface (② in **Fig. 3.3**), termed *energy transfer mode*. We can define a figure of merit, as (=②/(①+②)) for maximizing the outcoupling fraction of energy path ②. The magnitude of this merit figure can serve as evidence for presence of

substantial the surface plasmon-mediated energy transfer across the thick film.

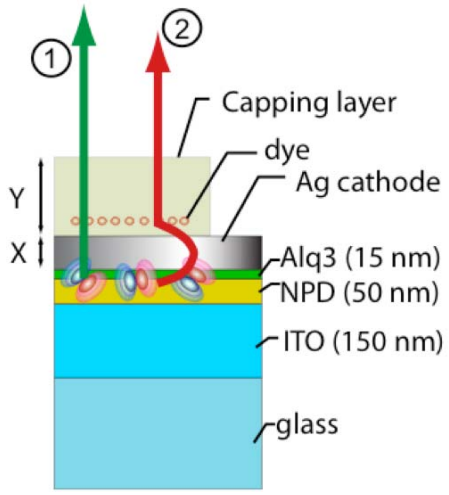

Figure 3.3 The designing structure for energy transfer device. The device is based on a conventional organic light-emitting device (OLED) structure of ITO (150 nm) / α-NPD (50 nm) / Alq_3 (15 nm) / Ag (X nm) / α-NPD (Y nm), where the thickness of Alq_3 is reduced compared to conventional OLEDs in order to achieve better dipole-dipole energy transfer from the excitons to the metal. The amount of light energy radiated by decaying dipoles in the direction of the metal electrode that leaks through this electrode is denoted "①" and the amount of energy coupled from decaying dipoles into SPP modes that again coupled to the fluorescent dyes placed near the metal electrode is denoted "②".

The use of an organic capping layer dramatically increases the rate of decay of excitons to SPPs by providing a matched boundary condition to strongly couple interior and exterior SPP modes. Calculations of exciton decay rate as a function of this capping layer thickness and in-plane wave vector are shown in **Fig. 3.4a**. It is apparent that interior and exterior SPP modes are increasingly coupled and approach a nearly identical in-plane vector as the capping layer thickness increases, due to the matched boundary condition on either side of the metal electrode. **Figure 3.4c** shows both leaky mode (①) and energy transfer mode (②) with the capping layer thickness, where 2% energy coupling

efficiency between the SPPs on the exterior metal-organic interface and the organic dye. (The optimum point for improved energy transfer does not vary appreciably with the assumed coupling efficiency.) The rate of exciton coupling to leaky modes has a periodic dependency on the capping layer thickness, due to optical interference effects (similar to the transmittance of the organic-metal-organic system in **Fig. 3.9**). In contrast, the rate of exciton coupling to SPPs and subsequent coupling to dyes placed on the exterior metal surface shows a monotonic increase with increasing capping layer thickness. To better separate the SPP pathway (②) from the leaky pathway (①), a 150 nm thick capping layer was chosen to minimize leaky radiation.

The metal cathode thickness was selected in a similar way. The decay rate calculation of **Fig. 3.4b** shows that the two SPP modes are better coupled as the thickness increases. Energy flux calculations (**Fig. 3.4d**) that include the effect of metal absorption show that absorption losses for leaky modes (①) increase exponentially as the metal thickness increases, and the losses are believed to be similarly increase to the surface plasmon coupling (②). As a result of these two competing mechanisms of field resonance and metal absorption, the rate of energy transfer to the coupled SPP modes has a maximum at 37 nm thickness of the silver cathode.

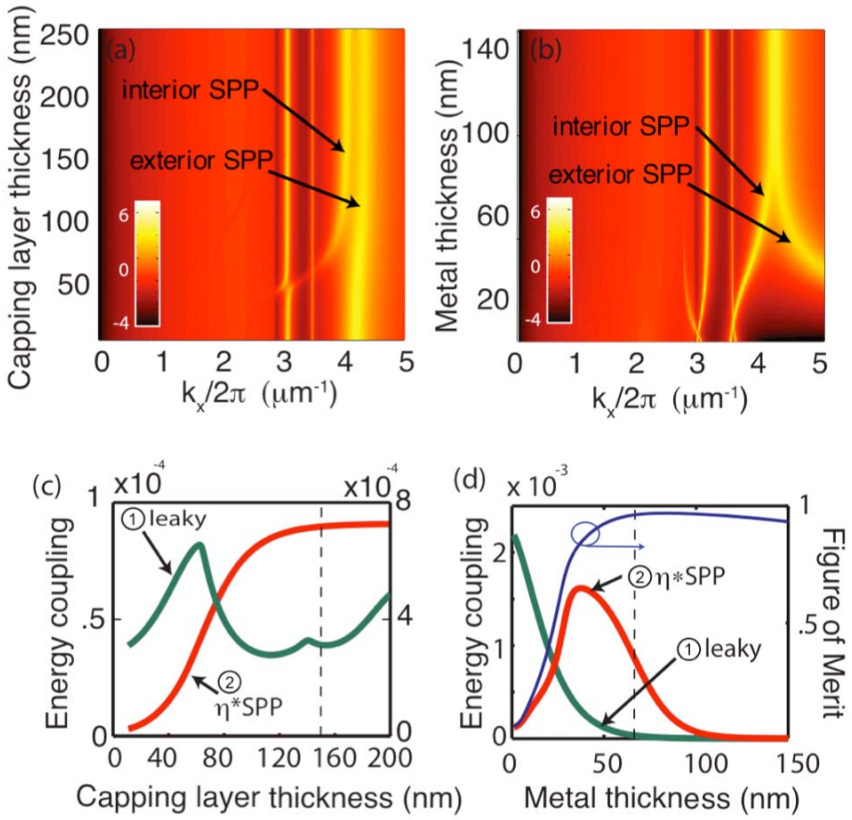

Figure 3.4 Calculated energy coupling rate (in log scale false color) for the device structure of ITO (150 nm) / α-NPD (50 nm) / Alq_3 (15 nm) / Ag (X nm) / α-NPD (Y nm), where the metal (X nm) and capping layer (Y nm) thicknesses are optimized for maximum energy coupling to surface plasmons. (a) Exciton decay rate as a function of capping layer thickness and in-plane wave vector (k_x). As the capping layer thickness increases, surface plasmons (near $k_x/2\pi = 4$) at the organic/metal and metal/capping surfaces start to couple, leading to increased electric field strength and efficient energy transfer from decaying excitons. (b) Similar phenomena occur when the metal cathode thickness changes. (c) Energy coupling rates to leaky (①) and surface plasmon modes (②), as a function of capping layer thickness. The energy coupling efficiency between surface plasmons at exterior interface and dye placed near the metal is assumed to be 2%. While the coupling to leaky radiation oscillates with the capping layer thickness because of optical interference effects, the symmetry introduced via the capping layer is responsible for the monotonically increasing of the SPP outcoupling. (d) A similar calculation as a function of cathode metal thickness. The figure of merit characterizes the fraction of energy transferred into cathode SPP modes (②) (versus leaky radiative emission (①) through the cathode). While leaky radiation shows an exponential decay due to metal absorption, coupling to SPP modes shows an optimal point as a result of the two competing mechanism of field resonance and metal absorption.

Applications of this device in sensing and microscopy are likely to achieve highest SNR when the coupling to SPPs (②) is maximized and light leaking (①) through the cathode is minimized, which is similar concept to the previously defined figure of merit. For better detection of surface plasmon mediated energy transfer, we choose 65 nm-thick silver, maximizing the figure of merit in **Fig. 3.4d**.

A set of glass / ITO (anode) / α-NPD / Alq_3 / Ag (metal cathode) / α-NPD (capping layer) devices was fabricated to experimentally test the coupling mechanisms discussed above. Device I had no α-NPD capping layer, resulting in SPP modes that were confined to the Alq_3/Ag interface as shown by the (red) electric field of **Fig. 3.5a**. Devices II and III had a 150 nm thick α-NPD capping layer (the optimal thickness of **Fig. 3.4c)**, leading to a strong (blue) electric field at both interior and exterior surfaces of the cathode caused by coupled surface plasmons. While capping layer is doped with 5% DCM2 in mass ratio in the far edge of the capping layer for device II, dye is inserted in the region adjacent to the metal in device III. The detailed layer structure is presented in **Fig. 3.5**. The DCM2-doped α-NPD has an absorption peak at λ=530 nm, which is very close to the emission peak of Alq_3 (λ = 525 nm) and therefore expected to favor resonant coupling. Devices I, II, and III are simultaneously fabricated on one device cell to facilitate comparison at identical operating conditions and mitigate erroneous data due to run-to-run nonuniformities.

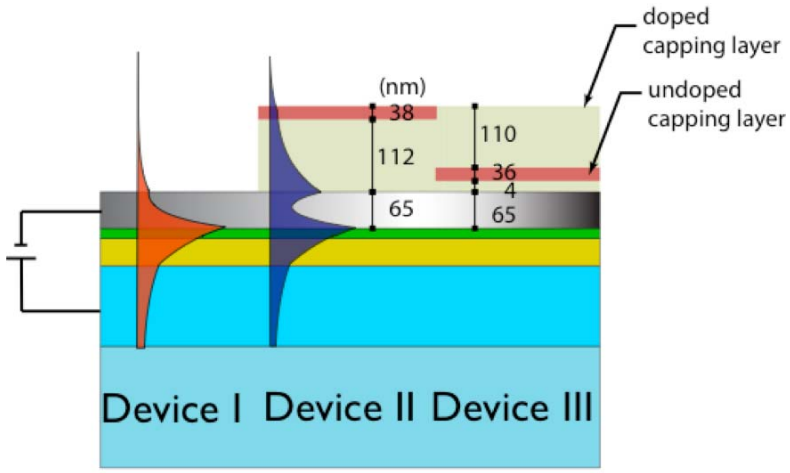

Figure 3.5 (a) Three device structures for convenient energy transfer measurement, using an archetypal OLED structure as a common substrate, but observed from the side opposite the substrate (from the top). Device I is a bare OLED, with no capping layer, resulting in an SPP mode that is confined only at the interior metal interface as shown in the (red) electric field (E_z). Devices II and III have a 150 nm thick capping layer of α-NPD, leading to a strong electric field at both interior and exterior surfaces of the metal film (blue color electric field). DCM2, a red-emitting dye, is doped into the α-NPD outer layer with 5% mass ratio for Device II and III. The accurate position of the doped region within the capping layer is shown. While Device II has dye doped region far from the metal electrode, Device III has dye-doped region adjacent to the metal layer.

Figures 3.6a and **Figures 3.6b** show electroluminescence and emission spectra of the devices with 7V bias. Device III exhibits a significant red peak due to DCM2 dye emission, indicating efficient plasmon-assisted transfer of energy from decaying excitons in the device across the thick metal film to the DCM2 dye adjacent to the metal. To verify that this red emission is not merely photoluminescence (PL) due to the absorption of leaky radiation transmitted through the cathode, we examine the spectrum of Device II. Devices II and III are expected to have nearly the same leaky light intensity (even after accounting for microcavity effects, as discussed below), and since their only difference is the location of the DCM2 layer, they are expected to have the same PL intensity. Device

II shows little red emission, which shows that dye PL is weak in Devices II and III, and furthermore shows that the energy transfer mechanism is consistent with the exponential decay of the evanescent SPP field into the capping layer. In fact, the model discussed above predicts that the field intensity in the DCM2 layer of Device II is 5 times smaller than the field intensity in the DCM2 layer of Device III.

We can understand plasmon-mediated energy transfer in these devices in greater depth by numerical modeling. The dispersion diagrams for Device I (**Fig. 3.7a**) and Device II or III (**Fig. 3.7b**)[1] show that coupled surface plasmon modes at both metal interfaces exist only in devices that have a capping layer. These modes provide an efficient path for energy transfer to the DCM2 dye molecules, as shown in the energy flux diagram of **Figs. 3.7c** and **Figs. 3.7d**. The surface plasmon is confined in the interior metal interface (metal/organic) in Device I, most of the energy being absorbed in lossy metal film (**Fig. 3.7c**). A large amount of energy, however, is found to be transferred to the dyes in the capping layer via coupled surface plasmons as shown in **Fig. 3.7d**.

[1] Note that the device dispersion diagrams for Device II and III are identical, independent of the position of the acceptor (DCM2) dye.

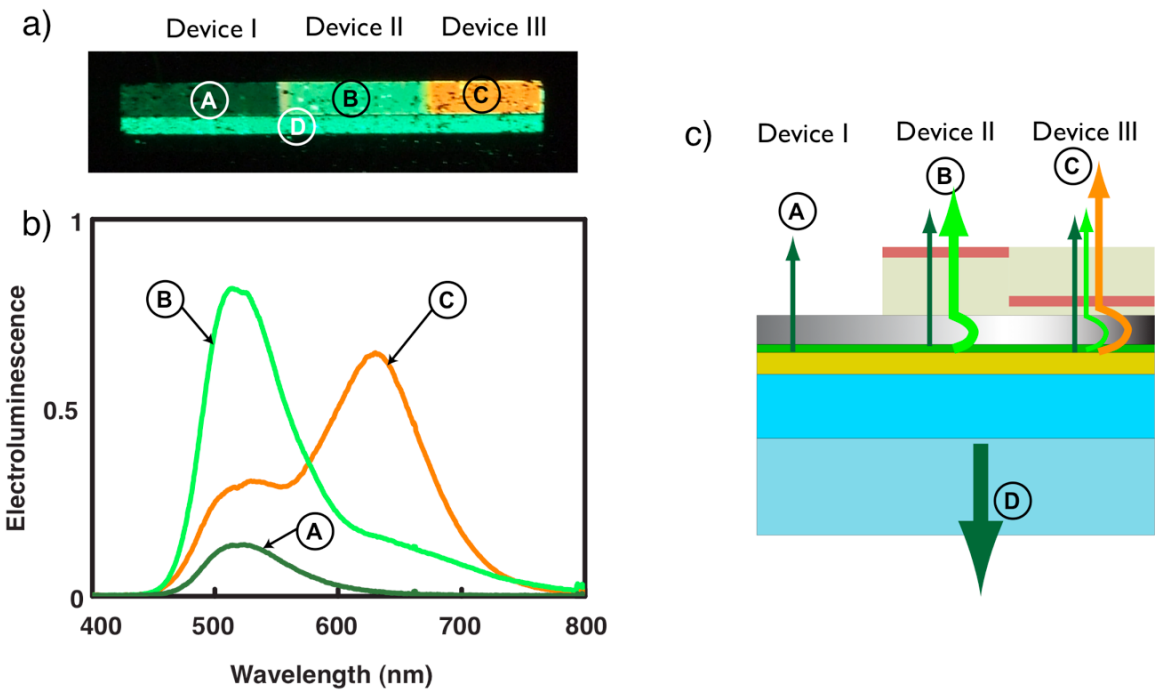

Figure 3.6 Measurement of energy transfer. a) A photograph of the energy transfer devices deposited onto a common substrate, operating under forward bias, imaged from the top (silver electrode side). The pathways labeled Ⓐ,Ⓑ, and Ⓒ are tied to the light emission through the top of each Device I,II, and III. Pathway Ⓓ is the bottom light emission to the ITO side, which remains essentially constant among the three devices. In Device III, the evanescent SPP fields efficiently couple energy into DCM2 dye through a resonant near-field process, leading to strong dye emission (Ⓒ) – seen as orange light. Device II shows 6-hold enhanced emission of green light (Ⓑ) compared to Device I (Ⓐ). The increased energy content in SPP modes at the exterior metal surface is scattered outward into propagating light modes due to metal film roughness. (b) Emission spectra measured from the top of each device clearly show the energy transfer in Device III and enhancement of light emission in Device II. (c) In Device I, direct emission from the leaky mode through thick metal film is detected, but is quite dim. In Device II, scattering of surface plasmons by roughness enhances the light emission in addition to the emission of Device I. However, note that the emission color is green, despite the presence of the dye molecules. In Device III, most of the surface plasmons in the exterior interface coupled to the DCM2 dyes before being scattered out by roughness, giving strong dye emission (Ⓒ). The coupling in Device III is much stronger than in Device II, due to dye proximity to the metal surface and immersion in the evanescent field of the SPPs.

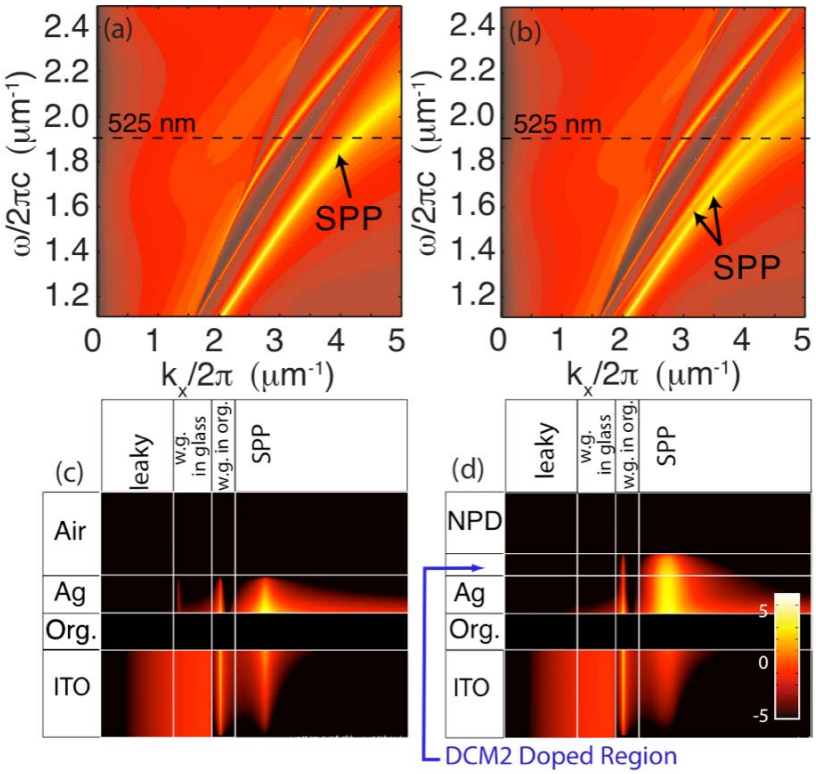

Figure 3.7 Dispersion diagrams of energy coupling for Device I (a) and Device III (b). While surface plasmons are generated only at the interior (Alq_3/Ag) metal interface in Device I, coupled surface plasmons are created at both (Alq_3/Ag and Ag/α-NPD capping) metal interfaces in Devices II and III (b). (c) and (d) represent the energy flux through the device layers calculated from the Poynting vector, clearly indicating energy transfer from decaying electrically-pumped dipoles into leaky, waveguided, surface plasmon, and lossy modes. From (d) it is clear that a large amount of energy is transferred to the dye in the capping layer via coupled surface plasmons. The transfer is most effective when the dye is adjacent to the outer metal-capping layer interface due to near-field interaction. The scale is indicated in (d) in log scale.

Surface patterns or roughness can also provide the required in-plane wave vector for the surface plasmon to be outcoupled to radiation, as observed in Device II. In this device, green (λ=525 nm) emission was enhanced by a factor of 6 compared to Device I. Atomic force microscopy (AFM) measurement of the topography of the Ag film shared

by all three devices showed a 6 nm RMS roughness (see **Fig. 3.8**), which is sufficient to outscatter surface plasmon modes [67].

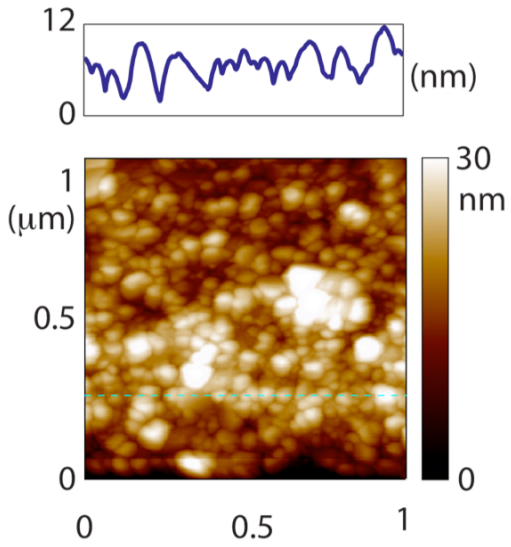

Figure 3.8 Atomic force microscopy (AFM) topographic image of the top surface of the rough silver film. The root mean square (RMS) roughness is 6 nm.

Calculations of the far-field transmittance of a Alq_3 (20 nm)/metal/capping layer structure show oscillations with increasing capping layer thickness regardless of the metal type, due to optical interference effects. The transmission characteristics of this structure with 150 nm capping layer thickness (i.e. Devices II and III) and zero capping layer thickness (i.e. Device I) exhibit little difference in transmission, as shown in **Fig. 3.9**. This supports the conclusion that the 6-fold enhancement in green light emission seen in Device II is not related to leaky (direct) radiation through the thick metal film, but rather to the outscattering of the large amount of coupled surface plasmons. The total top emission is the sum of leaky radiation and outscattering of surface plasmons. (see **Fig. 3.6c** ○B) The outscattering efficiency of surface plasmons is calculated to be 1.6% from

the green emission enhancement ratio and calculated direct emission and scattering of surface plasmons by roughness: $(I_{rad}+\eta_{SC}I_{SPP})/(II_{rad}+\eta_{SC}II_{SPP})=6$, where I_{rad} and I_{SPP} are the power coupling to radiation and surface plasmons respectively in Device I, and II_{rad} and II_{SPP} are for Device II.

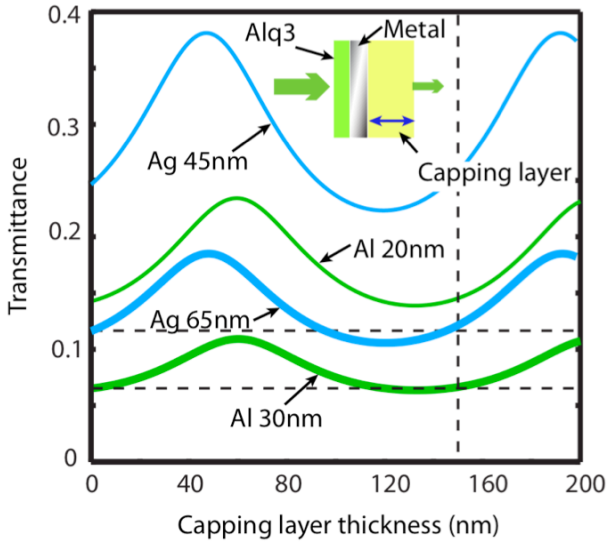

Figure 3.9 Transmittance calculation of Alq_3 (20 nm)/metal/capping layer structures. Regardless of the metal type and its thickness, the transmittance curves show oscillations attributable to optical interference effects due to the capping layer. For the range of cathode thicknesses studied in this chapter, there is little difference in transmitted power for a 150 nm capping layer (i.e. Devices II and III) and a 0 nm capping layer (i.e. Device I).

To further support the assertion that energy transfer by coupled surface plasmons is the main cause for the observed light emission enhancements, a further set of experiments was performed using an aluminum cathode rather than silver. Devices BI, BII, and BIII used a 30 nm Al cathode instead of 65 nm Ag, all other layers being identical with Devices I, II, and III. From the dispersion diagram and energy flux diagram of **Figs. 3.10a** and **Figs. 3.10b,** we found that there is no significant coupled surface plasmon mode for the Al cathode devices, resulting in only a tiny amount of energy transfered to

the dyes of capping layer.

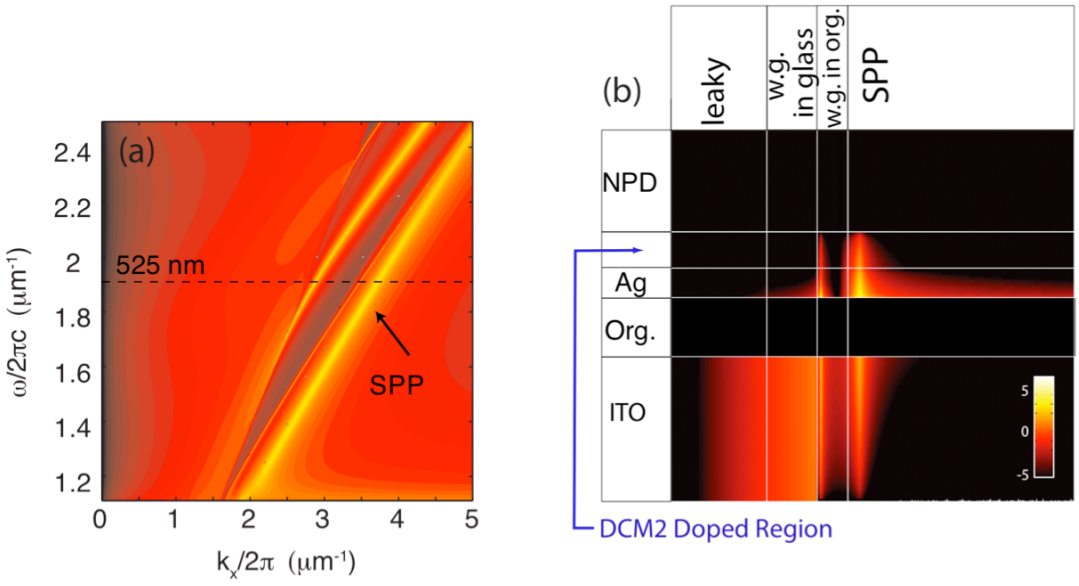

Figure 3.10 The dispersion diagram (a) and energy flux diagram (b) show that there are no coupled surface plasmon modes for a device based on Al cathode. Surface plasmons excited at the interior interface of Al (Al/Alq_3) are highly confined in the interface, resulting in only a tiny amount of energy transfer to the dyes.

Electroluminescence and emission spectra shown in **Fig. 3.11** for devices with Al cathodes exhibit no change in green emission intensity and only a weak increase in red emission for the devices with DCM2 dye layers (BII and BIII). The insignificant changes in measured green emission and negligible red emission is consistent with the above calculation results. As discussed above, there is negligible difference in leaky mode transmittance. And also with the Al cathode, there are no supported coupled surface plasmons at the metal interfaces, leading to no enhancement of light emission by outcoupled surface plasmon, and no energy coupling from surface plasmons to dye placed in the capping layer.

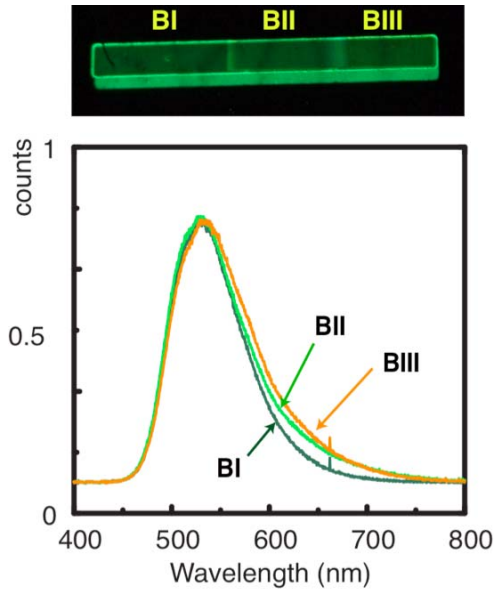

Figure 3.11 Electroluminescence and emission spectra of the control samples. Device BI, BII, and BIII used 30 nm Al cathode instead of 65 nm Ag; all other layers were identical with Devices I, II, and III. There is no change in green emission intensity, and a small red emission signal from DCM2 dyes from Device BII and BIII. Red emission from the BII is from the PL of dyes, and some of red emission from BIII comes from the energy transfer by way of surface plasmons. However, the amount of energy transferred is small compared to the device with silver cathode.

In summary, surface plasmon mediated energy transfer of electrically-pumped excitonic energy across a thick metal film was demonstrated for the first time. This mechanism appears to be useful for improving top-emission in OLEDs. Furthermore, we propose a scheme for an integrated electrically-pumped evanescent wave generator with applications in very high resolution optical microscopy and lab-on-a-chip.

3.4 Integrated thin film surface plasmon resonance detector

Based on the energy transfer mechanism described above, an integrated thin film surface plasmon resonance detector can be proposed. The conventional surface-plasmon

resonance (SPR) detector is a widely used as a label-free sensing tool for bio applications because of its high sensitivity to the refractive index changes in a molecular level reaction on top of metal surface. However, the complex and bulky optical components of conventional SPR detectors, such as light source, lenses, filters, and detectors, result in high system cost. Furthermore, the large optical components prevent the system from being miniaturized for use in compact, point-of-care monitoring systems that are of growing interest. **Figure 3.12** shows a conventional SPR detector, comprising complex optical components and two-dimensional detector. When bio molecules react with the ligands that are attached to metal surface, not only the effective refractive index of the part above the metal film, but also the thickness of the high index material on the metal increase. In consequence, the resonance condition for the surface plasmon changes. This altered condition is measured through the reflection measurement where the dip in the reflectivity signal versus wavelength or angle on the two-dimensional detector is modified as shown in **Fig. 3.12**.

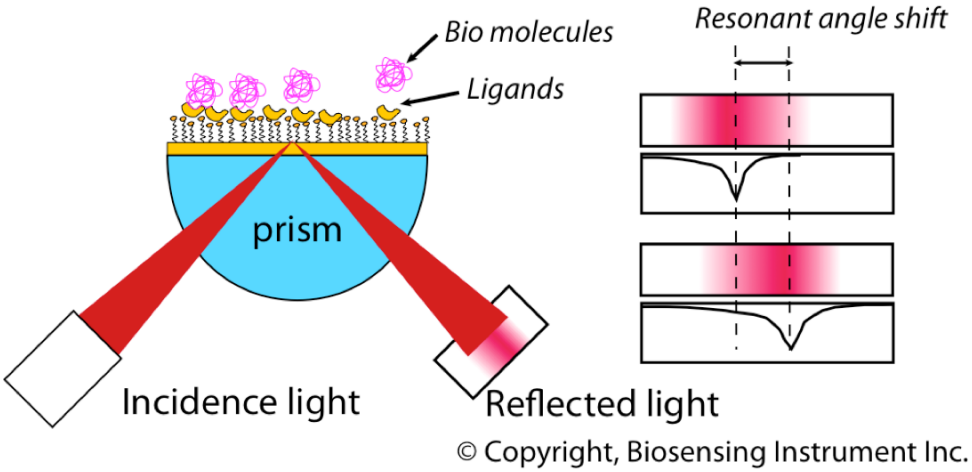

Figure 3.12 Conventional reflection measurement setup for a surface plasmon resonance for bio applications.

The proposed integrated thin film surface-plasmon resonance (SPR) detector uses an electrical signal that is modulated by changes in refractive index and thickness of materials on top of metal surface, without the assistance of any optical parts and detector. The thin film detector is composed of two metal electrodes as a hole and electron provider, and active organic materials that generate excitons at the organic heterojunction. The decay rate of the excitons inside the device is strongly dependent on the composition of adjacent layers, particularly for excitons near the metal surface interfere with the reflected electromagnetic waves and surface plasmons. The organic heterojunction structure is designed such that the power coupling of the dipoles to surface plasmons are maximized in order to make the device very sensitive to refractive and thickness changes on the metal surface, based on the calculation of the previous chapter (Section 2.2). **Figure 3.13** illustrates the integrated thin film SPR measurement setup based on this new organic optoelectronic device. A 40 nm thick layer of aluminum is first deposited, followed by organic thin films (70 nm ETL and 15 nm HTL) whose emission peak is at 525 nm, followed by a thin (15 nm) gold film as the anode. The gold anode also functions as a reaction surface, on which the analyte (label free) molecules adsorb. The refractive index and thickness variations caused by molecular reaction on the gold film alter the decay rate of the excitons.

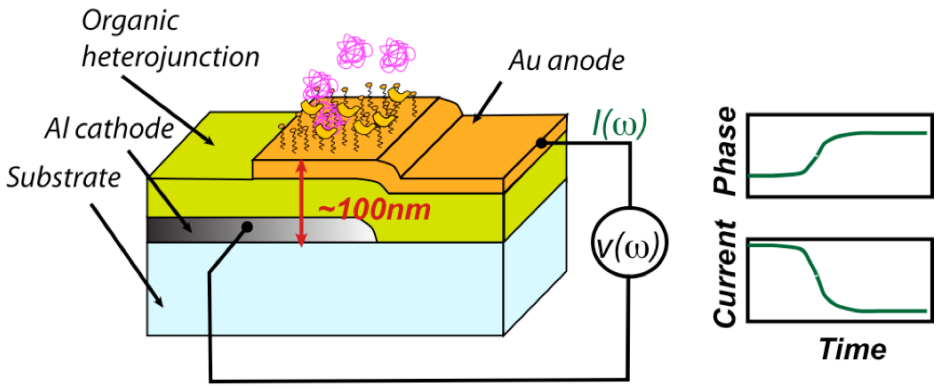

Figure 3.13 A proposed thin film surface plasmon resonance detector

To predict the effect of molecular reaction on top of metal surface, We calculated the variation in the exciton decay rate upon modifying the refractive index and thickness of the capping layer on gold, using the classical dipole oscillator model of Chance, Prock, Silbey described in Chapter 2. This approach allows the estimation of the power dissipation rate to radiative and waveguided modes, to surface plasmons, and parasitic loss to the electrodes. The calculated power dissipation spectrum indicates the coupling efficiency of dipoles to each mode goes, as shown in **Figs. 3.14a** and **Figs. 3.14c**. The thickness and refractive index of the capping layer greatly affect the dissipation rate of dipoles to surface plasmons at the outer interface of the gold film, maintaining the coupling to other modes at similar levels as without the capping layer. This is the main cause of the dramatic drop in the total decay rate of dipoles when there are small changes in thickness (from 0 to 10 nm), or in refractive indices (from 1 to 2.5), as shown in **Figs. 3.14b** and **Figs. 3.14d**. A similar effect is predicted to occur when silver is used instead of gold, with an emitter with peak wavelength of 475 nm.

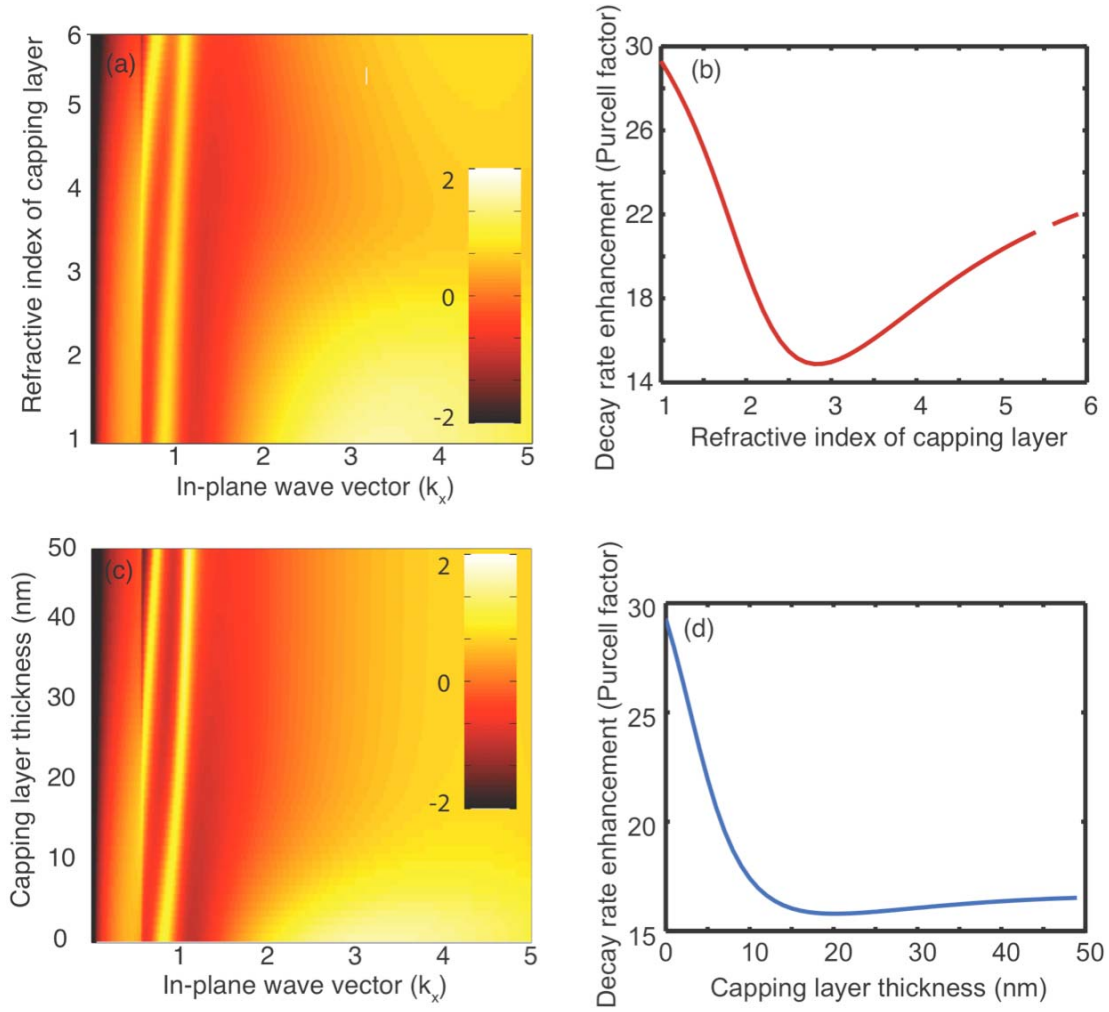

Figure 3.14 Variation of decay rate depending on the capping layer thickness (a-b) and refractive index of capping layer (c-d). (a) and (c) shows energy dissipation diagram, where bright region indicates higher energy dissipation. Excitons that have high in-plane wave vector (k_x~3.5) are associated with the surface plasmon. As the thickness and refractive index of capping layer increase, the energy dissipation to the surface plasmon are decrease, resulting in reduced total decay rate.

It is possible that the changes in the dynamic exciton concentration will result in small but detectable changes in the conductivity of the organic films and/or the heterojunction. One therefore expects the exciton decay rate changes to translate into an electrical signal from the device. To test this hypothesis, heterojunction devices were tested *in situ* in forward bias, while the capping layer was deposited. The device consisted of an

archetypal OLED, with the layer structure: Al (70 nm) / α-NPD (50 nm) / Alq_3 (60 nm) / Ag (30 nm), followed by a capping layer of variable thickness. The decay rate of the dipoles is predicted to oscillate with capping layer thickness, with some damping due to the interference effects, as shown clearly in **Fig. 3.15a** for a given wavevector. The total decay rate can now be compared to the measured current variation with the capping layer thickness. The measurement is done *in situ* in the vacuum evaporation chamber during the deposition of an Alq_3 capping layer; the bias was held constant at 6 V. The measured variation in the device current shows a very similar trend, strongly suggesting a linear relationship between the exciton decay rate at constant forward bias, and the current through the device. It is therefore quite likely to be able to detect molecular reactions on top of the metal surface, enabling integrated bio-sensing or chemical sensing devices.

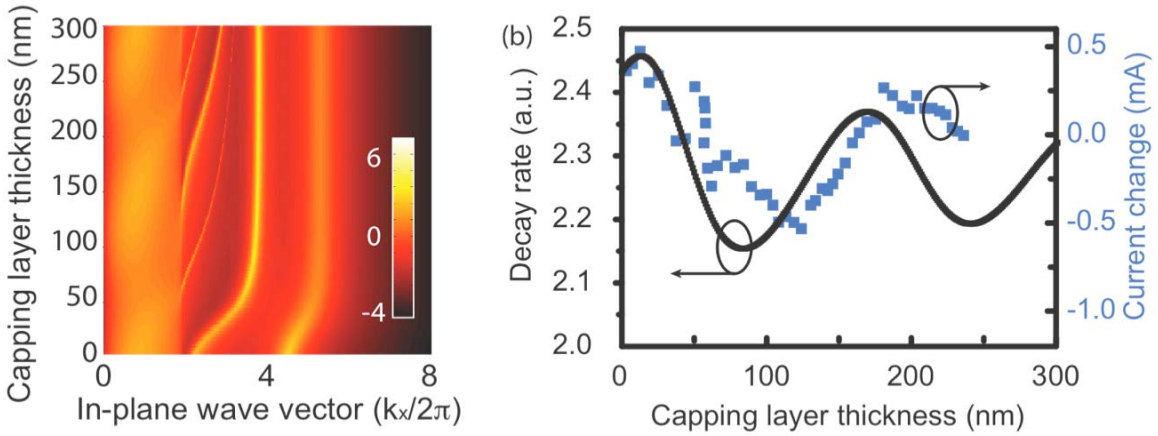

Figure 3.15 Decay rate diagram (a) and decay rate variation (b) of dipoles depending on the capping layer thickness on Al (70 nm) / α-NPD (50 nm) / Alq_3 (60 nm) / Ag (30 nm). The decay rate of the dipoles oscillates with damping due to the interference effect. The decay rate diagram (a) clearly represents that the radiation mode oscillates. The total decay rate is compared to the measured current variation depending on the capping layer thickness. The measurement is done in-situ in the vacuum evaporation chamber during deposition of Alq_3 capping layer at a constant 6 V biased.

CHAPTER 4
MICROCAVITY-BASED
TUNABLE ORGANIC PHOTODETECTOR

4.1 Background

The previous two chapters discussed electrically pumped sensor configurations, where bipolar charge injection lead to formation of excitons, which coupled to a medium on the outside of the device via optical interference effects, surface-plasmon-polaritons, or other near-field interactions. The sensing process could be accomplished by monitoring the decay rate of excitons, the intensity, and/or wavelength of light emission from the device. Additionally, a feedback mechanism exists between electrical transport in the organic heterostructure and the exciton decay rate (which is sensitive to changes the device's environment), potentially enabling the use of the device's current-voltage characteristic for sensing.

In this chapter, we turn to sensors based on the photovoltaic (PV) effect. Optical excitation of semiconductor thin films leads to the formation of electron-hole pairs (in the case of organic semiconductors, the electron-hole pairs form tightly bound Frenkel excitons), which can be dissociated by an applied electric field and/or by an appropriately chosen p-n junction (or an electron donor-acceptor heterojunction, in the case of organic PV devices). With regard to designing sensors based on the photovoltaic effect, organic materials offer a number of advantages. Many molecular organic dyes exhibit very large

absorption coefficients (~10^5 cm^{-1}), motivating their use in optical recording and paint pigments, solar cells and photodetectors.

Organic photodetectors (OPDs) [78][80] have received considerable research attention for applications such as image scanners [60], artificial eyes [105], and microfluidic sensors [40]. The speed [57] and sensitivity [80][74] of OPDs have been investigated in detail, addressing limitations due to deep trapping and low charge mobility [74]. Several applications of OPDs have been targeted, including the detection of fluorescence signals in microfluidic systems [59], where organic-based devices could simplify integration, improve portability, and reduce cost. Yao et al. [108] used organic light emitting devices (OLEDs) as excitation sources for fluorescence-based detection of proteins, showing compatibility with a polydimethylsiloxane (PDMS)-based microfluidic channel. Pais et al. [71] combined both an OPD and an OLED in a compact, low-cost, and highly sensitive fluorescence detection system for a disposable lab-on-a-chip device.

For many OPD applications, spectral selectivity is critical. An OPD used for biological imaging must discriminate between strong excitation and weak fluorescent emission signals that have narrow spectral separation (and often must furthermore distinguish the emission of multiple fluorescent dyes). To this end, Pais et al. [71] incorporated two cross-aligned polarizer films to separate the fluorescence signal from the excitation light source. Addressing spectral selectivity requirements for colorimetry applications, Antognazza et al. [5] used three distinct organic materials in the active layers of their OPDs, demonstrating photoresponse curves that mirrored the standard color matching function. Seo et al. [91] demonstrated a color sensor by vertically stacking three photodetectors that were individually sensitive to only blue, green, or red light. However, the color separation characteristics in the stacked sensor were sub-optimal, primarily due to the

broad absorption spectra of the active organic layers. Achieving wavelength selectivity by simply using organic dyes with different absorption spectra often presents additional practical challenges, particularly in optimizing the electrical characteristics of the detector.

Optical microcavity effects provide an alternative approach to tune the wavelength selectivity of a photodetector. These effects arise due to the interference of electromagnetic waves in dielectric cavities sandwiched by reflective layers, in which the optical path length is on the order of a wavelength. As with a Fabry–Perot interferometer, the microcavity structure exhibits spectral selectivity due to resonant optical modes in the cavity. Lupton et al. [53] utilized this effect in an OPD by replacing the cavity layer with photoactive materials, fabricating a Bragg reflector below the indium tin oxide (ITO) substrate and depositing a semi-transparent silver top electrode to form the top mirror. The spectral selectivity of the device was shown to depend on the bilayer cavity thickness, although the sensitivity and spectral selectivity remained relatively low due to a relatively low cavity quality (Q) factor caused by parasitic absorption in the thick photoactive layers. Furthermore, the maxima of the standing wave of the resonant field were positioned far from the donor–acceptor interface where exciton dissociation takes place, lowering the quantum efficiency of the detector.

4.2 Organic photodetector with spectral response tunable across the visible spectrum

This chapter describes a microcavity organic photodetector that incorporates a conductive, transparent optical spacer inside the cavity and places the organic heterojunc-

tion near a peak intensity of the resonant field. This results in a stronger optical microcavity (an enhanced Q factor) and hence increases the sharpness of the spectral response. Detector sensitivity is enhanced by two orders of magnitude over prior work [53], and the peak wavelength can be tuned across a much wider range. We also study the effects of metal mirror roughness on the external quantum efficiency (EQE) spectrum, accounting for roughness explicitly in our optical model and demonstrating excellent agreement between predicted and measured EQE when topographical data obtained via atomic force microscopy (AFM) is incorporated. Finally, we study the angular dependence and frequency response of our devices.

Appropriate optical spacer materials should exhibit low electrical and optical losses, as well as a properly matched work function to reduce contact resistance. Optical spacers such as TiO_x [46], bathocuproine (BCP), and C_{60} [78] have previously been used in organic solar cells. Archetypal organic solar cells, however, are weak microcavities since they are most often deposited onto ITO electrodes, resulting in a low cavity Q factor. Instead, thin metal films are used for both anode and cathode [65], and a considerably thicker optical spacer is used to substantially increase the strength of the electric field near the organic heterojunction, thereby enhancing the narrow-band quantum efficiency of the device. Vacuum-deposited molybdenum trioxide (MoO_3) is used as the optical spacer, facilitating the fabrication of the photodetector by conventional vacuum thermal evaporation. As shown in **Fig. 4.1**, MoO_3 has good transparency over a broad range of the visible spectrum (where the EQE peaks of our OPDs are located). Current–voltage measurements of a 40 nm Ag / 140 nm MoO_3 / 50 nm Al structure yielded Ohmic characteristics with a resistivity of $5x10^5$ Ω•cm, which is several orders of magnitude lower than that of most organic materials. The work function of MoO_3 is known to be 5.8 eV

[69], enabling efficient hole collection.

To precisely identify OPD structures with desired external quantum efficiency (EQE) spectra, optical models based on the transfer matrix approach are employed, predicting the optical field distribution within the multilayer structure. These models were coupled to exciton transport equations that account for exciton generation, extinction, and diffusion [78][63][73]. The models assume literature values for exciton diffusion length (100 Å for CuPc and 300 Å for C_{60}) [78], and 100% charge dissociation and extraction efficiency. The simulated device layer structure has a 50 nm Al anode, variable thickness MoO_3 spacer, 20 nm copper phthalocyanine (CuPc) donor, 40 nm C_{60} acceptor, 7 nm BCP exciton blocking layer, and 40 nm semi-transparent silver cathode. Wavelength-dependent optical constants for these layers were taken from literature [73][62][72][89].

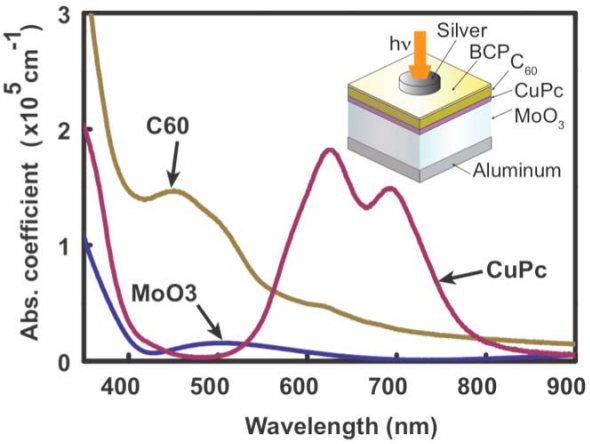

Figure 4.1 A comparison of the absorption coefficients of MoO_3, CuPc, and C_{60}, indicating that a MoO_3 film remains transparent across the visible spectrum. (inset) An illustration of the photodetector structure.

The photodetector structure is illustrated in the inset of **Fig. 4.1**. Calculated electric field profiles within the device for the visible range of incident wavelengths are

shown in **Fig. 4.2a**, assuming a 150 nm thick MoO_3 optical spacer. The engineered spectral responsivity is apparent in **Fig. 4.2a**, which compares the electric field profile for the 430 nm non-resonant wavelength to that of the 520 nm wavelength, which is near the second resonant mode of the microcavity. The left peak for the resonant mode is very close to the organic heterojunction, leading to increased optical absorption in this region and hence larger photocurrent. Even though the light couples in through a 40 nm thick semi-transparent silver film, the peak light intensity near the donor–acceptor junction is comparable to that of a conventional ITO based solar cell [63][73]. Below the wavelength of the second resonant mode, there exist third and fourth resonant modes in the electric field contour, indicating possible absorption in the ultra-violet range. Thicker spacers make the peaks narrower, and push the higher resonant mode into the visible range, similar to the Fabry–Perot interferometer. The calculated EQE spectrum, plotted in **Fig. 4.2a**, shows a strong correlation with the resonant electric field. Note that the EQE spectrum of a microcavity device can be largely decoupled from the absorption spectra of the active photosensitive materials (**Fig. 4.1**), a consequence of the strong resonant effects. However, the width of the peak in EQE spectrum is hard to be separated from the absorption spectrum, which will be shown later in this section.

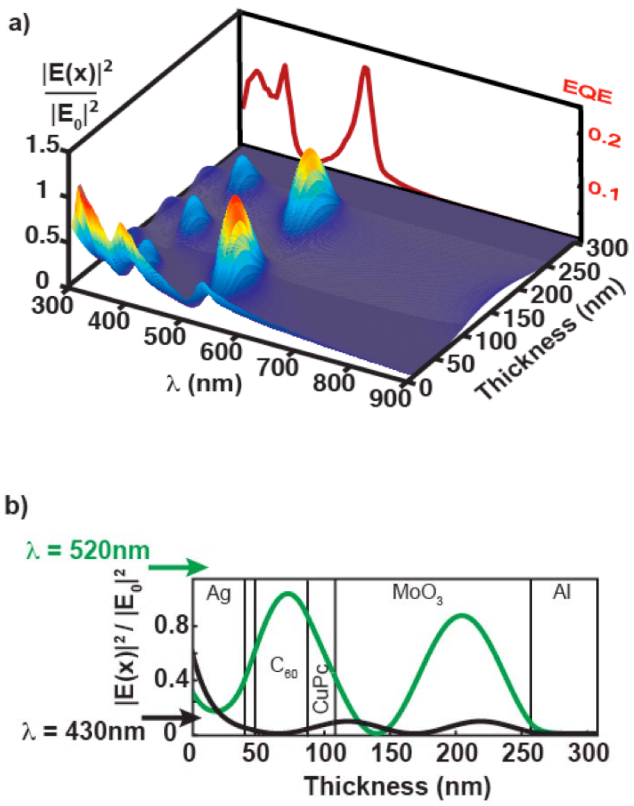

Figure 4.2 (a) Calculated electric field intensity $|E|^2$ distribution throughout the photodetector for a range of incident wavelengths. The thickness axis denotes the distance from the air–cathode interface, on which light is incident. The external quantum efficiency (EQE) is plotted also along the back plane of the graph to represent the strong correlation between $|E|^2$ and EQE. (b) A plot comparing $|E|^2$ profiles inside the OPD for 430 nm and 520 nm incident light. A strong second mode can be seen for 520 nm illumination. The device structure used in the simulation for both (a) and (b) is: 50 nm Al / 150 nm MoO_3 / 20 nm CuPc / 40 nm C_{60} / 7 nm BCP / 40 nm Ag.

Following the optical analysis, device structures were fabricated having layer sequences and thicknesses identical to those modeled (within experimental error), deposited onto 1 mm thick glass substrates using vacuum thermal evaporation (VTE) at 10^{-6} Torr and 1–2 Å/s evaporation rate. The nominal layer sequence was as follows: thick aluminum that serves as the bottom mirror and anode anode, MoO_3 optical spacer varied from 110 nm to 220 nm thick, CuPc electron donor, C_{60} electron acceptor, BCP hole and exci-

ton blocking layer, and semi-transparent silver serving as the top mirror and cathode. Cathodes were defined by depositing through a shadow-mask, which was mounted in atmosphere immediately after depositing the C_{60} layer. Device photocurrent was measured in atmosphere using a transimpedance amplifier at zero bias, with the photodetector illuminated by monochromated light from a halogen lamp; a lock-in amplifier (at 89 Hz chopping frequency) was used to enhance the signal-to-noise ratio in determining the EQE. Incident light power was measured using a calibrated silicon photodetector (Newport 818-SL). For a device having a target resonant mode at 520 nm, our calculation suggested a 150 nm thick optical spacer. This resonant peak was confirmed by EQE measurements on a fabricated device with 150 nm optical spacer thickness, as shown in **Fig. 4.3e**. Despite the accuracy of the predicted peak position, there is a mismatch in the peak height. This is due to a lowering of the cavity Q factor, most likely a result of the roughness of the evaporated metal mirrors. To include the scattering caused by mirror roughness in our optical model, we used Filinski's theory [29] of modified reflection coefficients, which accounts for phase variations resulting from small height differences by a Gaussian distribution characterized by the root-meansquare (RMS) of the film topography. Atomic force microscopy (AFM) was used to quantify the roughness of the aluminum and silver films, as shown in **Figs. 4.3a-d**. We found RMS roughness values of 14.5 nm for aluminum deposited onto glass substrates, and 7.3 nm for silver films deposited onto the organic layers. Incorporating Filinski's correction into our optical model and using these RMS values explicitly resulted in excellent agreement with experiment, as shown in **Fig. 4.3e**. In the inset of **Fig. 4.3e** we compare the sensitivity of the detector to monochromatic light at wavelengths of 430 nm and 520 nm, corresponding respectively to the valley and peak of the EQE spectrum of the heterostructure. The sensitivity ratio

for these two wavelengths was 15 at zero applied bias. Further measurements of the EQE spectra under a reverse bias of 2 V showed no changes in the wavelength peak or spectral width, although the magnitude of the peak increased slightly, as the sensitivity curve (inset of **Fig. 4.3e**) indicates.

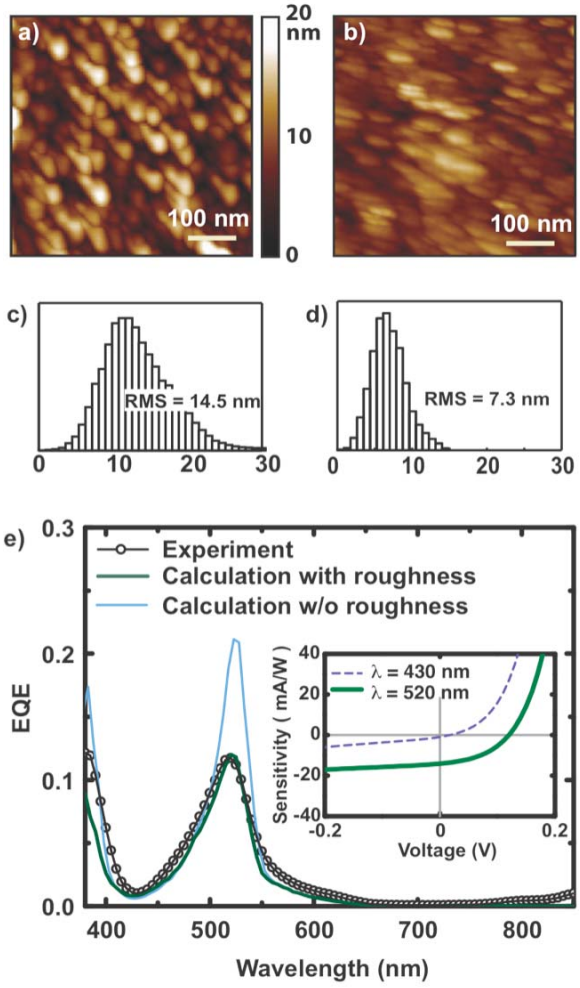

Figure 4.3 Atomic force microscopy (AFM) scans of (a) aluminum thin films deposited onto glass substrates, and (b) silver thin films deposited onto the organic layers of BCP, C_{60} and CuPc on the aluminum, along with histograms (c–d) of the measured surface height values, which exhibit a Gaussian distribution. The root-mean-square (RMS) roughness measures 14.5 nm for aluminum and 7.3 nm for silver. (e) A plot superimposing the measured and calculated external quantum efficiency spectra. Two calculated spectra are shown – one that does not take electrode roughness into account, and one that does. (inset) A plot of photodetector sensitivity for illumination wavelengths of 430 nm and 520 nm, showing clear spectral selectivity.

To further demonstrate the spectral selectivity of the microcavity-based organic photodetector, we calculated (again accounting for roughness) the position of the resonance peak for a range of spacer thicknesses between 130 nm and 210 nm, predicting that the resonance peak would span wavelength ranges from 490 nm to 620 nm (**Fig. 4.4a**). These predictions were confirmed experimentally, as shown in **Fig. 4.4b**. By varying only the optical spacer thickness in the fabricated device structures, we are able to span a 450 nm to 630 nm range with the EQE spectrum. Some discrepancy between simulation and experiment is present for longer wavelengths, attributable to two effects. Firstly, the extinction coefficients used in our model for this wavelength range are based on literature values [72]; however, these coefficients can vary in practice for deposited films due to differences in film morphology. We separately performed optical absorption measurements on Ag thin films deposited in our thermal evaporation system and found that they had a slightly higher extinction coefficient for longer wavelengths than predicted in Palik's data [72]. Secondly, we note that the two experimental EQE spectra for photodetectors with optical spacer thicknesses of 200 nm and 220 nm (dashed lines in **Fig. 4.4b**) were obtained from a heterostructure that used N,N0-di-[(1-naphthalenyl)-N,N0-diphenyl]-(1,10-biphenyl)-4,40-diamine (α-NPD) instead of CuPc for the donor layer.

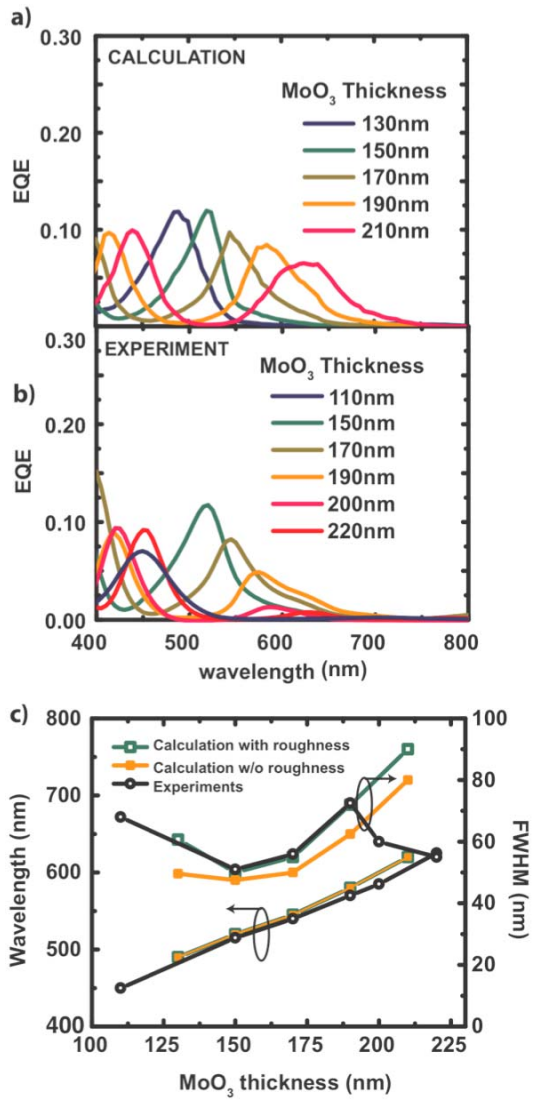

Figure 4.4 (a) Calculated and (b) measured external quantum efficiency spectra versus incident wavelength for optical spacer layers of different thickness. The calculated response predicts that the resonance peak can be shifted from 490 nm to 620 nm (corresponding to optical spacer thicknesses of 130–210 nm). The observed peak in the response shifts from 450 nm to 630 nm for spacer thickness ranging from 110 nm to 220 nm, while other elements of the OPD structure remain unchanged. (c) A further comparison between theory and experiment, plotting the peak position versus spacer layer thickness; two sets of calculated peaks are shown for calculations that either do or do not account for electrode roughness. Note that the dotted lines in (b) and the last two experimental data points in (c) were obtained from heterostructures that use α-NPD instead of CuPc for the electron donor layer, to demonstrate control of the width of the spectrum via absorber layer composition.

While substituting a different absorber demonstrates the ability to further control the spectral response, it also leads to reduced detector sensitivity, in this case due to the low intrinsic optical absorption of C_{60} and α-NPD near the second resonant peak of the microcavity mode (590 nm and 620 nm for the two dashed spectra). **Fig. 4.4c** plots the peak position versus spacer layer thickness as a more direct comparison between theory and experiment. The two experimental data points with the largest spacer thicknesses correspond to the C_{60}/α-NPD heterostructure and demonstrate the ability to significantly reduce the photodetector response peak width with proper choice of absorber. The agreement observed between model and experiment suggests that our model can serve as a viable design tool.

Optical microcavities tend to be sensitive to the angle and polarization of incident light. We calculated EQE spectra at several incident angles for a microcavity photodetector employing a 150 nm thick optical spacer. The inclined incident (and polarized) light (0˚ = normal incidence) blue-shifted the peak wavelength of the photodetector, as shown in **Fig. 4.5**, attributable to the decreased optical phase difference of reflection at higher angles, as predicted by Fabry–Perot theory. Similar peak wavelength changes were measured experimentally, as shown in the inset of **Fig. 4.5**. The absolute magnitude of the EQE was progressively smaller at oblique incidence, regardless of polarization, attributed to a combination of increased reflectivity and increased attenuation of light in the top silver electrode. As a result, variation of the EQE spectrum with incident angle is minimal. We note that, while small, this manifestation of microcavity effects at varying incidence angles could constrain some applications. It also potentially could be used as a means to actively tune the spectral response of a given OPD.

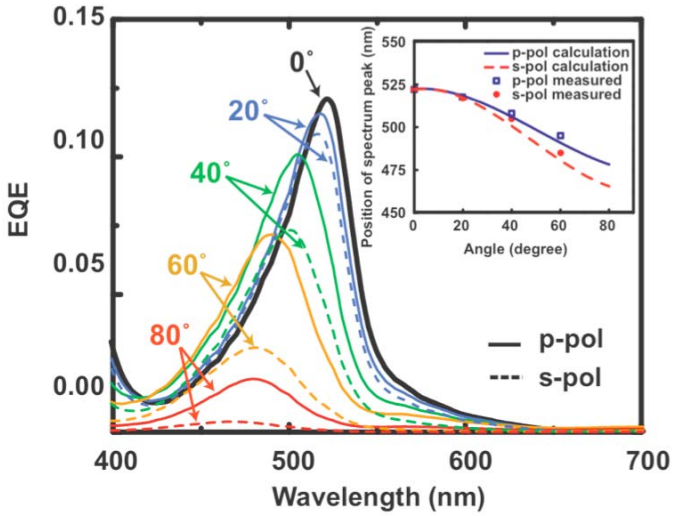

Figure 4.5 A plot of the EQE spectra for several incident angles (0˚ = normal incidence), including both p- and s-polarized light, calculated for a microcavity photodetector employing a 150 nm thick optical spacer. The peak blue-shifts with increasing angle, while the absolute magnitude of the EQE reduces at shallower incidence, regardless of polarization, due to a combination of increased reflectivity and increased absorption of light in the top silver mirror. The inset shows similar changes in peak wavelength measured experimentally.

The frequency response of a photodetector is another important design consideration; one might suspect that inserting additional transport layers in a heterostructure could significantly reduce the response time. However, we find that the insertion of MoO_3 introduces negligible delays in the response time of the detector. We measured the bandwidth of two device structures with different MoO_3 thicknesses: 50 nm Al / 150 nm MoO_3 / 20 nm CuPc / 40nm C_{60} / 7 nm BCP / 40 nm Ag and 50 nm Al / 20 nm MoO_3 / 20 nm CuPc / 40 nm C_{60} / 7 nm BCP / 40 nm Ag. These OPDs were defined by 1 mm diameter circular cathodes and were illuminated by a green LED (λ = 530 nm) with 1.3 mW/cm^2 intensity that was modulated by a function generator (Agilent 33120A). The transient OPD response for a range of load resistances was measured using a 300 MHz

bandwidth oscilloscope (Tektronix TDS3032B) as shown in **Fig. 4.6**. The bandwidth extrapolated at 50x input impedance is approximately 15 MHz. This bandwidth is significantly lower than that measured in [78] for certain devices (430 MHz), most likely due to the fact that the devices in [73] were thinner, contained multiple junctions, and were measured in reverse bias and at higher illumination intensity. Importantly, the bandwidth of our device was measured to decrease only negligibly upon the addition of the MoO_3 optical spacer (see **Fig. 4.6**), indicating that the small resistance of the optical spacer contributes very little to the RC time constant.

In summary, we developed a means for tuning the spectral response of an organic photodetector across the visible spectrum by engineering its optical microcavity through the insertion of an electrically conducting and optically transparent spacer layer. We tested this concept using a spacer layer of thermally evaporated MoO_3, which exhibits good transparency and hole transport properties that do not limit the OPD's spectral or temporal response. Our calculations of the detector's photoresponse match well with experiments, particularly when the measured roughness of the electrodes (mirrors) is taken into account explicitly. We anticipate applications of this type of tunable organic photodetector design in colorimetry, fluorescence detection, and large-area flexible imagers, and photovoltaic cells.

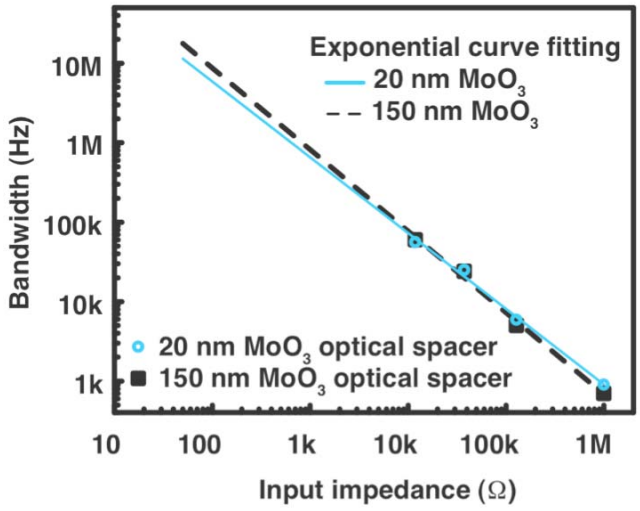

Figure 4.6 A plot of the -3 dB bandwidths of OPDs employing a thick MoO_3 spacer layer (50 nm Al / 150 nm MoO_3 / 20 nm CuPc / 40 nm C_{60} / 7 nm BCP / 40 nm Ag) and thin MoO_3 spacer (50 nm Al / 20 nm MoO_3 / 20 nm CuPc / 40 nm C_{60} / 7 nm BCP / 40 nm Ag) as measured at several input impedances by a 300 MHz bandwidth oscilloscope. A green LED (λ = 530 nm) with intensity of 1.3 mW/cm^2 was modulated in a square wave pattern, illuminating a circular device 1 mm in diameter through a focusing objective. The bandwidth extrapolated at 50Ω input impedance is ~15 MHz, and decreases only negligibly upon the addition of the MoO_3 optical spacer, indicating that the small resistance of the optical spacer contributes very little to the RC time constant.

The thin film devices discussed in Chapter 2-4 have broad applications in OLEDs, PV cells, SSL, as well as sensing and imaging. Particularly the subject is suitable for exciting dyes and detecting light. To give more functionality, such as high resolution or mapping ability for the sensing technique, a scanning probe technique will be introduced in subsequent chapters, which will discuss approaches to uniting the developed thin film techniques and the scanning probe techniques.

CHAPTER 5

SCANNING PROBE MICROSCOPY USING A MONOLITHICALLY INTEGRATED ORGANIC LIGHT-EMITTING DEVICE

Chapters 5 and 6 demonstrate how conventional OLED and organic photodetector (OPD) device structures can be adapted to a novel form factor – i.e. a scanning probe – that leverages the sensing modalities discussed in the previous chapters and enables sensing to be performed with high spatial resolution in 2 or 3 dimensions. The novel devices demonstrated here represent significant advances in the area of ultra-high resolution optical microscopy, with improved performance over existing techniques, and potentially broader scope of applicability. Chapter 5 focuses on light-emitting probes in which OLEDs are directly fabricated on commercial AFM cantilevers and used in a commercial AFM instrument. Chapter 6 focuses on a similar type of probe based on a monolithically integrated OPD. Chapter 7 discusses radically novel sensing modalities that are potentially enabled by these devices.

5.1 Introduction

Microscale optical microscopy techniques such as scanning near-field optical microscopy [12] (SNOM) have proven to have great potential for characterizing a feature that is less than diffraction limit, making use of near-field phenomena. SNOM is primarily an optically pumped technique, with the two most standard realizations being

aperture-based and apertureless probe architectures. In aperture-based SNOM, light is coupled to a sample through a subwavelength-sized aperture at the vertex of a hollow pyramid [34][55] or at the end of a pulled optical fiber with a partially etched metal cladding [12]. In apertureless SNOM probes, light typically floods a metallized probe tip that is in close proximity to the sample, exciting surface plasmons in the tip that evanescently couple to the sample over an area of subwavelength size.

Several attempts have been made to demonstrate electrically-pumped microscale light sources. Sasaki et al. [87] demonstrated a microfabricated optical probe integrated with a light-emitting diode (LED), waveguide, and aperture; the LED, however, was not monolithically integrated but rather glued to the cantilever, reducing the probe's robustness. More recently, Heisig et al. [39] demonstrated 80 nm imaging resolution using a GaAs vertical cavity surface emitting laser integrated with a GaAs cantilever. However, while III-V semiconductors have favorable light emission properties due to a direct band gap, they cannot be grown easily with high optical quality on Si or SiN_x (the most mechanically robust scanning probe cantilever materials for topographic imaging) due to lattice mismatch and the formation of antiphase domains [49]. Scanning probe cantilevers made from III-V materials are fragile, hard to fabricate, and typically show low yield [45] compared to standard Si micromachining techniques that enable batch fabrication.

In contrast, light-emitting devices based on thin films of van der Waals-bonded molecular organic compounds can be deposited onto a variety of substrates without the lattice-matching constraints of conventional covalently bonded semiconductors [18]. Furthermore, the availability of a wide range of luminescent dyes provides an additional degree of freedom in tuning the spectral characteristics of the organic light-emitting

device (OLED). These properties make OLEDs promising for integration with the well-established atomic force microscopy scanning probe platform. In the present work, we introduce an electrically pumped microscale light source based on molecular OLEDs deposited directly onto conventional silicon and silicon nitride scanning probe cantilevers.

The fabrication of an OLED directly on a scanning probe cantilever requires the ability to define an electrical contact (and hence an emissive region) that is smaller than the width of the cantilever (~30 μm) to prevent electrical shorting, and much finer still to enable high resolution imaging. This high-resolution patterning is complicated by the incompatibility of the organic active layers with typical semiconductor processing and patterning techniques. Several nanoscale OLEDs on relatively large planar substrates have recently been reported. Suh and Lee [97] demonstrated sub 100-nm vacuum-deposited OLEDs on broad-area indium tin oxide (ITO) substrates with a spin-coated and pre-patterned insulator layer. More recently, Yamamoto et al. [107] spin coated a polymer emitter into small wells in silicon nitride on a planar conducting substrate, before depositing a cathode. Boroumand et al. [15] used a combination of electron beam lithography and spin coating to make a 100 nm diameter device in a silicon dioxide well on ITO. However, surface tension effects and probe fragility render the spin coating process not well suited for placing either e-beam resist or active organic layers onto a scanning probe cantilever.

In the following sections we discuss an electrically-pumped microscale light source based on molecular organic emitters that is monolithically fabricated on a scanning probe cantilever. Such a probe can enable a new form of electrically-pumped SNOM with the advantages of improved signal-to-noise ratio and compatibility with existing atomic force microscopy tools and techniques. Furthermore, we show that the

OLED's current has a dependence on the local optical properties of a nearby sample (such as dielectric constant), making the probe a promising tool for characterizing phase separation and crystallization in materials and devices. In addition, the probe can be used to resonantly transfer singlet or triplet exciton (bound electron-hole pair) energy to a sample, enabling applications such as micro- and nanoscale characterization of photovoltaic devices and biological materials.

5.2 Organic light-emitting device on a scanning probe cantilever

5.2.1 Design of device layer structure

Prior to the fabrication of an OLED on a probe cantilever, the device structure was analyzed and designed for maximum external quantum efficiency, based on the optical and electrical simulation approach described in Chapter 2, Section 2. A bilayer structure was considered in this calculation in order to minimize parasitic recombination near the electrodes and hence increase the internal quantum efficiency. We began with a baseline structure composed of a 45 nm thick aluminum and 5 nm thick nickel anode, 50 nm thick N,N'-di-[(1-naphthalenyl)-N,N'-diphenyl]-(1,1'-biphenyl)-4,4'-diamine (α-NPD) hole transport layer, variable thickness tris (8-hydroxyquinoline) aluminum (Alq_3) electron transport and emissive layer, and 30 nm thick silver cathode after lithium fluoride (0.5 nm) and aluminum (1 nm) interfacial layer for efficient electron injection. The thickness of anode doesn’t affect considerably the calculation results as well as the electrical and optical measurement. We choose typical thickness for hole transport layer and interfacial layer for efficient electron injection. The cathode thickness can be varied to control the amount of the outcoupled top emission.

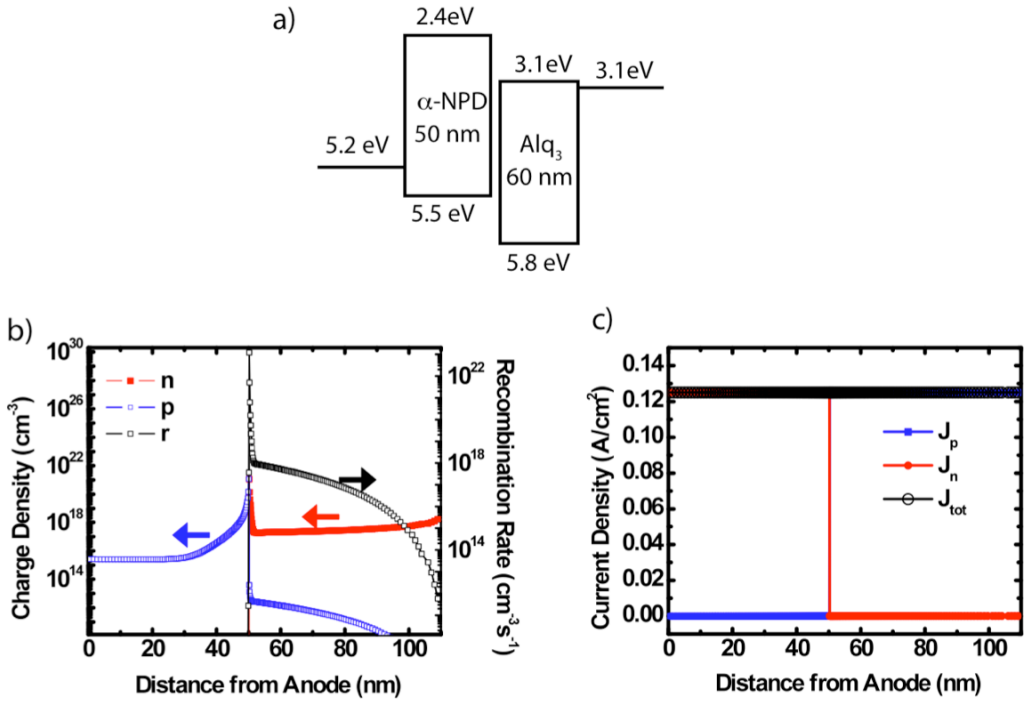

Figure 5.1 (a) Energy level diagram used for the calculation [85]. (b) Calculated charge density and recombination rate distributions in the archetypal α-NPD (50 nm) / Alq_3 (60 nm) bilayer structure at 9V bias. The recombination rate peak occurs within a few nanometers of the interface. (b) Hole, electron, and total current density. The total current density is used to check the convergence of the simulation because it is invariant through the layers. The vast majority of holes and electrons recombine at the interface, leading to negligible leakage current.

Figure 5.1 shows the calculated spatial variation of the carrier densities, electric field, and recombination rate density in the archetypal OLEDs structure. It is evident that most of the excitons are created at the organic interface, where the recombination rate is 8 orders of magnitude higher than the other region due to the energy barrier between the electron transport layer (ETL) and hole transport layer (HTL), as well as the large change in mobility at the junction for both holes and electrons.

The device layer thicknesses can be adjusted to increase the external quantum

efficiency. The electrical transport modeling results presented above suggest that the *internal* quantum efficiency is relatively constant with respect to the Alq_3 layer thickness, since most of the dipoles are created in the Alq_3, at the HTL-ETL interface. In contrast, excitons decaying at a given location in the device have different likelihoods of coupling to radiative modes in free space. As **Fig. 5.2a** shows, the *external* quantum efficiency varies periodically with Alq_3 thickness (x), mainly due to interference effects in the cavity defined by the metal electrodes. For $x < 50$ nm, the coupling of exciton energy to non-radiative decay pathways such as surface plasmon modes and lossy modes increases abruptly (as shown in **Fig. 5.2b**), resulting in a drop in the external quantum efficiency. The peak in the external quantum efficiency at $x = 75$ nm is larger than the peak at $x = 225$ nm, primarily due to parasitic coupling to the wave-guided mode (parallel to the device plane) for thicker Alg_3 layers. The optimum thickness of the Alq_3 layer for maximizing the external quantum efficiency is thus approximately 75 nm. In order to maximize emission in the normal direction (i.e. perpendicular to the device plane), the optimum thickness is 60 nm, which is slightly smaller than 75 nm, as evident in **Fig. 5.2a**. This Alq_3 thickness was used in the devices fabricated on AFM cantilevers.

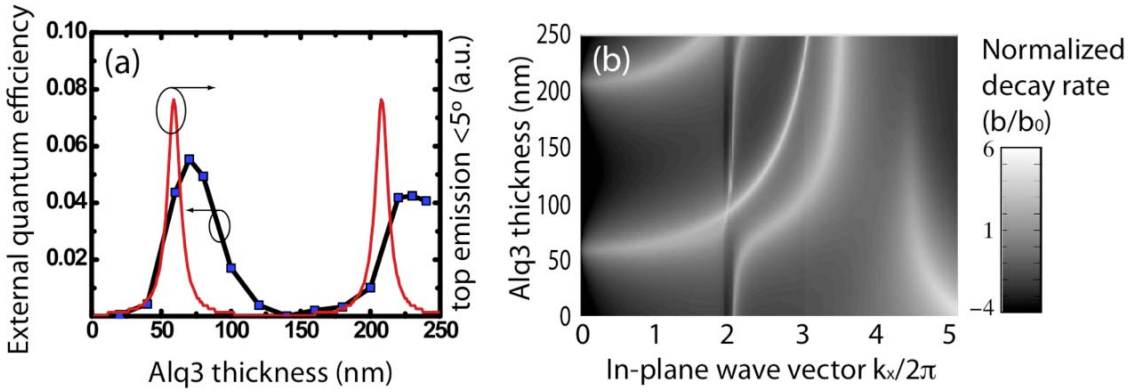

Figure 5.2 (a) Calculated external quantum efficiency of the OLED structure: Al (45nm) / α-NPD (50nm) / Alq_3 (x nm) / Ag (30nm) with varying Alq_3 layer thickness. The amount of light emission to the perpendicular direction within 5° is calculated based on the decay rate calculation. (b) Decay rate diagram of the device.

5.2.2 Fabrication of organic LED on tipless AFM cantilever (Type A probe)

Several OLED-based probe configurations are discussed below. All are fabricated on scanning probe cantilevers using vapor- and vacuum-deposited materials, while the emissive region is defined through the use of focused ion beam (FIB) milling. The three types of cantilevers used are shown in **Fig. 5.3**.

Figure 5.4 is a cut-away schematic of the emissive region of the OLED on a silicon tipless (Type A) scanning probe cantilever. The cantilevers used have an approximate width, length, and thickness of 35, 90, and 2 μm. The organic device is made, based on the calculation. The anode consisted of 100 nm thick aluminum capped by 13 nm of nickel, both thermally evaporated onto the cantilever; this was followed by a conformal 800 nm thick electrically insulating layer of vapor-deposited parylene-C [102]. The anode was deposited thicker than designed structure for better device shape after focused ion beam milling, and the thicker anode doesn't hurt the device performance. The active region on the cantilever was formed by milling the insulator with a focused gallium ion

beam (FEI 3D Dual Beam FIB) with an accelerating field for the Ga+ ion of 20 kV and an applied current of 0.76 nA. The material within the milled hole was characterized using energy dispersive x-ray detection, making it possible to mill in a controlled fashion through the parylene and only a portion of the anode.

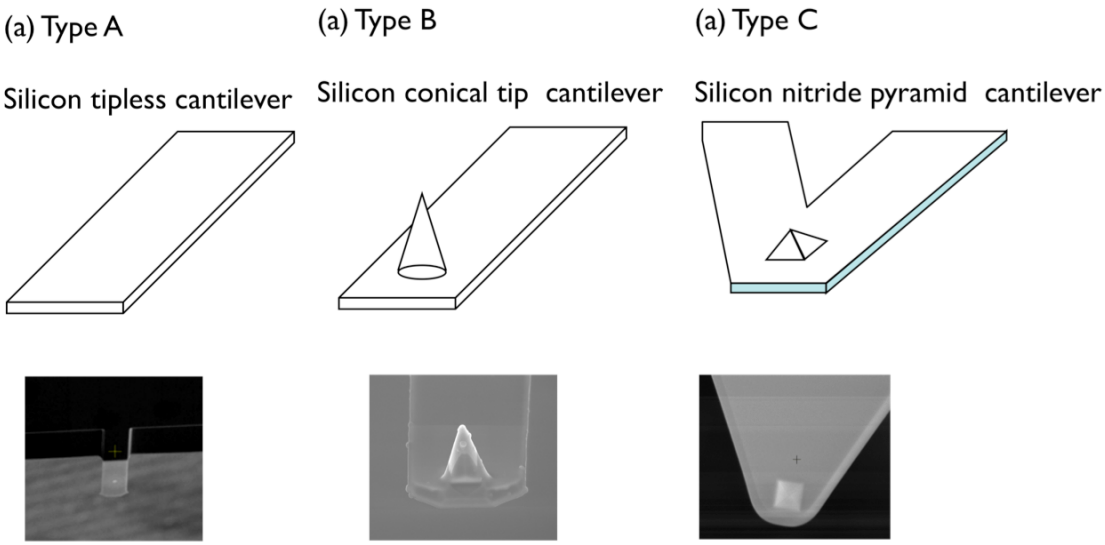

Figure 5.3 Three type of scanning probe cantilevers on which OLEDs are deposited: a) Type A – a silicon tipless flat cantilever; b) Type B – a silicon conical tip cantilever. c) Type C – a hollow silicon nitride pyramidal tip cantilever.

Following the FIB milling step, the active organic layers were deposited by thermal evaporation at 10^{-7} Torr. The hole transporting layer consisted of 50 nm thick α-NPD, while the electron transporting and emissive layer consisted of 60 nm thick tris(8-hydroxyquinoline) aluminum (Alq_3). The cathode comprises a 0.5 nm thick layer of LiF, followed by a 1 nm thick layer of aluminum [10] and an 18 nm thick layer of silver. Thinner silver cathode compared to the designed structure is chosen for higher light emission. A control sample was prepared on a scanning probe cantilever using a

deposition and processing sequence identical to that above but without the FIB milling step; the anode of the control sample is therefore separated from the active organic layers by a strong electrical insulator.

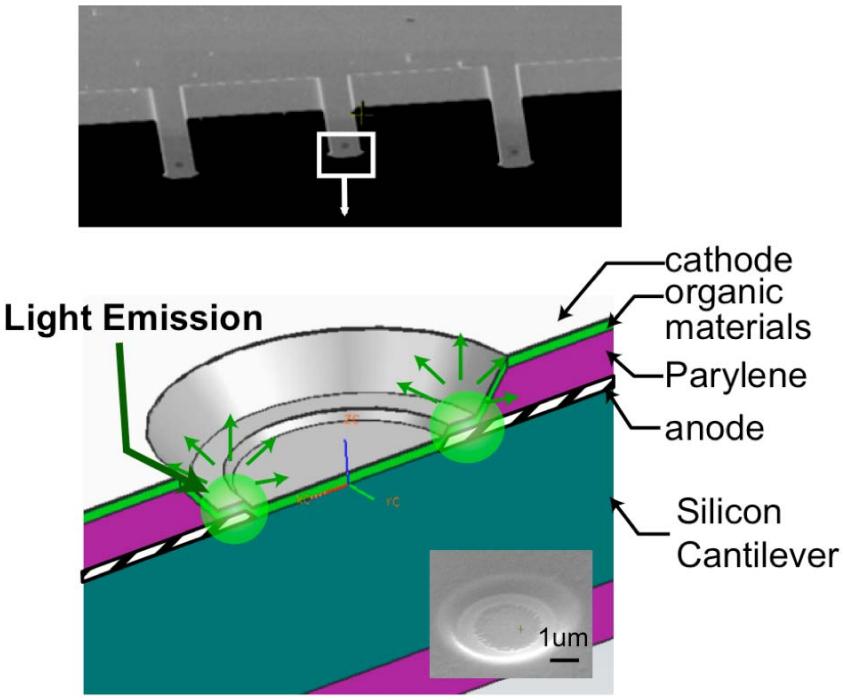

Figure 5.4 Scanning electron microscope image of Type-A scanning probe cantilevers, along with a cross-sectional illustration of an organic light-emitting device fabricated on this type of cantilever. The layer structure is Al (100 nm) / Ni (13 nm) / α-NPD (50 nm) / Alq_3 (60 nm) / LiF (0.5 nm) / Al (1 nm) / Ag (18 nm). The organic layers and cathode were deposited on the front side of the cantilever after milling the parylene insulator and anode with a focused Ga^+ ion beam.

5.2.3 Probe mounting and measurement

The probe was mounted on the nosecone of an atomic force microscope (Agilent 5100 AFM) and operated in forward bias, while monitoring the light emission through the upright microsocpe. In order to make the probe compatible with the geometry and electrical connections of the AFM probe holder, a special layer configuration and masking procedure was used as shown in **Fig. 5.5a**. Briefly, the clamp on the nosecone

was used as an electrical connection to the OLED cathode (on the top side of the probe), while a 20 μm gold wire was placed beneath the probe to connect through the low resistivity (0.05 Ω·cm) *n*-type Si probe to the OLED anode. A liquid metal electrode was made by friction-alloying indium gallium and placed between the probe and gold wire to ensure an Ohmic contact. The hole and electron paths are schematically represented on **Fig. 5.5** by dashed lines. Note that the thick anode was deposited so as to only partially cover the probe, with the rear portion of the probe masked off during deposition. To prevent electrical shorts between the anode metal and clamp used for electron injection that would occur due to the compression force of the clamp, nail polish was brushed on and dried just prior to parylene deposition. The organic semiconductor materials and cathode were deposited in a vacuum thermal evaporator through a shadow mask that prevented the materials from depositing on the probe edges, thereby minimizing the possibility of an electric short during handling or installation. Silver paste was brushed on the fragile cathode (composed of lithium fluoride (0.5 nm), aluminum (2 nm) and silver (18 nm)) before mounting the probe on the nosecone seat, in order to prevent damage by the clamp .

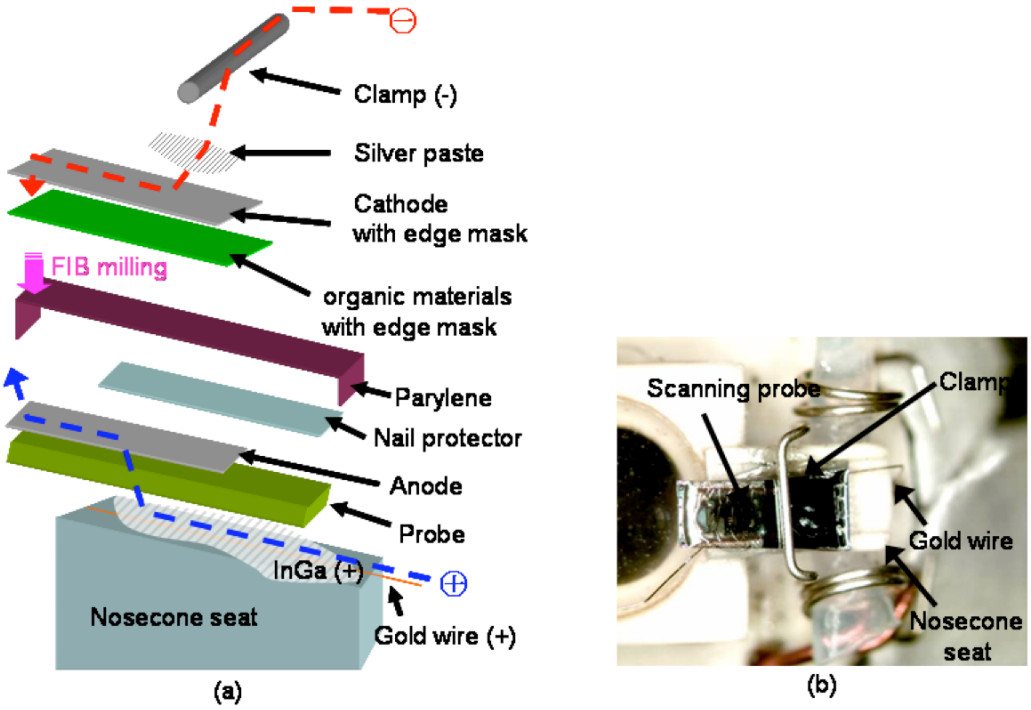

Figure 5.5 (a) Probe layers and mounting scheme. Hole and electron paths are represented by broken blue and red lines. (b) Stereo microscope picture of a probe mounted on the nosecone of the AFM.

Electroluminescence (EL) from the OLED on the cantilever was detected through an upright microscope (Olympus IX71) with a long working distance (20.5 mm) objective (50x, numerical aperture of 0.42) that facilitated making electrical connections to the device electrodes. To image light emission, a sensitive charge-coupled device (CCD) camera (Opteon LV2) was utilized in a dark room. **Figure 5.6a** shows a CCD image of an OLED near the end of a tipless cantilever under external illumination. The dark ring indicates the walls of the milled region. **Figure 5.6b** shows the EL image of the OLED in **Fig. 5.6a** under forward bias. The EL emission is ring shaped even though the milled region is a disk, because holes in the anode are preferentially injected from the nickel due to it having a higher work function than aluminum. The milling process removes the top nickel layer from the anode, leaving a ring-shaped region for hole

injection into the active organic layers from the nickel on the edge of the milled region.

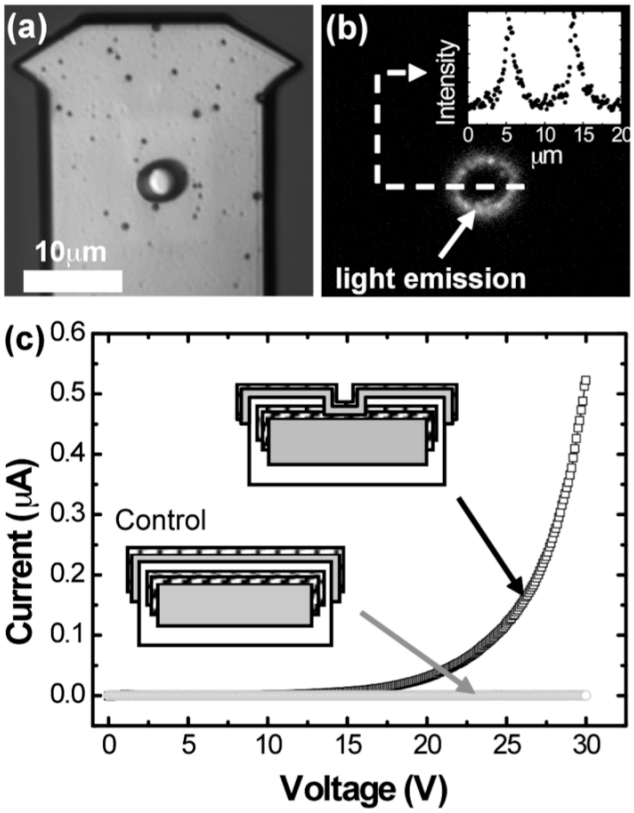

Figure 5.6 (a) Micrograph of an unbiased OLED on a scanning probe cantilever under external illumination. (b) Micrograph of an OLED scanning probe under forward bias, showing electroluminescence (EL) in the shape of a 5 μm diameter ring. A CCD camera was used to capture light emission through a 50x objective lens with an exposure time of 200 ms. The inset shows the EL intensity along the dashed line which spans the ring-shaped emission. (c) Current-voltage (I-V) characteristics of the OLED scanning probe and control sample, indicating a very low parasitic leakage current in the OLED probe.

The far-field light captured by the CCD is primarily a combination of the wave-guided emission along the sides of the milled well and the direct emission from the bottom of the well. The inset of **Fig. 5.6b** shows a cross-sectional EL intensity profile of the ring-shaped emitter. The full width half maxima (FWHM) of the emission peaks are

1.8 and 1.4 μm, respectively, as measured in the far field. Near-field enhancement of imaging resolution may occur at the top of the well, in proximity to the rim, due to the efficient coupling of energy from the electrically pumped dipoles to surface plasmon polariton modes that can propagate along the metal-organic interface [93][111]. The near-field coupling of these plasmon modes to a sample can occur at the rim of the well, in a manner analogous to plasmon/sample coupling in apertureless SNOM [4][30].

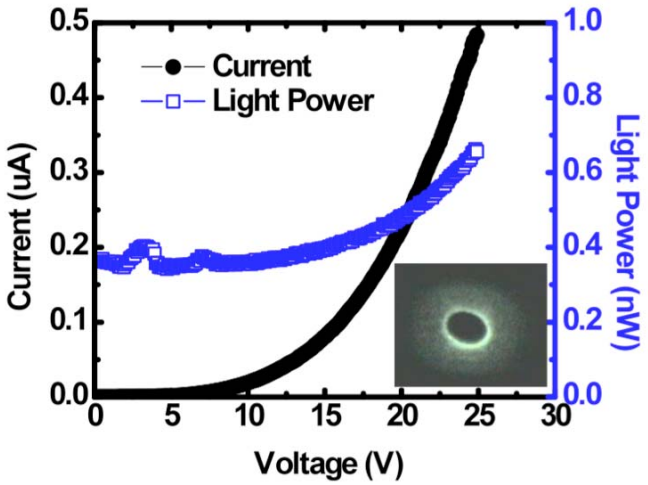

Figure 5.7 Current-voltage (I-V) and light power measurements. The voltage was swept from 0 to 25 V at 100 mV intervals while the optical power was measured with a Si photodetector. The inset shows the light emission from a probe imaged through an inverted microscope with a 60x objective lens.

The light power of the OLED probe mounted in an atomic force microscope was measured using a silicon photodetector. A semiconductor parameter analyzer monitored the device current to the OLED, and an optical power meter measured the light power emitted by the ring-shaped light source by means of a transimpedance amplifier (FEMTO DLPCA-200). The result is shown in **Fig. 5.7**. The power efficiency at 24 volts was approximately 0.006%, a relatively low value that we ascribe to the series resistance of

the Si probe, the contact resistance of the electrodes, and possible charge unbalance. The efficiency could be improved by choosing other active organic materials with different energy barrier heights, or by using an inverse OLED layer structure [110].

Each of the three cantilevers (see **Fig. 5.4**) contained an OLED, and each OLED was of identical size and shared a common anode and common cathode. All three devices were thus connected in parallel, and all emitted light simultaneously. **Figure 5.6c** compares the current-voltage (I-V) characteristics of the ring-shaped OLEDs on cantilevers with the control sample, both measured during optical testing using an Agilent 4156B semiconductor parameter analyzer. It is clear from the figure that the current passes through the OLED devices, and that the leakage current (i.e., the current through the control sample) is very small. This provides further evidence of effective electrical insulation by the parylene layer. The device emission and I-V characteristics shown here are similar for a large number of tested cantilever probes.

To summarize, the Type A probe consisted of a 5 μm diameter ring-shaped OLED (with submicron ring width) that was monolithically integrated on a commercially available AFM scanning probe cantilever. The device exhibited clear OLED-like current-voltage-luminance behavior with a very low leakage current, owing to the special masking procedure that utilized a conformally deposited parylene insulator and focused ion beam milling. The fabrication technique can be easily transferred to other cantilever substrates such as silicon nitride. OLED probes show promise for high-resolution optical imaging; in this case, if the ring-shaped light emission is used, the sample image can be reconstructed using deconvolution with a ring filter to achieve high resolution. However, note also that the flat cantilever design is likely to result in a larger-than-desired working distance from the probe to the sample. For SNOM applications, the probe-sample

distance should be less than one wavelength. The following sections describe modified probe designs that minimize this distance.

5.3 Organic LED on the tip of scanning probe cantilevers (Type B and Type C probes)

For maximum spatial resolution, the distance between the divergent light source and sample should be minimized. In this section, we describe an OLED fabricated on a tipped cantilever probe platform that used a layer structure identical to that described in the Section 5.2. A typical tip geometry used is illustrated in **Fig. 5.8a**, with approximate height, cone angle, and radius of curvature of 25μm, 30° and 10 nm. The fabrication sequence was analogous to that of the tipless probe, except that the FIB milling process was modified in 2 ways: (1) the sharp tip was truncated, as shown in **Fig. 5.8**; and (2) an accelerating field of 30 kV and applied current of 30 pA were used for FIB milling. Milling from the side of the conical tip results in a truncated tip that contains a metal ring anode, as shown in **Figs. 5.8a** and **5.8b**. Following the deposition of the organic layers and cathode, a ring-shaped light emitter was therefore formed atop the truncated conical tip (**Fig. 5.8c**). The current-voltage characteristic of this device is plotted in **Fig. 5.9**, showing typical OLED behavior with two clear regimes: ohmic ($I \propto V$) and trapped charge-limited regime ($I \propto V^m$, $m \sim 7$) [10].

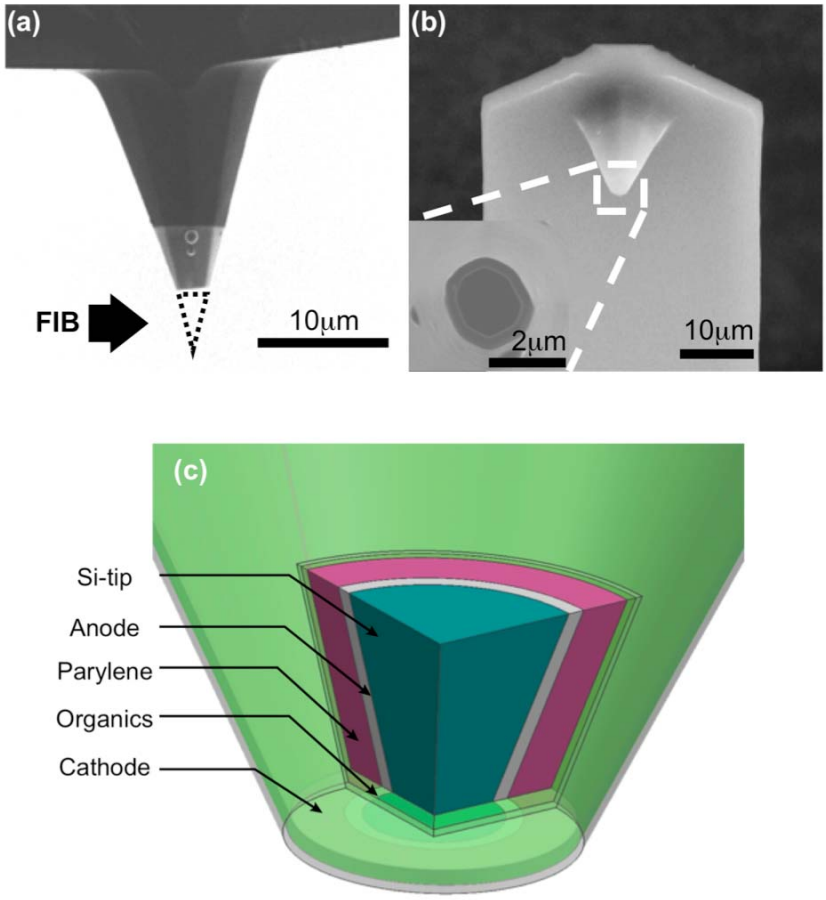

Figure 5.8 Scanning electron microscope image of the tip of a scanning probe after focused ion beam (FIB) milling. (a) Milling was done from the side of the probe rather than from the top to achieve better resolution. (b) FIB makes the tip flat with a ring-shape metal electrode exposed. The inset shows a top view of the milled surface. (c) Illustration of the completed probe after deposition of active organic layers and cathode on top of the milled probe.

The size of the OLED fabricated atop the microscale conical platform is defined by both the diameter of the platform and the thickness of the anode. The latter dimension, which is less than 30 nm, suggests a possibility of near-field optical scanning microscopy using this type of electrically pumped light source.

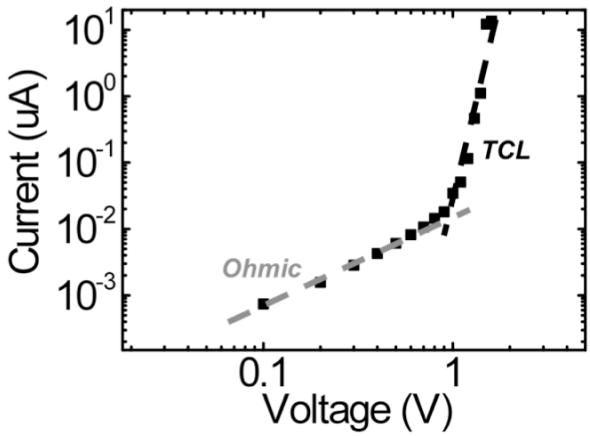

Figure 5.9 Current-voltage characteristics for the OLED on a tipped cantilever. The two operating regimes of space charge limited transport and trap charged limited transport, both characteristic of OLEDs, are clearly shown; this indicates that the OLED on the scanning probe cantilever does indeed act like a normal OLED.

Another probe design (Type C) is shown in **Figure 5.10**. Here, a hollow silicon nitride tip was used as a substrate for the fabrication of the OLED scanning probe. The approximate height of the probe tip, cone angle, and radius of curvature were 3 μm, 35° and 20 nm. The fabrication procedure was similar to that described for the two types of devices described above, except that, as illustrated in **Fig. 5.10**, the pyramidal tip was milled to expose a thin needle atop the truncated platform. This configuration can be used to simultaneously obtain topographic and optical images of a sample, with the light source maintained at a constant distance from the sample to prevent degradation.

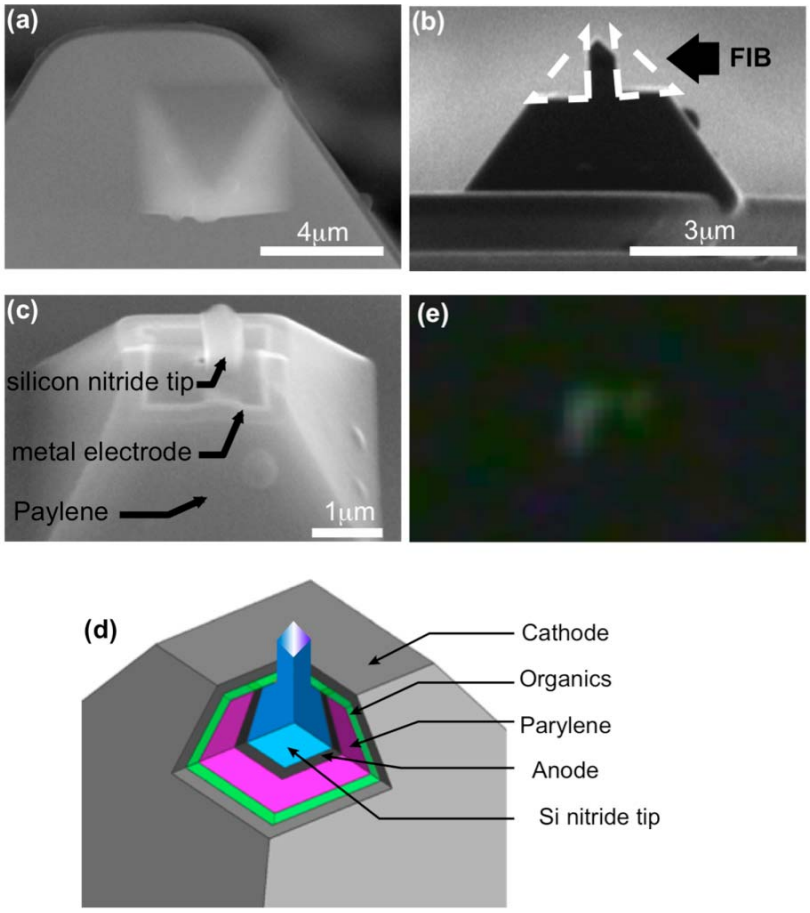

Figure 5.10 (a) SEM image of a silicon nitride tipped cantilever before FIB milling. (b) Milling process for the tip, in which two sides of the needle are milled, the probe is turned 90^{o}, and the remaining two sides are milled. (c) SEM image of the cantilever after milling. A rectangular metal electrode (anode) was exposed below the tip. The silicon nitride tip, metal electrode, and parylene insulator can be distinguished by their SEM contrast. (d) Active organic layers and cathode are deposited on top of the milled pyramid platform to complete the fabrication process. (e) Light emission from an OLED on a silicon nitride tip milled in this fashion was detected by a CCD camera connected to an optical microscope.

5.4 Summary

High resolution sensing and imaging tools consisting of submicron-scale organic light-emitting devices on scanning probe cantilevers were demonstrated in this chapter.

The emission spectra of OLED probes can be tuned across the entire visible spectrum, including white light emission, by altering the composition of the emissive layer [94]. The fabrication technique is suitable for a number of cantilever substrates including silicon and silicon nitride. In addition to probing a sample with light emission, the OLED probe can also be used to directly transfer exciton energy through the cathode to a sample via plasmon-assisted energy transfer [4]. Using the probe in this manner would be valuable for studying exciton dynamics in organic or organic/inorganic hybrid photovoltaic devices, as will be discussed in greater detail in Chapter 7.

CHAPTER 6
ORGANIC PHOTODETECTOR PROBES FOR SCANNING PROBE MICROSCOPY

The preceding chapter described a novel probe based on an OLED formed on the tip of a commercial AFM cantilever. The critical dimension of the OLED is smaller than a micrometer, suggesting promise for ultra-high-resolution optical microscopy and sensing applications. This chapter describes a submicrometer scale organic photodetector realized on an AFM probe tip, and demonstrates nanoscale scanning resolution using the device mounted in a commercial AFM instrument.

6.1 Introduction

The ability to reliably perform optical and topographic imaging simultaneously is an important challenge for microscopy and can be useful, for example, in studying cell membrane transport processes in biological systems. Near-field scanning optical microscopy [12] (NSOM) has been shown to achieve optical imaging with spatial resolution that surpasses the diffraction limit of conventional optics, and has been employed in studies of nanoscale processes in optoelectronic materials and devices, as well as biological systems. However, several practical limitations currently exist. Aperture-based NSOM probes (e.g., pulled optical fibers) often suffer from low optical transmission coefficients on the order of 10^{-9}–10^{-5} [37]; increasing optical output power

leads to excessive probe heating that can damage samples and reduce probe reliability [50][96]. Apertureless NSOM techniques have also been developed, but limitations such as low signal-to-noise ratio and optical alignment still arise from having to collect the signal using far-field optics [8][36][44].

To circumvent the problems associated with strong signal attenuation and far-field detection, several groups have attempted the fabrication of active cantilevers that bring an electrically-pumped, nanoscale light emitter or photodetector directly into the near field of a sample. The external quantum efficiency of light emitting devices (LEDs) and photodetectors can exceed 10^{-1}, making the signal-to-noise ratio (SNR) of such methods potentially much higher than existing NSOM approaches. Heisig et al. [39] demonstrated 80 nm imaging resolution using a GaAs vertical cavity surface-emitting laser integrated with a GaAs cantilever. However, due to lattice mismatch and the formation of antiphase domains [18][49], these devices cannot be grown easily with high optical quality on silicon, the most common and robust material for atomic force microscopy (AFM) cantilevers. Davis et al. [25] fabricated a Schottky photodiode having a very small (100 nm) optically sensitive region on a silicon cantilever, and demonstrated optical imaging with a high resolution similar to the size of the diode aperture. Hoshino et al. [42] demonstrated near-field imaging results using a monolithically grown silicon light emitting diode on a scanning probe tip. These probes demonstrate improved SNR over existing NSOM approaches and may be cost competitive with aperture and apertureless NSOM. However, their limited spectral selectivity precludes their use in important applications such as fluorescence microscopy, and leaves considerable room for further development of probe architectures and materials combinations.

Previously, we have developed probes in which organic LEDs were fabricated on

commercially available silicon AFM cantilevers [3][110]. The use of organic-based optoelectronic devices is motivated in part by the ability to deposit device-quality thin films onto a variety of substrates without the need for lattice matching, and also by the ability to incorporate compounds with desired spectroscopic properties into the active layers. The latter approach can be used to avoid background noise due to absorption of the AFM's positioning laser and sample fluorescence. In the following section, the probe configuration and fabrication are discussed in detail.

6.2 Photodetector on a scanning probe

The organic photodetector (OPD) used in this study [2] was fabricated using a combination of methods similar to those described in Chapter 5 for the fabrication of OLED-based probes [3][110]. Briefly, the OPD probe consisted of molecular organic thin films sandwiched between thin-film metallic electrodes, all deposited onto a conventional AFM cantilever using vacuum thermal evaporation. The anode consisted of aluminum evaporated onto a thin nickel adhesion layer which was pre-deposited on the Si cantilever substrate. Parylene was deposited onto the cantilever by a chemical vapor deposition process, covering the entire probe surface and forming an electrically insulating film. Focused ion beam (FIB) milling was then used to define the working area of the device by cutting off the vertex of the pyramidal tip and exposing the anode, as shown in **Fig. 6.1**. After the subsequent deposition of the active organic layers and cathode, this exposed anode on the tip effectively defines the current collection and sensing regions. By precisely controlling the width and position of the beam during the milling step, a very small photodetector can be formed. **Figure 6.1a** clearly shows the exposed metal anode ring after FIB milling; for this probe, the ring diameter was 500 nm and the ring

width was 150 nm. To complete the probe, active organic compounds and a thin silver cathode were evaporated onto the substrate. The active organic layers consist of N,N'-di-[(1-naphthalenyl)-N,N'-diphenyl]-(1,1'-biphenyl)-4,4'-diamine (α-NPD) and C_{60}, forming a heterojunction. The former compound was used to minimize parasitic optical absorption from the laser (λ=675 nm) used in the AFM's deflection feedback system. Bathocuproine was deposited between the C_{60} and cathode as an exciton blocking and buffer layer [75]. The total thickness of the photodetector was approximately 85 nm. The finished probe was mounted in a commercial AFM system (Agilent 5100 AFM) for testing as illustrated in **Fig.6.2**. During scanning, the outer electrode of the probe contacts the sample as shown in **Fig. 6.1b**, and optical excitation of the active organic layers generates excitons, which are subsequently dissociated at the α-NPD/C_{60} heterojunction, producing photocurrent in proportion to the optical signal intensity.

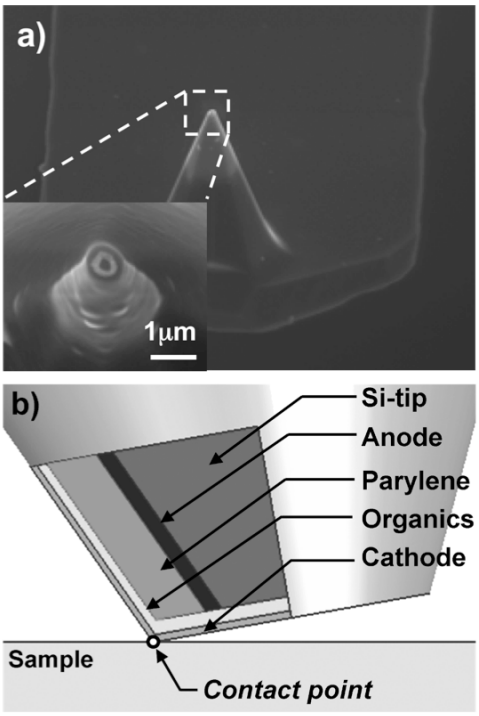

Figure 6.1 a) A scanning electron micrograph of an AFM cantilever after focused ion beam (FIB) milling of the tip vertex, on which the metallic anode and parylene insulator were previously deposited. Inset: a detailed view of the exposed ring-shaped metal anode with 500 nm diameter and 150 nm width. b) A cut-away schematic of the organic photodetector deposited on a Si AFM tip, illustrating the probe orientation relative to the sample during scanning.

Most commercial AFM systems have a sensitive current measurement module for performing scanning tunneling microscopy or current sensing AFM. The current measurement module in the Agilent 5100 has a 10^9 V/A transimpedance amplifier that is suitable for measuring electrical current from the probe, with sensitivity in the pico-ampere range. The AFM scanner on which the probe is mounted can move the tip with nanometer precision and potentially enables the photodetector to detect light with similar spatial resolution. The laser feedback system maintains constant deflection of the cantilever and thereby provides a simultaneous measurement of the sample's topography.

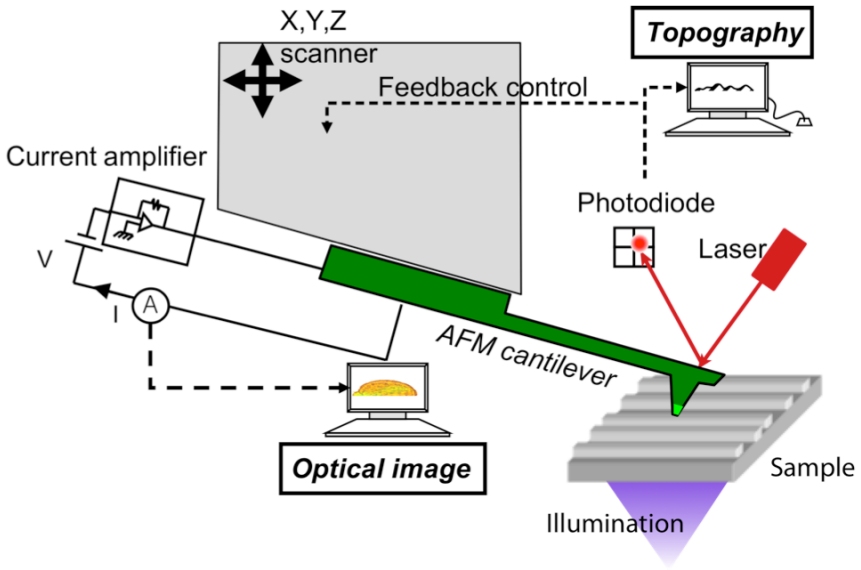

Figure 6.2 Schematic view of a scanning optical microscopy apparatus based on an organic photodetector probe. The system is built on a commercial atomic force microscope (AFM) platform, making use of a current amplifier, piezoelectric scanner, and laser-based positioning system. The AFM cantilever mounted on the system has a sub-micrometer scale organic photodetector on the tip of the probe, and the current sensing module measures photocurrent during scanning in contact with samples. The positioning system contains a laser (λ = 675 nm) and photodiode that detect the deflection of the cantilever to measure topography during scanning. Thus, the system is capable of measuring optical signals and topography simultaneously.

The probe was tested by scanning a 10x25 μm^2 rectangular aperture created by FIB milling a 20 nm thick silver film [see **Fig. 6.3a** inset]. During scanning, a portion of the tip was in contact with the sample, as illustrated in **Fig. 6.1b**, maintaining constant contact force. While a portion of the probe touches the sample, there is a 500 nm or smaller gap between the photodetector and the sample. (Note that both this gap and the photodetector diameter can be made smaller, potentially less than 50 nm [34], by more precise FIB milling.) During scanning, the photodetector was reverse biased at a constant voltage, while the aperture was illuminated from below using a wideband mercury lamp

behind a 460–490 nm bandpass filter. **Figure 6.3a** shows the topography of the sample and **Fig. 6.3b** shows the optical image, both acquired simultaneously. The aperture can be clearly seen in the optical image as a bright region, corresponding to the transparent (milled out) portion of the sample. **Figure 6.3c** is a line profile of the aperture region, and **Fig. 6.3d** is the optical signal obtained during a line scan along the dashed line shown in **Fig. 6.3c**. Because FIB milling of the aperture produces silver redeposition near the cutting region, along with a slightly sloped aperture wall, neither the topographic nor the optical signal has a sharp cutoff in the vicinity of this tapered edge. However, by comparing the optical and topographic line profiles, we deduce the spatial resolution of optical image to be better than one micrometer. This sub-micrometer resolution is consistent with the size of the detector and the separation between the detector and sample due to the device thickness and probe tilt. As indicated by the uniform intensity distribution in **Fig. 6.3b** and the photocurrent versus time plot in **Fig. 6.3e**, there was no degradation of the probe during the contact-mode scan.

To confirm that the current signal from the probe is indeed due to photocurrent induced by the light transmitted through the sample (and not, for example, due to the mechanical deformation of the organic layers or the scattered red light of the AFM's positioning laser), the blue light used for illumination was turned on and off twice during a single scan. **Figure 6.3a** confirms that the probe photocurrent response tracks this optical input and is not influenced by the topographic features. The current-voltage characteristics shown in **Fig. 6.3b** clearly demonstrate that the probe detects only the blue light from the filtered mercury lamp and not the red light of AFM's positioning laser. Note that there is relatively high apparent dark current at zero voltage bias, attributed to the design of AFM's transimpedance amplifier, which produces a constant ~80 pA offset

when the AFM's positioning laser is turned on. This offset is clearly seen in the inset of **Fig. 6.3b**, where the measured current-voltage characteristic of a 10^9 Ω resistor is shown when the positioning laser is on and when it is off. For these measurements, the laser spot was moved far away from the resistor in order to confirm that the offset is due to the amplifier circuit rather than light absorption in the resistor. This constant offset does not impact the operation or sensitivity of the photodiode, which is held at constant voltage bias during scanning.

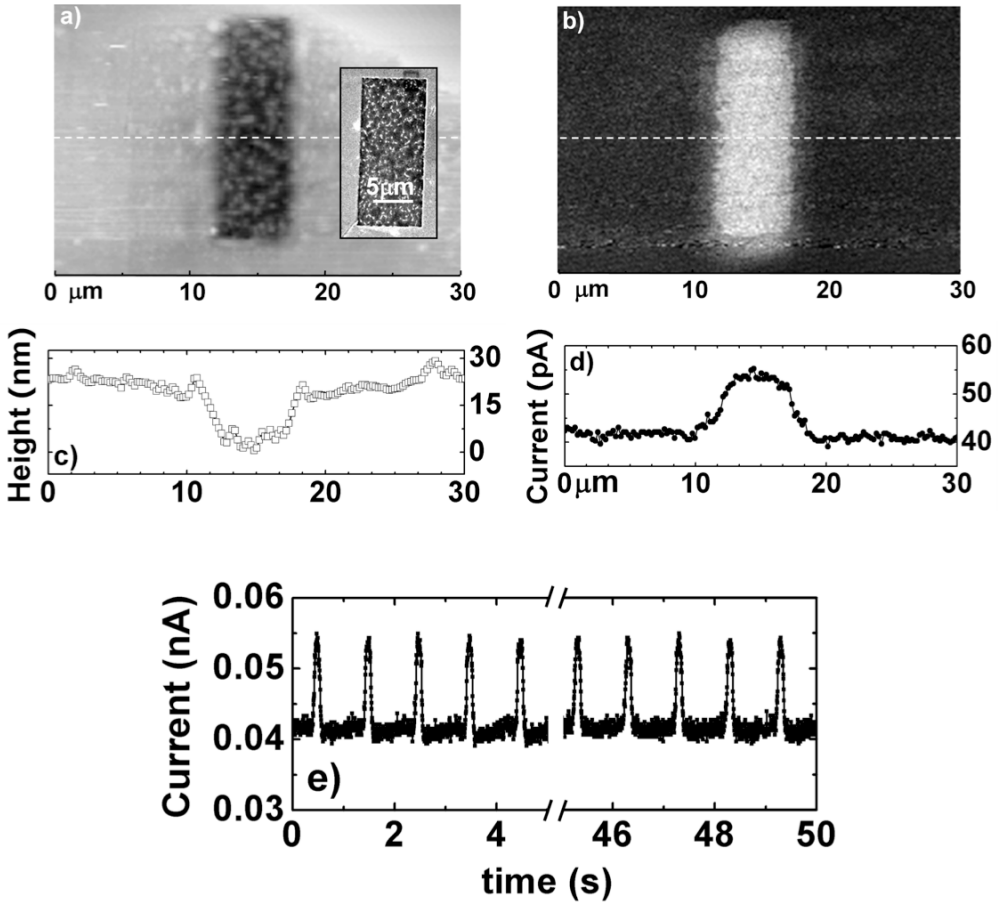

Figure 6.3 a) A topographic scan of an aperture made by FIB milling a thin silver film on glass. Inset: SEM image of the 8×20 μm^2 aperture. b) Optical (photocurrent) image of the back-illuminated aperture, acquired simultaneously with the topographic scan. c) Height and (d) Photocurrent data along the dashed line shown in (a) and (b). e) A plot of the probe photocurrent versus time during the scan, indicating no noticeable degradation of the probe.

The spectral sensitivity and selectivity of the photodetector can be further engineered by selecting active layer materials having desired absorption spectra from the large existing library of molecular organic compounds. Alternatively, the layer structure of the photodetector can be configured to optimize optical microcavity effects, which have been shown to strongly influence the spectral response of OPDs [1][53]. Taking advantage of optical microcavity effects can potentially broaden the application area of the probe to include, for example, high-resolution fluorescence microscopy of biological systems and other metrology applications.

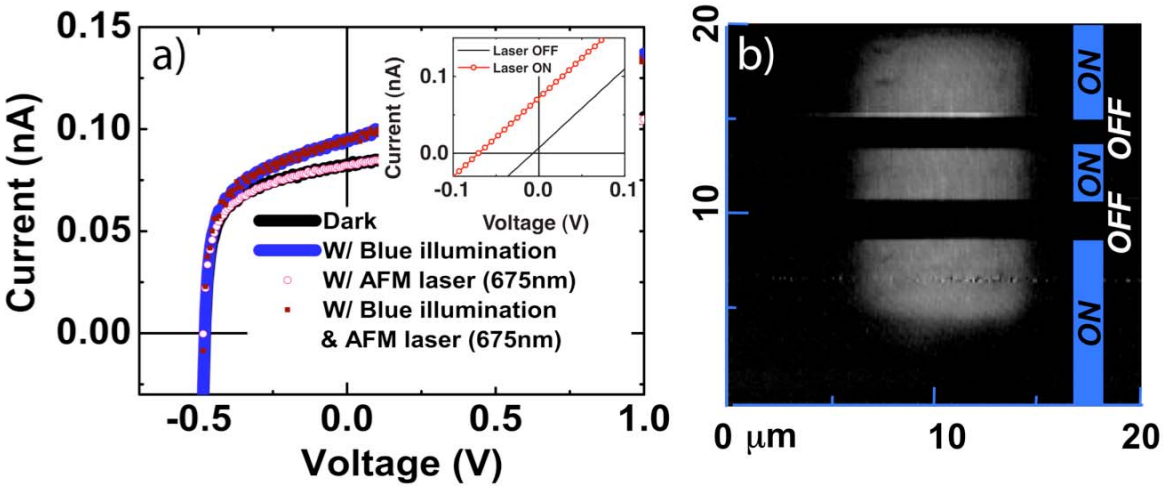

Figure 6.4 a) Current-voltage characteristics for the submicron photodetector under several different illumination conditions, demonstrating that the probe does not suffer from parasitic absorption of the AFM's positioning laser at λ=675 nm. Inset: Current-voltage characteristics for a 1 GΩ resistor demonstrating the constant current offset inherent in the transimpedance amplifier circuit when the positioning laser is turned on. This does not affect the operation of the probe, which is held at constant voltage bias. b) An optical scan of the back-illuminated aperture in which the illumination was turned on and off during scanning as indicated on the right side of the image. This demonstrates that the current signal from the probe is indeed due to photocurrent induced by the light from the sample and not a spurious signal caused by mechanical deformation of the device.

We note that the probe discussed thus far does not at present exceed the spatial resolution of commercially available near-field optical microscopes or far-field confocal microscopes. Nevertheless, it does provide sub-micrometer spatial resolution with simultaneous topographic imaging in a convenient probe form factor. Sub-wavelength spatial resolution of visible light signals may be achieved by decreasing the size of the photodetector on the cantilever (e.g., via precise FIB milling [34]). A potential advantage of the probe described here over conventional NSOM probes is that it enables direct local detection of the optical field, which leads to a higher collection efficiency. Based on the test represented by **Fig. 6.4**, we determined a SNR of 17 for the probe while using 19.2 W/cm^2 incoherent "bottom" illumination with a signal integration time of 1.95 ms. Note that this high SNR ratio is achieved without the use of a lock-in amplifier. Future measurements varying illumination intensity, probe area, and probe temperature will provide a better understanding of the relative magnitudes of the sources of noise in the probe (such as shot noise, dark current noise, and readout noise). Note that current literature does offer extensive studies of noise in OPDs.

The probe structure discussed above serves as a powerful design platform and is capable of achieving much higher imaging resolution, as discussed in the following section.

6.3 High-resolution scanning microscopy

Using a probe configuration similar to the one discussed above, the best spatial resolution of optical imaging observed in our laboratory was as high as 50 nm [113]. The probe used for this measurement was fabricated as described above, but used a 700 nm

thick parylene insulator. Focused ion beam (FIB) milling was used to make a 200 nm diameter anode at the center of the milled tip, as shown in **Fig. 6.5a** and **Fig. 6.5b**. On top of the exposed metal, 20 nm α-NPD, 45 nm C_{60}, 6 nm BCP, and 20 nm Ag were deposited in a vacuum thermal evaporator, completing the device. The resulting layer structure is schematically shown in the cutaway diagram of **Fig. 6.5c**. The active sensing area, where excitons are formed and dissociated, is located at the center of the tip and has a roughly circular disk shape that is 200 nm in diameter.

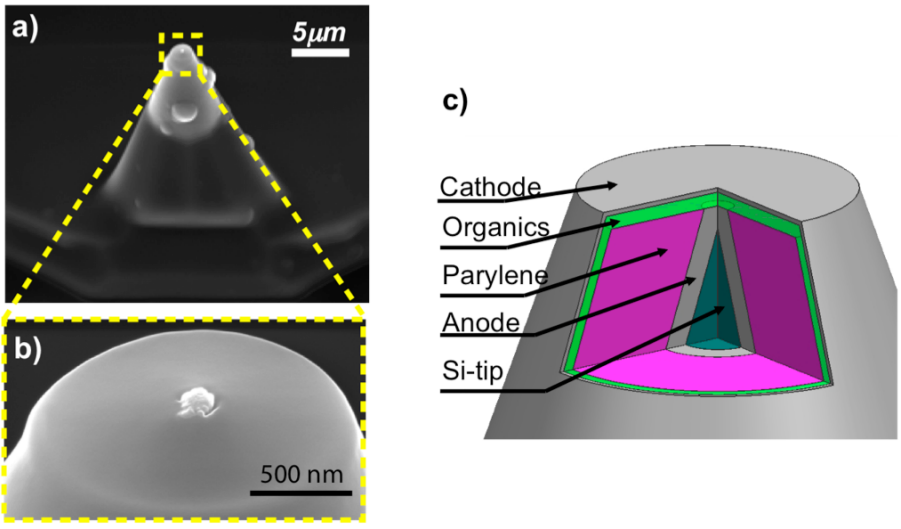

Figure 6.5 a) Scanning electron micrograph of the AFM tip after focused ion beam milling of the parylene layer, exposing a small region of the anode that is underneath the parylene. The exposed anode region is ~200 nm in diameter, and can be seen in greater detail in (b). c) Cut-away schematic of the photodetector fabricated on the silicon tip. The active sensing area, where excitons are formed and dissociated, is located at the center of the tip, forming a disk 200 nm across.

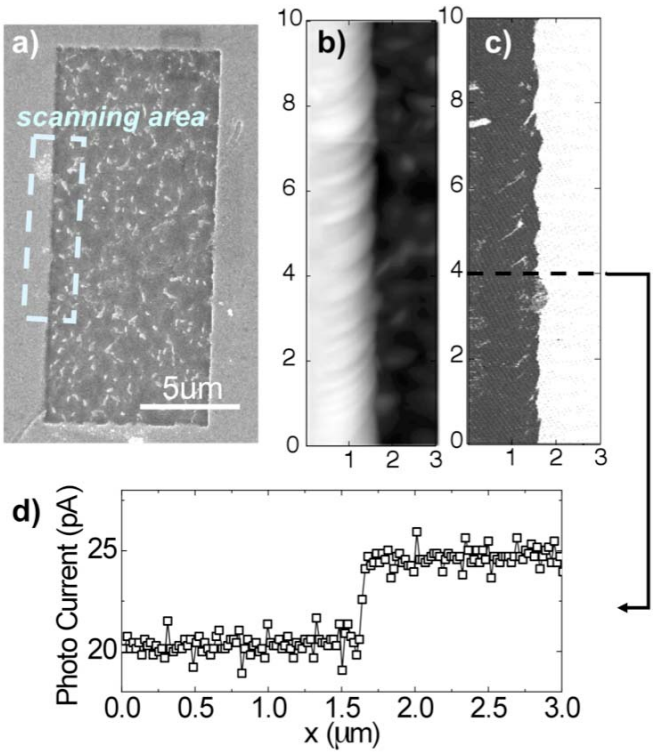

Figure 6.6 a) Scanning electron micrograph of the scanning area of the testing sample. The 20 nm silver film is milled by focused ion beam in a rectangular shape to make a 8 μm x 20 μm rectangle area. The transmittance changes rapidly on the borders of this shape, enabling measurement of the probe's optical image resolution. b) Scanned topography results (3 μm x 10 μm) and c) Scanned optical image simultaneously obtained with the probe. d) Scanned current data from the photodetector for the line shown in c). Across the boundary of the milled area, a sharp change in photocurrent is measured, from which can be derived a probe spatial resolution of 50 nm.

The probe was installed in the AFM system using the specially developed mounting procedure described in Chapter 5, and was subsequently used to scan an aperture made by FIB milling of a 20 nm thick silver film on a glass substrate (**Fig. 6.6a**). The photocurrent signal (**Fig. 6.6c** and **6.6d**) abruptly changes at the borders of the milled region, suggesting an imaging resolution that is far better than previously observed. Fitting a Gaussian shape to this signal change quantifies this resolution as 50 nm.

Remarkably, a feature has been resolved that is smaller than the working area (anode size) of the probe.

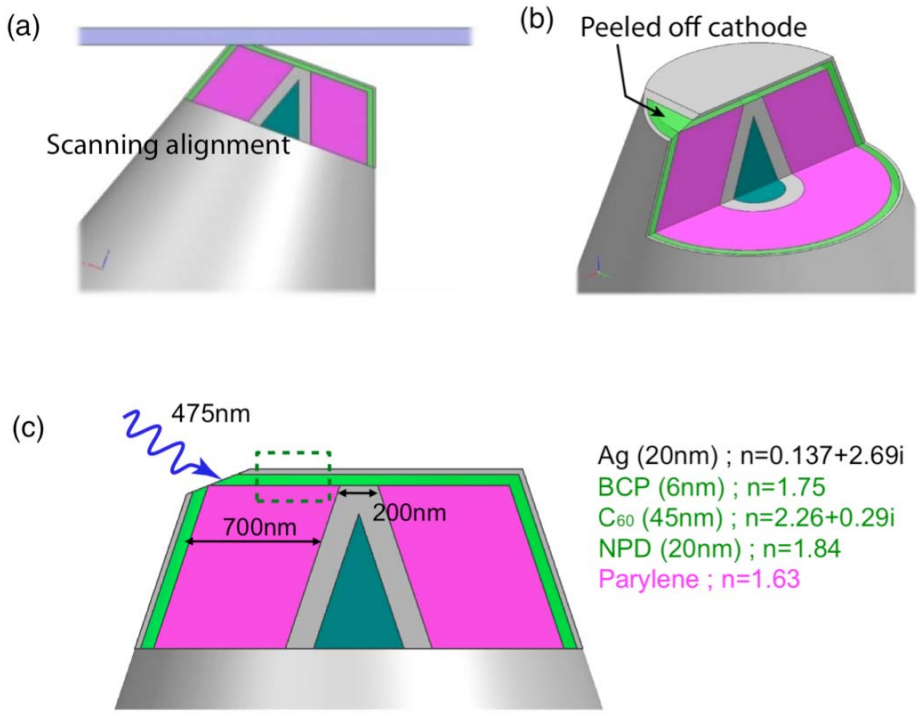

Figure 6.7 a) Illustration of the alignment of the probe with respect to the sample during scanning. The probe contacts the sample with the one end of the cathode edge at roughly 20˚ inclination. (b) While scanning in contact mode, one edge of the cathode is peeled off by mechanical friction or accidental damage. (c) Light from the sample is coupled to the structure consisting of parylene, active organics, and metal cathode. This layer structure is used below for calculation of the dispersion relation and power flow, to identify possible waveguided modes that are supported.

To further investigate this unanticipated and significant result, the actual scanning alignment is analyzed in more detail. As illustrated in **Fig. 6.7a**, during a scan the probe contacts the sample at an incline, with the circular cathode making tangential contact with the sample. The probe's plateau is at ~ 20˚ inclination with respect to the

substrate plane. It is likely (and indeed, has been observed in the lab) that the scanning motion and resulting friction between the probe and the sample rub off part of the cathode, creating an aperture (**Fig. 6.7b**). It is thus possible for light to couple directly into the device through this aperture and be waveguided to the sensing region near the exposed anode.

To examine the delivery of light through this aperture and waveguide, the models developed in Chapter 2 are now applied to the present structure (**Fig. 6.7c**). For simplicity, one dimensional system is assumed. **Figure 6.8a** shows the calculated dispersion diagram of the structure. There is a readily apparent surface plasmon mode, along with several waveguide modes near the light line in the parylene layer. The light source for the measurement has a peak wavelength of 475 nm; at this wavelength, there is considerable power decay between the regions corresponding to the air light line and the NPD light line, suggesting appreciable optical waveguiding in the organic layers. For the point on the dispersion diagram marked by a star (just right of the parylene light line in **Fig. 6.8a**), the electric field along the z-direction is calculated and overlaid on the layer structure in **Fig. 6.8b**. The field is confined within the organic layer, although some field penetrates the metal cathode and decays into the air. In addition to optical waveguiding of the 475 nm light, we also examined propagation of the supported surface plasmon polariton (SPP) mode with a peak at λ = 475 nm. Due to the high in-plane wave vector and substantial loss in the metal, we find it unlikely that the SPP propagation length is sufficiently long to deliver the incident energy 700 nm to the sensing region.

Several optical images acquired experimentally using this probe support the mechanism elaborated above. The photocurrent generated by the probe having a 200 nm diameter active region is due to absorption of both the waveguided mode and the leaky

mode that penetrates through the metal cathode. The contributions to photocurrent from these two modes give overlapping dual and sharp images, as shown in **Figure 6.9** for the silver thin film aperture.

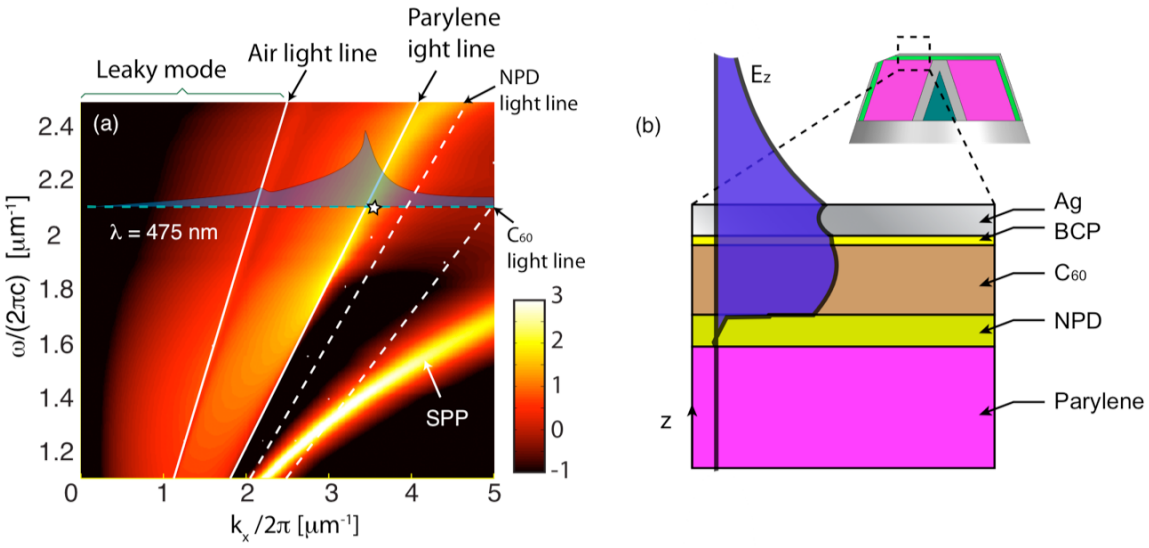

Figure 6.8 a) Calculated dispersion diagram for the structure of **Fig. 6.7c**. Note that the light source has a peak wavelength of 475 nm, corresponding to the horizontal dashed blue line. Where this line intersects the light lines, there are strong waveguided modes supported in the parylene and active organic layers. While high intensity is visible between the air light line and the parylene light line (corresponding to the waveguided mode in the thick parylene), the region *between* the parylene and NPD light lines corresponds to the mode waveguided in the active organic layers. For the point marked with star in (a), the electric field component along the z-direction is overlaid on the layer structure in (b). The field is largely confined within the active organic layers, with some of the field penetrating the metal and decaying in the air.

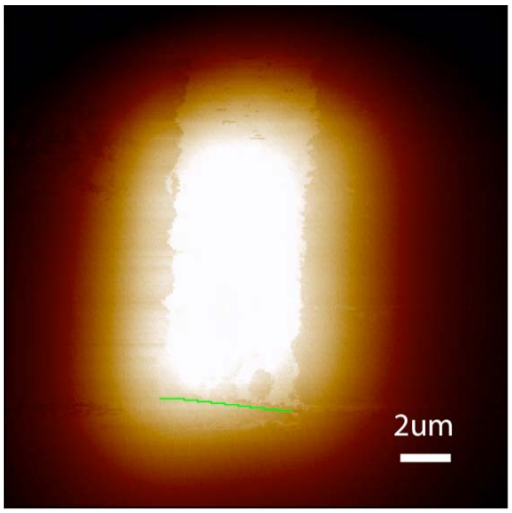

Figure 6.9 Scanning optical image obtained with the probe described above, showing a superposition of two simultaneous methods of light delivery to the active region, one at low resolution (from scattered light leaking through the metal directly), and one sharp (from the waveguided mode supported by the structure).

6.4 Summary

This chapter described novel submicrometer-scale organic photodetector devices fabricated on commercial AFM probe tips. The probes were used for the first time for scanning optical microscopy, showing remarkable imaging resolution in dual (optical and topographic) imaging mode. The device showed a reasonable (i.e. sub-micrometer) resolution when detecting primarily the light penetrating through the thick metal cathode – an imaging resolution that is comparable to the size of the working region of the probe. By introducing waveguided modes into the detection scheme, high resolution scanning optical microscopy is possible. Specifically, a 50 nm spatial resolution was observed in the optical imaging mode using incident light having 475 nm peak wavelength, demonstrating resolution beyond the diffraction limit.

The devices described have applications in imaging nanostructured semiconduc-

tor [9], ferromagnetic [27], photonic [58][16], biological [26], and single molecule [11] systems with nanoscale resolution. Combining the microcavity thin film technology developed in Chapter 4 with the photodetector platform, a tool for high-resolution scanning fluorescence microscopy is achievable that can simultaneously provide topographic data and optical images with sub-diffraction-limit resolution.

CHAPTER 7

SUMMARY AND SUGGESTIONS FOR FUTURE WORK

7.1 Summary of present work

This thesis presented several novel organic optoelectronic devices capable of optical and chemical sensing. Leveraging the relatively weak Van Der Waals bonding of molecular organic semiconductors and the ability to deposit high quality thin films on a variety of substrates, novel devices were demonstrated in conventional thin-film form factors as well as non-planar probe architectures.

The physical principles of operation of these novel devices were elucidated in Chapters 2 and 3, using electromagnetic and transport theories that were adapted specifically to the unique characteristics of thin optical microcavities, disordered organic materials, and noble metal electrodes. Owing to the low refractive index of organic compounds and the strong coupling between molecular excitons and surface plasmon polaritons supported by device electrodes, it was possible to design devices that support electrically pumped excitonic energy transfer across a thick metal film – an exciton transfer mechanism demonstrated for the first time in this work. Moreover, the fundamental physics considered in Chapters 2-3 can be applied readily to improve the performance of OLEDs, PV cells, and solid-state lighting.

The tunable organic photodetector discussed in Chapter 4 made use of highly absorbing organic materials with narrow absorption bands. Since the thin film tunable

photodetector is mechanically flexible, it can be applied in different (and perhaps broader) contexts than conventional (e.g. silicon or III-V based) photodetectors, such as fluorescence detection in microfluidic devices or large-area and flexible color imagers.

Making the leap beyond conventional planar device architectures, novel devices consisting of OLEDs and PV cells were built on the tips of otherwise conventional, commercially available scanning probes. As demonstrated in Chapters 5 and 6, these probes can be used for simultaneous high-resolution imaging in optical and topographic modes. In some instances, distinct advantages are obtained over existing, conventional probe-based imaging techniques.

Together, the theoretical developments and experimental demonstrations described in the preceding chapters serve as a strong platform that enables a multitude of potential applications in optical microscopy, excitonic scanning microscopy, and surface plasmon-emitting devices. Combining the novel sensor architectures based on vacuum- or vapor-deposited thin film organic compounds, and state-of-the-art micro- and nano-fabrication techniques for building nanoscale optoelectronic devices on non-planar substrates, many other innovative devices can be developed. The following sections present a few ideas for future research directions that leverage the developments presented thus far.

7.2 Suggestions for future work

7.2.1 Evanescent wave generator for high resolution microscopy

The phenomenon of excitonic energy transfer across a thick metal film described in Chapter 3 suggests the development of an integrated thin film evanescent wave generator, which has potential applications in high resolution microscopies such as total

internal reflection fluorescence microscopy (TIRFM) and surface plasmon microscopy (SPM) [95]. The TIRFM technique, first developed by Axelrod [7] in 1984, is an important tool for biophysics and quantitative biology. In TIRM, a fluorescently-labeled sample (such as a biological species) is adsorbed onto a functionalized gold film that is predeposited onto a glass slide. The slide is illuminated using waveguided light or a prism to achieve a sufficient incident angle for total reflection at the glass-air interface, creating an evanescent field on the functionalized side of the gold film. Cell binding events, molecular and ionic transport, and other biological events that are confined near the specimen surface and that involve species labeled with fluorescent dyes become observable via dye excitation by the evanescent field, as discussed in Chapter 1.

The excitonic energy transfer device described in Chapter 3 creates an evanescent wave above the metal surface in the form of surface plasmons, pumped by electrically generated molecular excitons in the interior of the organic layers. As demonstrated in Chapter 3, energy can be transfer resonantly from the electrically-pumped excitons to an acceptor molecule on the outside of the metal electrode, provided the molecule is near the surface. Therefore, such a device can function as a direct substitute for the optically illuminated glass slide used in conventional TIRFM. This potentially allows the sensor to be monolithically integrated with other components in lab-on-a-chip systems, achieving high signal-to-noise and fabrication costs comparable to those of gold-coated glass slides while eliminating the need for free-space optical pumping components. Electrical pumping also allows for considerably miniaturized devices and pixilated detector arrays for multiplexed and/or high throughput detection.

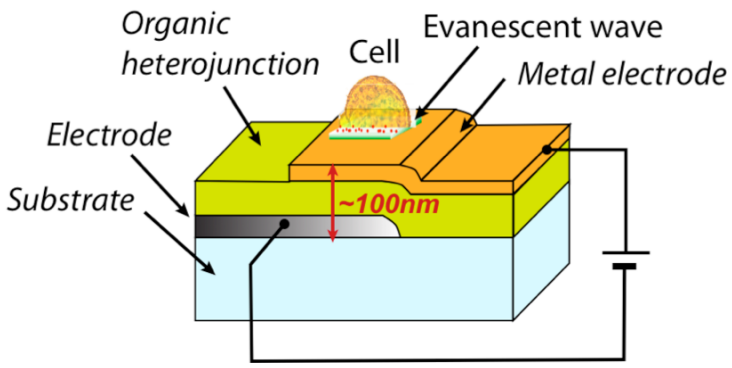

Figure 7.1 Proposed integrated evanescent wave generator, composed of an organic heterostructure sandwiched between two metal electrodes that inject electrons and holes. The recombination of carriers creates molecular excitons, which couple resonantly to surface plasmons in the top electrode, which in turn evanescently couple to the cell adsorbed on top, exciting fluorescencently labeled species in the cell that are adjacent to the metal surface.

7.2.2 High-resolution excitonic probe

The excitonic energy transfer mechanism described in Chapter 3 is useful for exciting dyes in proximity to the electrode (i.e. within several tens of nanometers). It therefore achieves sub-diffraction-limit resolution in the vertical (out-of-plane) direction, but does not have any lateral (in-plane) resolution. To enable sensing with nanoscale precision in 3 dimensions, we can combine the evanescent wave device architecture with the approaches in Chapters 5 and 6 for fabricating organic devices on the tips of scanning probes. Several important applications of the resulting excitonic probe are immediately apparent, such as imaging excitonic and charge carrier transport in nanostructured semiconductor materials, or profiling the 3D distribution of various fluorescently-labeled species in biological samples. Such a probe is visualized in **Fig. 7.2a**; it consists of an electrically pumped organic heterostructure deposited conformally on a sharp probe, similar to the device geometry reported in [110]. In contact mode, the metal cathode of

the probe touches the sample, with the contact region size dictated by the tip radius of curvature, the contact force, and the sample deformation. Plasmon-mediated transfer of the electrically-pumped excitonic energy excites the dyes in the sample, with an interaction strength that depends on the distance from the tip. For regions of the sample far from the contact point, the boundary condition does not support a coupled surface plasmon, and the field is confined to the cathode-organic interface on the interior of the probe, depicted in **Fig. 7.2a** in red. The lateral resolution achievable using this type of probe is therefore expected to be finer than 50 nm, since the extent of the evanescent field that excites the sample is 50 nm or smaller.

A further application of the scanning exciton probe is illustrated in **Fig. 7.2b**; such a probe could be used to profile the cross-section of a bulk heterojunction (BHJ) organic solar cell [77]. As the probe is scanned across the sample, excitons generated inside the probe transfer their energy (via plasmons in the tip) to the material in the sample, followed by exciton diffusion and photocurrent generation in the sample. Correlating the measured photocurrent in the sample with probe position can thus map out the electron donor-acceptor interface of the bulk heterojunction. Such a probe would be valuable for studying exciton dynamics in organic or organic/inorganic hybrid photovoltaic devices.

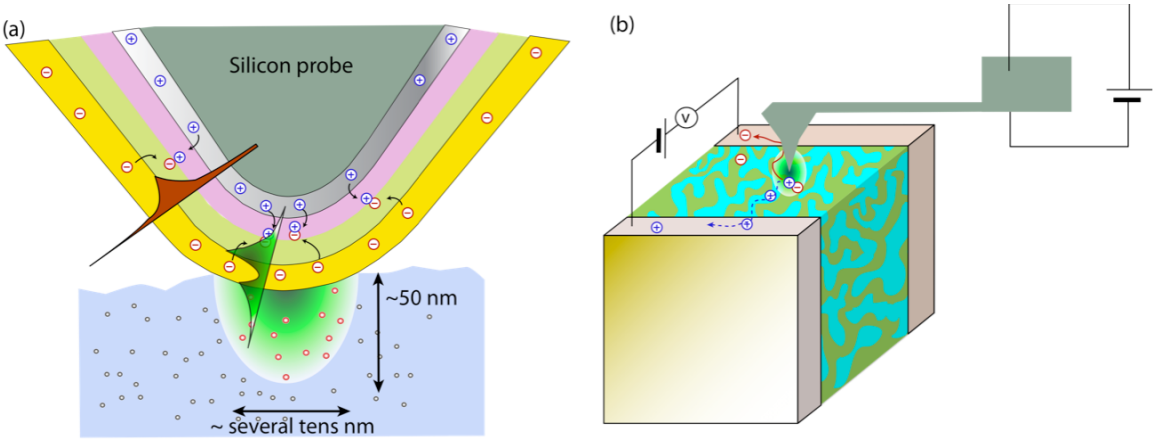

Figure 7.2 (a) An illustration of how an excitonic probe can be used to measure the distribution of fluorescent dyes in a sample. There are three ways to measure the energy transferred from the probe: 1) measure the fluorescent light emission from the sample, 2) measure the current change to the excitonic probe, and 3) measure the photocurrent in the BHJ device. The depth of the evanescent field that excites dyes in the sample is less than 50 nm, suggesting that the lateral resolution can be finer than 50 nm. (b) An illustration of the scanning exciton probe being used to map the distribution of electron donor and acceptor materials in a bulk heterojunction solar cell, where photocurrent is expected to be stronger when the probe excites molecules that are closest to the donor-acceptor interface.

7.2.3 High-resolution scanning fluorescence microscopy

Fluorescence microscopy requires the ability to detect weak fluorescent emission at a given wavelength and reject (or otherwise not detect) strong excitation light at a slightly different wavelength. In Chapter 4 we introduced a method to tune the spectral response of a thin-film organic photodetector by controlling the optical cavity thickness using an optical spacer (MoO_3), and in Chapter 6 we demonstrated high-resolution scanning optical microscopy with a submicrometer-scale organic photodetector fabricated on the tip of a scanning probe. Combining these two techniques, as in **Fig. 7.3a**, could result in a tool for high-resolution scanning fluorescence microscopy (**Fig. 7.3b**). For example, the probe could be tuned using an optical spacer to respond only to green light

(e.g. fluorescent dye emission) and not the blue light used for sample illumination (excitation). The spatial resolution is expected to be comparable to the size of the anode (~ 200 nm), providing a useful tool for imaging fluorescently-labeled biological systems.

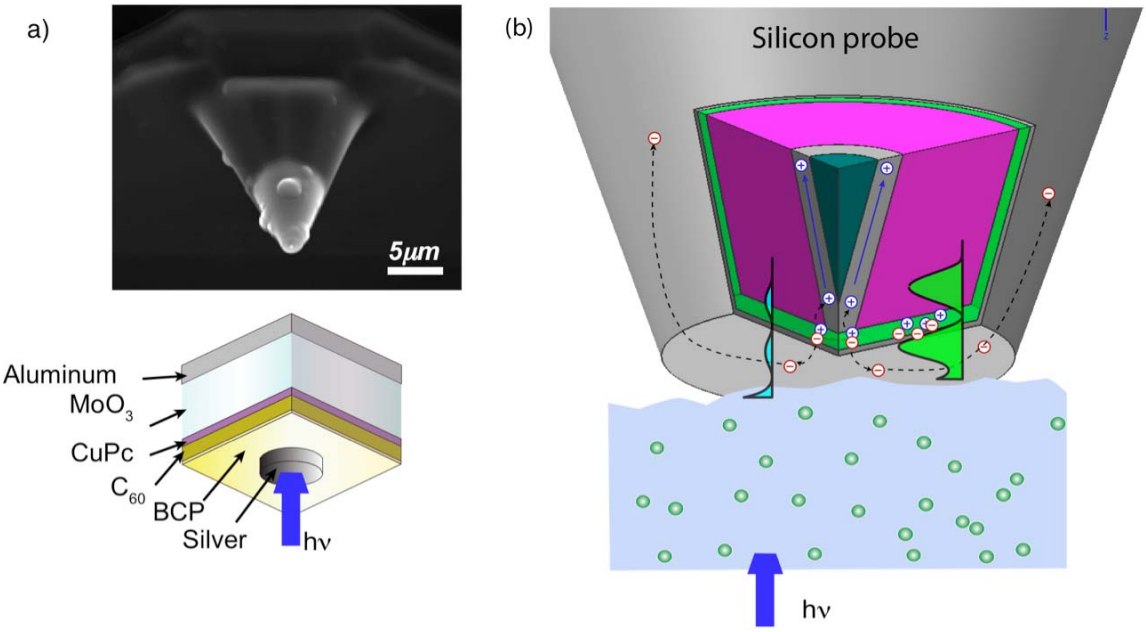

Figure 7.3 (a) An illustration of how a tunable, thin film organic photodetector can be realized in a scanning probe form factor to enable wavelength-selective detection with submicrometer spatial resolution. (b) An illustration of how high-resolution scanning fluorescence microscopy can be performed with such a probe. For a probe that is tuned to respond only to green light, excitation (blue) light does not contribute to photocurrent generation in the active organic materials of the probe. However, green emission from the fluorescent dye resonantly couples to the microcavity inside the organic layers, and does generate photocurrent. The spatial resolution is expected to be comparable to the size of the anode (~ 200 nm) or even finer, as discussed in Chapter 6.

APPENDIX A

Formulation of Dyadic Green's function

Here we calculate the electric field produced by a source in a multilayer stack, using a dyadic Green's function approach based on Li and Celebi's works [20,51]. **Figure A.1** shows the multilayer structure used for the calculation. The dipole source is placed in layer *s* at *z* = 0, with layers 1 and N assumed to be semi-infinite.

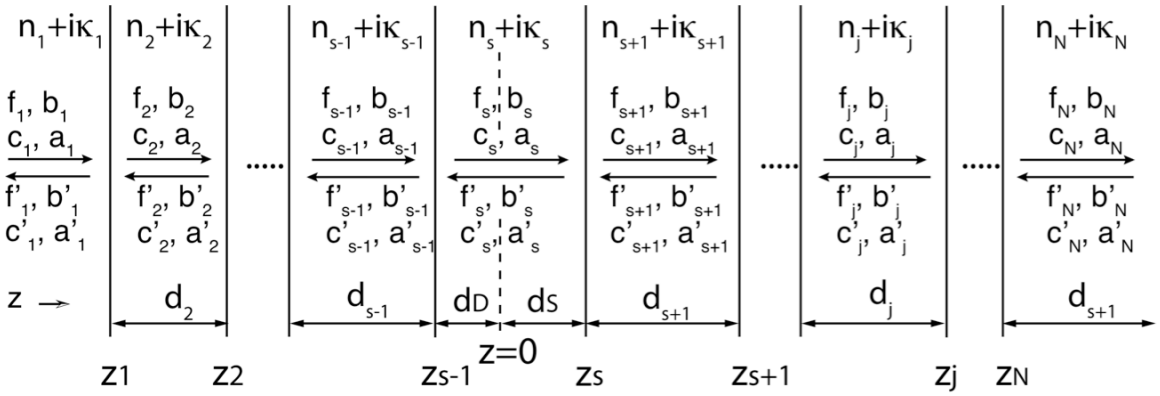

Figure A.1 Multilayer structure in which dyadic Green's function method is implemented.

Each layer is assumed to be isotropic, with property variables changing only in the cross-plane direction (*z*). Each layer is defined by a complex index of refraction ($n+i\kappa$) and thickness *d*. The electric field caused by an oscillating current source (electrical dipole) *J(R')* is given by

$$E(R) = i\omega\mu_0 \int G(R \mid R') \cdot J(R') d^3R' \tag{A.1}$$

where μ_0 is the magnetic permeability and $G(R|R')$ is the dyadic Green's function. The dyadic Green's function can be written in terms of eigenfunctions M and N in cylindrical coordinates for the multilayer system:

$$M_{\substack{e\\o}n\kappa}(h) = e^{ihz}\left[\mp\frac{nJ_n(\kappa r)}{r}\begin{matrix}\sin\\\cos\end{matrix} n\phi\hat{r} - \frac{\partial J_n(\kappa r)}{\partial r}\begin{matrix}\cos\\\sin\end{matrix} n\phi\hat{\phi}\right] \tag{A.2}$$

$$N_{\substack{e\\o}n\kappa}(h) = \frac{e^{ihz}}{k_j}\left[ih\frac{\partial J_n(\kappa r)}{\partial r}\begin{matrix}\cos\\\sin\end{matrix} n\phi\hat{r} \mp inh\frac{J_n(\kappa r)}{r}\begin{matrix}\sin\\\cos\end{matrix} n\phi\hat{\phi} + \kappa^2 J_n(\kappa r)\begin{matrix}\cos\\\sin\end{matrix} n\phi\hat{z}\right] \tag{A.3}$$

where j is the layer index, κ and h are the parallel and perpendicular components of the field wavevector, and J_n is an nth-order Bessel function of the first type. Even and odd eigenfunctions are designated by subscripts e and o. Using these eigenfunctions, the Green's function can be expressed as:

$$G_0(R\,|\,R') = \frac{i}{4\pi}\int_0^\infty d\kappa \sum_{\substack{n=0\\t=e,o}}^{\infty}\frac{2-\delta_{n0}}{\kappa h_s}\begin{cases}\left[M_{tn\kappa}(h_s)M'_{tnk}(-h_s) + N_{tn\kappa}(h_s)N'_{tnk}(-h_s)\right] & z \geq 0\\ \left[M_{tn\kappa}(-h_s)M'_{tnk}(h_s) + N_{tn\kappa}(-h_s)N'_{tnk}(h_s)\right] & z \leq 0\end{cases} \tag{A.4}$$

$$G_j(R\,|\,R') = \frac{i}{4\pi}\int_0^\infty d\kappa \sum_{\substack{n=0\\t=e,o}}^{\infty}\frac{2-\delta_{n0}}{\kappa h_s}\begin{bmatrix} c_j M_{tn\kappa}(-h_s)M'_{tnk}(h_s) + f_j N_{tn\kappa}(-h_s)N'_{tnk}(h_s)\\ +c'_j M_{tn\kappa}(h_s)M'_{tnk}(h_s) + f'_j N_{tn\kappa}(h_s)N'_{tnk}(h_s)\\ +a_j M_{tn\kappa}(-h_s)M'_{tnk}(-h_s) + b_j N_{tn\kappa}(-h_s)N'_{tnk}(-h_s)\\ +a'_j M_{tn\kappa}(h_s)M'_{tnk}(-h_s) + b'_j N_{tn\kappa}(h_s)N'_{tnk}(-h_s)\end{bmatrix} \tag{A.5}$$

where the prime denotes the sources, s denotes the source layer, j denotes the j^{th} layer, and δ is the Dirac delta function. The coefficients c, c', f, f', a, a', b, and b' in each layer can be determined by applying boundary conditions (equation 2.10 and 2.11) at each interface. For a source layer s, G_0 is added to G_j in order to take account of source effects :

$$\hat{z}\times\left\{G_j(R\,|\,R')+\delta_j^s G_0(R\,|\,R')\right\}=\hat{z}\times\left\{G_{j+1}(R\,|\,R')+\delta_{j+1}^s G_0(R\,|\,R')\right\} \tag{A.6}$$

$$\hat{z}\times\nabla\times\left\{G_j(R\,|\,R')+\delta_j^s G_0(R\,|\,R')\right\}=\hat{z}\times\nabla\times\hat{z}\times\left\{G_{j+1}(R\,|\,R')+\delta_{j+1}^s G_0(R\,|\,R')\right\} \tag{A.7}$$

The boundary conditions of A.6 and A.7 at $z = z_j$ give

$$c_j e^{-ih_j z}+c_j^{'}e^{ih_j z}=\left(c_{j+1}+\delta_{j+1}^s\right)e^{-ih_{j+1}z}+c_{j+1}^{'}e^{ih_{j+1}z} \tag{A.8}$$

$$-f_j e^{-ih_j z}\frac{h_j}{k_j}+f_j^{'}e^{ih_j z}\frac{h_j}{k_j}=-\left(f_{j+1}+\delta_{j+1}^s\right)e^{-ih_{j+1}z}\frac{h_{j+1}}{k_{j+1}}+f_{j+1}^{'}e^{ih_{j+1}z}\frac{h_{j+1}}{k_{j+1}} \tag{A.9}$$

$$a_j e^{-ih_j z}+\left(a_j^{'}+\delta_j^s\right)e^{ih_j z}=a_{j+1}e^{-ih_{j+1}z}+a_{j+1}^{'}e^{ih_{j+1}z} \tag{A.10}$$

$$-b_j e^{-ih_j z}\frac{h_j}{k_j}+\left(b_j^{'}+\delta_j^s\right)e^{ih_j z}\frac{h_j}{k_j}=-b_{j+1}e^{-ih_{j+1}z}\frac{h_{j+1}}{k_{j+1}}+b_{j+1}^{'}e^{ih_{j+1}z}\frac{h_{j+1}}{k_{j+1}} \tag{A.11}$$

$$-h_j c_j e^{-ih_j z}+h_j c_j^{'}e^{ih_j z}=-h_{j+1}\left(c_{j+1}+\delta_{j+1}^s\right)e^{-ih_{j+1}z}+h_{j+1}c_{j+1}^{'}e^{ih_{j+1}z} \tag{A.12}$$

$$k_j f_j e^{-ih_j z}+k_j f_j^{'}e^{ih_j z}=k_{j+1}\left(f_{j+1}+\delta_{j+1}^s\right)e^{-ih_{j+1}z}+k_{j+1}f_{j+1}^{'}e^{ih_{j+1}z} \tag{A.13}$$

$$-h_j a_j e^{-ih_j z}+h_j\left(a_j^{'}+\delta_j^s\right)e^{ih_j z}=-h_{j+1}a_{j+1}e^{-ih_{j+1}z}+h_{j+1}a_{j+1}^{'}e^{ih_{j+1}z} \tag{A.14}$$

$$k_j b_j e^{-ih_j z}+k_j\left(b_j^{'}+\delta_j^s\right)e^{ih_j z}=k_{j+1}b_{j+1}e^{-ih_{j+1}z}+k_{j+1}b_{j+1}^{'}e^{ih_{j+1}z} \tag{A.15}$$

We can rearrange the equations (A.8-A.15) in matrix form:

$$\begin{bmatrix} c_{j+1}+\delta_{j+1}^s & a_{j+1} \\ c_{j+1}^{'} & a_{j+1}^{'} \end{bmatrix}=\overline{T}_{ca}^{\,j}\cdot\begin{bmatrix} c_j & a_j \\ c_j^{'} & a_j^{'}+\delta_j^s \end{bmatrix} \tag{A.16}$$

$$\begin{bmatrix} f_{j+1}+\delta_{j+1}^s & b_{j+1} \\ f_{j+1}^{'} & b_{j+1}^{'} \end{bmatrix}=\overline{T}_{fb}^{\,j}\cdot\begin{bmatrix} f_j & b_j \\ f_j^{'} & b_j^{'}+\delta_j^s \end{bmatrix} \tag{A.17}$$

where

$$\overline{T}_{ca}^{\,j} = \begin{bmatrix} \dfrac{h_{j+1}+h_j}{2h_{j+1}} e^{i(h_{j+1}-h_j)z} & \dfrac{h_{j+1}-h_j}{2h_{j+1}} e^{i(h_{j+1}+h_j)z} \\ \dfrac{h_{j+1}-h_j}{2h_{j+1}} e^{-i(h_{j+1}+h_j)z} & \dfrac{h_{j+1}+h_j}{2h_{j+1}} e^{-i(h_{j+1}-h_j)z} \end{bmatrix} \tag{A.18}$$

$$\overline{T}_{fb}^{\,j} = \begin{bmatrix} \dfrac{k_{j+1}}{2k_{j+1}}\left(1+\dfrac{k_{j+1}^2}{k_j^2}\dfrac{h_j}{h_{j+1}}\right) e^{i(h_{j+1}-h_j)z} & \dfrac{k_{j+1}}{2k_{j+1}}\left(1-\dfrac{k_{j+1}^2}{k_j^2}\dfrac{h_j}{h_{j+1}}\right) e^{i(h_{j+1}+h_j)z} \\ \dfrac{k_{j+1}}{2k_{j+1}}\left(1-\dfrac{k_{j+1}^2}{k_j^2}\dfrac{h_j}{h_{j+1}}\right) e^{-i(h_{j+1}+h_j)z} & \dfrac{k_{j+1}}{2k_{j+1}}\left(1+\dfrac{k_{j+1}^2}{k_j^2}\dfrac{h_j}{h_{j+1}}\right) e^{-i(h_{j+1}-h_j)z} \end{bmatrix} \tag{A.19}$$

Defining $\overline{\overline{CA}} = \begin{bmatrix} c_j & a_j \\ c_j^{'} & a_j^{'} \end{bmatrix}$ to make the formula simpler, and assuming no incoming waves

for the first and last cells, we have

$$\overline{\overline{CA}}^{1} = \begin{bmatrix} c_1 & a_1 \\ 0 & 0 \end{bmatrix} \text{ and } \overline{\overline{CA}}^{N} = \begin{bmatrix} 0 & 0 \\ c_N^{'} & a_N^{'} \end{bmatrix} \tag{A.20}$$

The $(s\text{-}1)^{th}$ cell can be expressed in terms of the first cell:

$$\overline{\overline{CA}}^{s-1} = \overline{T}_{ca}^{s-2} \cdot \overline{T}_{ca}^{s-3} \cdot \overline{T}_{ca}^{s-4} \cdots \overline{T}_{ca}^{1} \cdot \overline{\overline{CA}}^{1} \tag{A.21}$$

with the source cell having the following two forms:

$$\begin{bmatrix} c_s+1 & a_s \\ c_s^{'} & a_s^{'} \end{bmatrix} = \overline{T}_{ca}^{s-1} \begin{bmatrix} c_{s-1} & a_{s-1} \\ c_{s-1}^{'} & a_{s-1}^{'} \end{bmatrix} = \overline{T}_{ca}^{s-1} \overline{\overline{CA}}^{s-1} \tag{A.22}$$

$$\overline{\overline{CA}}^{s+1} = \begin{bmatrix} c_{s+1} & a_{s+1} \\ c_{s+1}^{'} & a_{s+1}^{'} \end{bmatrix} = \overline{T}_{ca}^{s} \begin{bmatrix} c_s & a_s \\ c_s^{'} & a_s^{'}+1 \end{bmatrix} \tag{A.23}$$

Equating A.22 and A.23,

$$\begin{bmatrix} c_s & a_s \\ c_s^{'} & a_s^{'} \end{bmatrix} = \overline{T}_{ca}^{s-1} \overline{\overline{CA}}^{s-1} - \begin{bmatrix} 1 & 0 \\ 0 & 0 \end{bmatrix} = \left[\overline{T}_{ca}^{s}\right]^{-1} \overline{\overline{CA}}^{s+1} - \begin{bmatrix} 0 & 0 \\ 0 & 1 \end{bmatrix} \tag{A.24}$$

$$\overline{\overline{CA}}^{s+1} = \overline{\overline{T}}_{ca}^{s}\left(\overline{\overline{T}}_{ca}^{s-1}\overline{\overline{CA}}^{s-1} + \begin{bmatrix}0 & 0\\ 0 & 1\end{bmatrix} - \begin{bmatrix}1 & 0\\ 0 & 0\end{bmatrix}\right) \tag{A.25}$$

$$\begin{aligned}\overline{\overline{CA}}^{N} &= \overline{\overline{T}}_{ca}^{N-1}\overline{\overline{T}}_{ca}^{N-2}\cdots\overline{\overline{T}}_{ca}^{s+1}\overline{\overline{CA}}^{s+1}\\ &= \overline{\overline{T}}_{ca}^{N-1}\overline{\overline{T}}_{ca}^{N-2}\cdots\overline{\overline{T}}_{ca}^{s+1}\left(\overline{\overline{T}}_{ca}^{s}\overline{\overline{T}}_{ca}^{s-1} + \begin{bmatrix}-1 & 0\\ 0 & 1\end{bmatrix}\right)\\ &= \overline{\overline{T}}_{ca}^{N-1}\overline{\overline{T}}_{ca}^{N-2}\cdots\overline{\overline{T}}_{ca}^{s+1}\overline{\overline{T}}_{ca}^{s}\left(\overline{\overline{T}}_{ca}^{s-1}\overline{\overline{T}}_{ca}^{s-2}\cdots\overline{\overline{T}}_{ca}^{1}\overline{\overline{CA}}^{1} + \begin{bmatrix}-1 & 0\\ 0 & 1\end{bmatrix}\right)\\ &= \overline{\overline{\Gamma}}_{ca}^{(1)}\overline{\overline{CA}}^{1} + \overline{\overline{\Gamma}}_{ca}^{(s)}\begin{bmatrix}-1 & 0\\ 0 & 1\end{bmatrix}\end{aligned} \tag{A.26}$$

where

$$\overline{\overline{\Gamma}}_{ca}^{(k)} = T_{ca}^{N-1}\overline{\overline{T}}_{ca}^{N-2}\cdots\overline{\overline{T}}_{ca}^{k} \tag{A.27}$$

This finally yields

$$c_1 = \frac{\overline{\overline{\Gamma}}_{ca}^{(s)}(1,1)}{\overline{\overline{\Gamma}}_{ca}^{(1)}(1,1)} \tag{A.28}$$

$$a_1 = -\frac{\overline{\overline{\Gamma}}_{ca}^{(s)}(1,2)}{\overline{\overline{\Gamma}}_{ca}^{(1)}(1,1)} \tag{A.29}$$

$$c_N^{'} = -\frac{\overline{\overline{\Gamma}}_{ca}^{(s)}(1,1)}{\overline{\overline{\Gamma}}_{ca}^{(1)}(1,1)}\overline{\overline{\Gamma}}_{ca}^{(1)}(2,1) - \overline{\overline{\Gamma}}_{ca}^{(s)}(2,1) \tag{A.30}$$

$$a_N^{'} = -\frac{\overline{\overline{\Gamma}}_{ca}^{(s)}(1,2)}{\overline{\overline{\Gamma}}_{ca}^{(1)}(1,1)}\overline{\overline{\Gamma}}_{ca}^{(1)}(2,1) + \overline{\overline{\Gamma}}_{ca}^{(s)}(2,2) \tag{A.31}$$

with the coefficients for the source determined as

$$\begin{bmatrix}c_s + 1 & a_s\\ c_s^{'} & a_s^{'}\end{bmatrix} = \overline{\overline{T}}_{ca}^{s-1}\overline{\overline{T}}_{ca}^{s-2}\cdots\overline{\overline{T}}_{ca}^{1}\begin{bmatrix}c_1 & a_1\\ 0 & 0\end{bmatrix} \tag{A.32}$$

and A.21 used for the coefficients of the other layers. Coefficients *b* and *f* can be found in a similar way.

We calculate the electric field based on A.1 using $\boldsymbol{J(R')} = -i\omega\boldsymbol{p_0}\delta\boldsymbol{(R')}$ for a dipole

moment p_0, and equating M_z, $J^{\perp}_{r,\phi}$, and $J^{//}_z$ to zero. When the Bessel function index $n=0$, $N'_z=k_2/k_x$, and when $n=1$, $M'_r=-M'_\phi=\kappa/2$, $N'_r=-N'_\phi=\kappa h_s/2k_s$. For both cases, other components of the primed eigenfunctions are zero. The components of the electric field for perpendicular and parallel dipoles are then given as

$$E^{\perp}_{j,r}=\frac{\omega^2 p_0}{4\pi}\int_0^{\infty} d\kappa \frac{\kappa h_j}{k_s k_j h_s}\frac{\partial J_0(\kappa r)}{\partial r}\left(b_j e^{-ih_j z}+f_j e^{-ih_j z}-b'_j e^{ih_j z}-f'_j e^{ih_j z}\right) \tag{A.33}$$

$$E^{\perp}_{j,z}=\frac{i\omega^2 p_0}{4\pi}\int_0^{\infty} d\kappa \frac{\kappa^3}{k_s k_j h_s}J_0(\kappa r)\left(b_j e^{-ih_j z}+f_j e^{-ih_j z}+b'_j e^{ih_j z}+f'_j e^{ih_j z}\right) \tag{A.34}$$

$$E^{//}_{j,r}=\frac{i\omega^2 p_0}{4\pi}\int_0^{\infty} d\kappa \begin{bmatrix} \frac{1}{h_s}\frac{J_1(\kappa r)}{r}(\cos\phi-\sin\phi)\left(c_j e^{-ih_j z}+a_j e^{-ih_j z}+c'_j e^{ih_j z}+a'_j e^{ih_j z}\right) \\ +\frac{h_j}{k_j k_s}\frac{\partial J_1(\kappa r)}{\partial r}(\cos\phi+\sin\phi)\left(f_j e^{-ih_j z}-b_j e^{-ih_j z}-f'_j e^{ih_j z}+b'_j e^{ih_j z}\right) \end{bmatrix} \tag{A.35}$$

$$E^{//}_{j,\phi}=\frac{i\omega^2 p_0}{4\pi}\int_0^{\infty} d\kappa \begin{bmatrix} -\frac{1}{h_s}\frac{\partial J_1(\kappa r)}{\partial r}(\cos\phi+\sin\phi)\left(c_j e^{-ih_j z}+a_j e^{-ih_j z}+c'_j e^{ih_j z}+a'_j e^{ih_j z}\right) \\ +\frac{h_j}{k_j k_s}\frac{J_1(\kappa r)}{r}(\cos\phi-\sin\phi)\left(f_j e^{-ih_j z}-b_j e^{-ih_j z}-f'_j e^{ih_j z}+b'_j e^{ih_j z}\right) \end{bmatrix} \tag{A.36}$$

$$E^{//}_{j,z}=\frac{-\omega^2 p_0}{4\pi}\int_0^{\infty} d\kappa \frac{\kappa^2}{k_j k_s}J_1(\kappa r)(\cos\phi+\sin\phi)\left(f_j e^{-ih_j z}-b_j e^{-ih_j z}-f'_j e^{ih_j z}+b'_j e^{ih_j z}\right) \tag{A.37}$$

By substituting the calculated electric fields components at $z=0$ in $b=\frac{e^2 k_s^3}{6\pi m\omega\varepsilon}\left[1+\frac{3q\varepsilon}{2p_0 k_s^3}\mathrm{Im}(E_0)\right]$, we can express the decay rate as a function of the coefficients as

$$\frac{b_{\perp}}{b_0}=1-q+q\left\{1+\frac{3}{2}\mathrm{Re}\left[\int_0^{\infty} d\kappa \frac{\kappa^3}{h_s k_s^2}\left(b_s+f_s+b'_s+f'_s\right)\right]\right\} \tag{A.38}$$

$$\frac{b_{//}}{b_0} = 1 - q + q\left\{1 + \frac{3}{4}\mathrm{Re}\left[\int_0^\infty d\kappa \frac{\kappa}{h_s}\left(c_s + a_s + c_s^{'} + a_s^{'} + \frac{h_s^2}{k_s^2}\left(f_s - b_s - f_s^{'} + b_s^{'}\right)\right)\right]\right\} \quad \text{(A.39)}$$

To calculate the energy flow in the device, we use the divergence of the Poynting vector:

$$\int \nabla \cdot S dV = \oiint S \cdot dA \approx \int S_z dA \quad \text{(A.40)}$$

$$S_z = \frac{i}{2\mu_0 \omega}\left[E_r\left(\frac{\partial E_r}{\partial z} - \frac{\partial E_z}{\partial r}\right)^* + E_\phi\left(\frac{\partial E_\phi}{\partial z} - \frac{1}{r}\frac{\partial E_z}{\partial \phi}\right)^*\right] \quad \text{(A.41)}$$

The Poynting vector S_z can be expressed using the E-field components in cylindrical coordinates. With some algebra, we obtain a final form for the power flow rate for each perpendicular and parallel dipole after normalizing with respect to the total energy of the free dipole (b_0), given by $mp_0^2\omega^2/2e^2$.

$$\mathrm{Re}\left(\int S_{z,j}^{\perp\,*} dA\right) = \frac{3q}{4}\mathrm{Re}\left[\int_0^\infty du \frac{u^3 h_j k_j^*}{|h_s|^2 k_s^2 k_j}\left(b_s^{'}e^{ih_j z} + f_s^{'}e^{ih_j z} - b_s e^{-ih_j z} - f_s e^{-ih_j z}\right) \cdot \left(b_s^{'}e^{ih_j z} + f_s^{'}e^{ih_j z} + b_s e^{-ih_j z} + f_s e^{-ih_j z}\right)^*\right] \quad \text{(A.42)}$$

$$\mathrm{Re}\left(\int S_{z,j}^{//\,*} dA\right) = \frac{3q}{8}\mathrm{Re}\left[\int_0^\infty du \left(\begin{array}{l} \frac{uh_j^*}{|h_s|^2}\left(c_s^{'}e^{ih_j z} + a_s^{'}e^{ih_j z} + c_s e^{-ih_j z} + a_s e^{-ih_j z}\right) \\ \quad \cdot \left(c_s^{'}e^{ih_j z} + a_s^{'}e^{ih_j z} - c_s e^{-ih_j z} - a_s e^{-ih_j z}\right)^* \\ + \frac{uh_j k_j^*}{k_s^2 k_j}\left(b_s^{'}e^{ih_j z} - f_s^{'}e^{ih_j z} - b_s e^{-ih_j z} + f_s e^{-ih_j z}\right) \\ \quad \cdot \left(b_s^{'}e^{ih_j z} - f_s^{'}e^{ih_j z} + b_s e^{-ih_j z} - f_s e^{-ih_j z}\right)^* \end{array}\right] \quad \text{(A.43)}$$

where u ($=k_x/k_0$) is a normalized in-plane wave vector by k_0. Equations A.42 and A.43 can then be plotted with respect to the in-plane wave vector and the position, yielding the

energy flux at each position within the device. We present energy flux diagrams for perpendicular and parallel oriented dipoles in **Fig. A.2**.

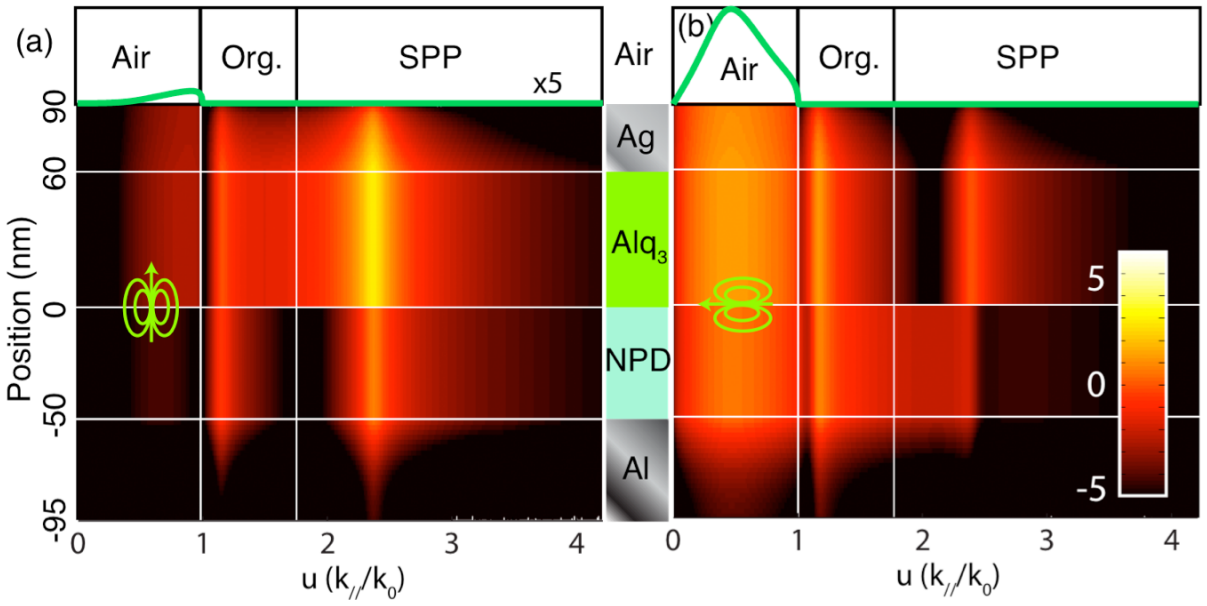

Figure A.2 Calculated energy flux diagram for a) perpendicular and b) parallel oriented dipoles with respect to normalized wave vector and layer position.

APPENDIX B

Boundary conditions for organic-organic heterojunction in electrical transport model

Because of differences in energy level and material properties of the device materials, the hole and electron densities in an organic device are discontinuous at organic-organic interfaces. For our finite-difference calculations, we define the cell domains as shown in **Fig. B.1**. The carrier densities (n, p) are defined at the center point (node) of the cell, and the current densities (J_n, J_p), electric field (E) and mobility (μ) are defined at the boundaries of the cell. The organic heterojunction is placed between the M_x and M_{x+1} nodes, adjacent to the boundary between the M_x and M_{x+1} cells. The band diagram of the organic heterojunction is drawn in **Fig. B.2**.

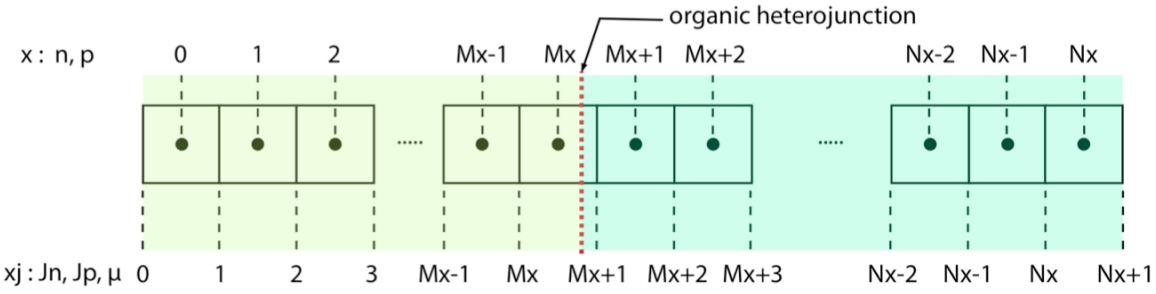

Figure B.1 Cells for the numerical calculation. Carrier densities are defined at the cell centers (nodes), and current densities and electric field are defined at the cell boundaries.

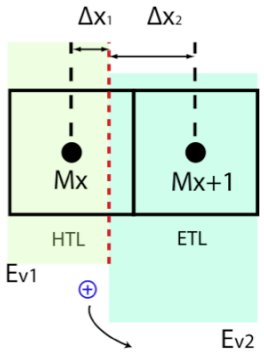

Figure B.2 Band diagram of the hole transport layer (HTL) and electron transport layer (ETL).

Thermionic emission over the heterobarrier (and carrier backflow in the opposite direction) are used in conjunction with the drift-diffusion equation to calculate carrier densities on either side of the organic heterojunction. We assume that the thermionic emission and backflow processes are sufficiently fast that quasi-thermal equilibrium is valid, and write the hole current density at the heterojunction as:

$$J_p = qv_1 p\left(x_0^-\right) e^{(E_{V1}-E_{V2})/kT} - qv_2 p\left(x_0^+\right) \tag{B.1}$$

where q is the elementary charge, k is the Boltzmann constant, E_{v1} and E_{v2} are HOMO energy levels for the HTL and ETL, $p(x^-)$ and $p(x^+)$ are the hole densities at the organic junction on the HTL and ETL sides respectively, and T is the absolute temperature. The effective carrier velocity v_i can be written as χ/n_{oi}, for i=1,2, where n_{oi} is intrinsic carrier density and χ is the kinetic coefficient for thermionic emission, taken as AT^2 with Richardson coefficient A [24]. In thermal equilibrium, the carrier density ratio at the interface is given by

$$\frac{p\left(x_0^-\right)}{p\left(x_0^+\right)} = \frac{n_{01}}{n_{02}} e^{-(E_{V1}-E_{V2})/kT} = \frac{v_2}{v_1} e^{-(E_{V1}-E_{V2})/kT} \tag{B.2}$$

The drift-diffusion equation for holes, expressed as

$$\frac{\partial p}{\partial x} = \frac{qE}{kT} p - \frac{J_p}{kT\mu_p} \tag{B.3}$$

can be integrated from x_M to the interface, to yield

$$p_0^- = p_M e^{\frac{qE_{1,M+1}}{kT}\Delta x_1} + \frac{J_{p,M}}{q\mu_{1p}E_{1,M+1}}\left(1 - e^{\frac{qE_{1,M+1}}{kT}\Delta x_1}\right) \tag{B.4}$$

Similarly, integrating from the interface to x_{M+1} gives

$$p_0^+ = p_{M+1} e^{-\frac{qE_{2,M+1}}{kT}\Delta x_2} + \frac{J_{p,M}}{q\mu_{2p}E_{2,M+1}}\left(1 - e^{-\frac{qE_{2,M+1}}{kT}\Delta x_2}\right) \tag{B.5}$$

By inserting equations B.4 and B.5 into B.1, we can write $J_{p,\,Mx+1}$ as

$$J_{p,M_x+1} = q\mu_{1p}E_{1,M_x+1}\frac{p_{M_x}e^{(qE_1/kT)\Delta x_1}e^{\varphi_b/kT} - p_{M_x+1}\dfrac{n_{01}}{n_{02}}e^{-(qE_1/kT)\Delta x_2}}{\dfrac{n_{01}}{\chi}\mu_{1p}E_1 - \left(1 - e^{(qE_1/kT)\Delta x_1}\right)e^{-\Delta E/kT} + \dfrac{E_1\mu_{1p}n_{01}}{E_2\mu_{2p}n_{02}}\left(1 - e^{-(qE_1/kT)\Delta x_1}\right)} \tag{B.6}$$

The analogous equation for electron current density can be found in a similar way:

$$J_{n,M_x+1} = q\mu_{1n}E_{1,M_x+1}\frac{n_{M_x+1}\dfrac{n_{01}}{n_{02}}e^{(qE_1/kT)\Delta x_2}e^{\varphi_b/kT} - n_{M_x}e^{-(qE_1/kT)\Delta x_1}}{\dfrac{n_{01}}{\chi}\mu_{1p}E_1 - \dfrac{E_1\mu_{1p}n_{01}}{E_2\mu_{2p}n_{02}}\left(1 - e^{(qE_1/kT)\Delta x_2}\right)e^{-\Delta E/kT} + \left(1 - e^{-(qE_1/kT)\Delta x_1}\right)} \tag{B.7}$$

We use equations B.6 and B.7 as boundary conditions for hole and electron current density calculations at organic-organic interfaces.

APPENDIX C

Measurement of external quantum efficiency of photovoltaic devices

To investigate the spectral response of organic photovoltaic device, we built an experimental setup for external quantum efficiency. The external quantum efficiency of a photovoltaic device is defined as the total number of collected electrons (N_e) divided by the total number of incident photons (N_{ph}) at a given wavelength:

$$\eta_{EQE}(\lambda) = \frac{N_e(\lambda)}{N_{ph}(\lambda)} \tag{C.1}$$

The number of collected electrons can be calculated from the measured photo-current, and the number of incident photons can be calculated from the measured light power. The system we use to measure device current is illustrated in **Fig. C.1**. A monochromic light source is realized using a monochromator (Cornerstone 74004) and halogen lamp. The full width half maximum is adjusted to be less than 5 nm by controlling the slit size of the monochromator. To enhance the signal-to-noise ratio of the measured photocurrent, we use a mechanical chopper and lock-in amplifier. The chopper modulates the incident light at a frequency of 89 Hz, the transimpedance amplifier (Femto DLPCA-200) amplifies the photocurrent and converts it to a voltage signal, and the lock-in amplifier measures the component of the photocurrent signal at 89 Hz. A computer running Labview is used to automatically sweep the monochromator over a

range of wavelengths and detect the resulting range of voltage signals produced by the lock-in amplifier.

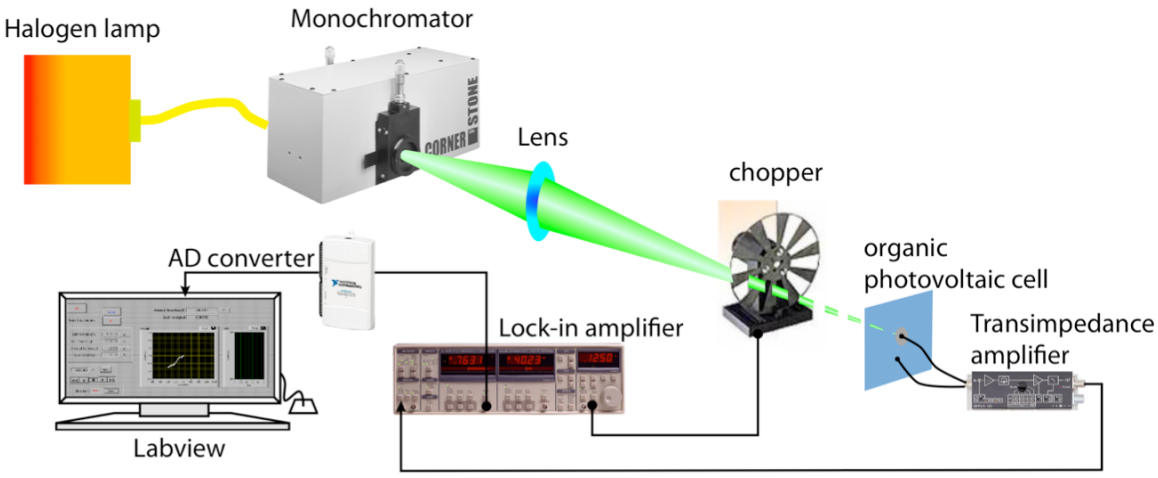

Figure C.1 Experimental setup used to measure the external quantum efficiency of photovoltaic devices.

From this measurement, the number of collected electrons for incident light at a given wavelength ($N_e(\lambda)$) can be calculated by

$$N_e(\lambda) = \frac{I(\lambda)}{q} = \frac{V(\lambda)}{q}\frac{M_{D,LA}}{M_{TA}} \tag{C.2}$$

where q is the elementary charge (1.602×10^{-19} Coulombs), I is the device photocurrent, V is the measured voltage, and M_{TA} and $M_{D,LA}$ are the amplification factors of the transimpedance amplifier and lock-in amplifier. The incident power to the photovoltaic device is separately measured using a reference silicon photodetector (Newport 818SL) and power meter in conjunction with a chopper and lock-in amplifier. From this measurement, we can calculate the number of incident photons at a given wavelength ($N_{ph}(\lambda)$):

$$N_{ph}(\lambda) = I_{ph}(\lambda)\frac{\lambda}{hc} = \frac{P_{ph}(\lambda)}{A_D R(\lambda)}\frac{\lambda}{hc} = \frac{V_{ph}(\lambda)L_{PM}M_{PM,LA}}{A_D R(\lambda)}\frac{\lambda}{hc} \quad \text{(C.3)}$$

where $I_{ph}(\lambda)$ is the intensity of incoming light at wavelength λ, h is Planck's constant, c is the speed of light, P_{ph} is the light power, A_D is the illuminated area on the photodetector, R is the responsivity of detector, $M_{PM,LA}$ is the amplification of lock-in amplifier, and L_{PM} is the set value for the range of power meter. Using equations C.3 and C.4, we have the external quantum efficiency:

$$\eta_{EQE}(\lambda) = \frac{N_e(\lambda)}{N_{ph}(\lambda)} = \frac{hc}{q\lambda}\frac{V(\lambda)}{V_{ph}(\lambda)}\frac{M_{D,LA}}{M_{PM,LA}}\frac{A_D R(\lambda)}{M_{TA}L_{PM}} \quad \text{(C.4)}$$

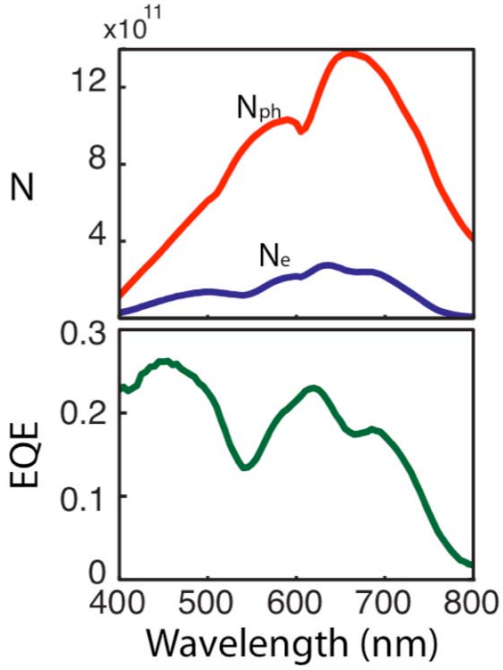

Figure C.2 Measured $N_e(\lambda)$ and $N_{ph}(\lambda)$ for a prototypical device, and calculated external quantum efficiency.

In **Fig. C.2**, we plot the measured $N_e(\lambda)$ and $N_{ph}(\lambda)$ for a device consisting of ITO / CuPc (20 nm) / C_{60} (40 nm) / BCP (7 nm) / Ag (40 nm). The obtained external

quantum efficiency is also presented in **Fig. C.2**, clearly showing the absorption spectra of CuPc and C_{60}.

Appendix D

Chemical vapor deposition of parylene

Parylene is a useful material not only for electrical insulation (due to its high electrical resistivity), but also for chemical passivation (due to its very limited reactivity). Chemical vapor deposition of parylene, shown in **Fig. D.1**, can yield coatings that are conformal, uniform in thickness, and pinhole free. [23] The process is solvent-free and is composed of three steps: 1) A parylene dimer is sublimated to a vapor, 2) Further heating pyrolyzes the material to form monomers, and 3) Monomers are deposited and polymerize on the substrate, which is maintained at room temperature.

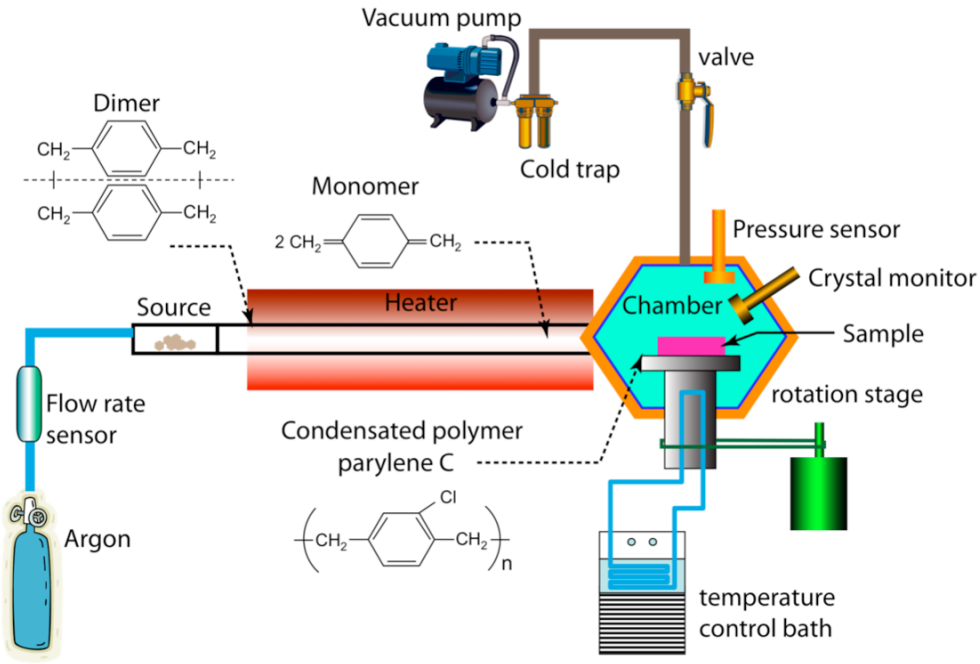

Figure D.1 Chemical vapor deposition system for parylene (Lahann lab, University of Michigan).

The system is composed of an argon source, glass tube, heater, deposition chamber, temperature controller, and vacuum pump. The glass tube and chamber are maintained at a pressure of 0.12 Torr, and the flow rate of argon is adjusted to several liters per second, discharging residual gas through a cold trap. The heater is controlled to maintain 650 ºC, the temperature for parylene pyrolysis. The sample plate continuously rotates for uniform deposition, and water circulation inside the sample plate cools the sample to room temperature (15 ºC) for monomer vapor condensation. For our depositions, we changed the lateral position of the source boat to tune the deposition rate to approximately 1-2 Å/s, and monitored the deposited thickness using the quartz crystal.

A layer of parylene deposited on the tip of an atomic force microscopy cantilever is shown in **Fig. D.2**. Although the film thickness is less than 1µm, the material is deposited conformally and uniformly on the surface, without any pinholes.

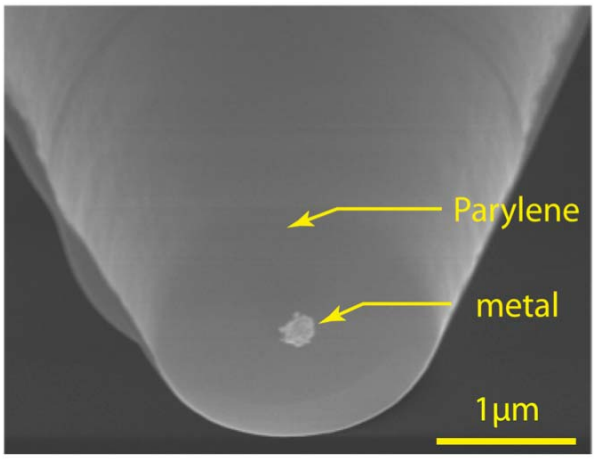

Figure D.2 Parylene layer deposited conformally on the tip of an AFM cantilever. The tip has afterwards been milled with a focused ion beam, demonstrating the uniform parylene layer thickness.

REFERENCES

[1] An, K.H., O'Connor, B., Pipe, K. and Shtein, M., *Organic photodetector with spectral response tunable across the visible spectrum by means of internal optical microcavity*, Org. Electron. **10** (2009) 1152.

[2] An, K.H., O'Connor, B., Pipe, K., Zhao, Y. and Shtein, M., *Scanning optical probe microscopy with submicrometer resolution using an organic photodetector*, Appl. Phys. Lett. **93** (2008) 033311.

[3] An, K.H., O'Connor, B., Pipe, K., Zhao, Y. and Shtein, M., *Organic light-emitting device on a scanning probe cantilever*, Appl. Phys. Lett. **89** (2006) 111117.

[4] Andrew, P. and Barnes, W., *Energy transfer across a metal film mediated by surface plasmon polaritons*, Science **306** (2004) 1002.

[5] Antognazza, M., Scherf, U., Monti, P. and Lanzani, G., *Organic-based tristimuli colorimeter*, Appl. Phys. Lett. **90** (2007) 163509.

[6] Atwater, H., *The promise of plasmonics*, Sci. Am. **296** (2007) 56.

[7] Axelrod, D., Burghardt, T. and Thompson, N., *Total internal-reflection fluorescence*, Annu. Rev. biophys. bioeng. **13** (1984) 247.

[8] Bachelot, R., Gleyzes, P. and Boccara, A., *Reflection-mode scanning near-field optical microscopy using an apertureless metallic tip*, Appl. Opt. **36** (1997) 2160.

[9] Bachelot, R., Lerondel, G., Blaize, S., Aubert, S., Bruyant, A. and Royer, P., *Probing photonic and optoelectronic structures by apertureless scanning near-field optical microscopy*, Microsc. Res. Tech. **64** (2004) 441.

[10] Baldo, M.A. and Forrest, S., *Interface-limited injection in amorphous organic semiconductors*, Phys. Rev. B **64** (2001) 085201.

[11] Betzig, E. and Chichester, R., *Single molecules observed by near-field scanning optical microscopy*, Science **262** (1993) 1422.

[12] Betzig, E. and Trautman, J., *Near-field optics - microscopy, spectroscopy, and surface modification beyond the diffraction limit*, Science **257** (1992) 189.

[13] Betzig, E., Trautman, J., Harris, T., Weiner, J. and Kostelak, R., *Breaking the diffraction barrier - optical microscopy on a nanometric scale*, Science **251** (1991) 1468.

[14] Born, M. and Wolf, E., *Principles of optics : electromagnetic theory of propagation, interference and diffraction of light*, 1997

[15] Boroumand, F., Fry, P.W. and Lidzey, D., *Nanoscale conjugated-polymer light-emitting diodes*, Nano Lett. **5** (2005) 67.

[16] Bozhevolnyi, S., Volkov, V.S., Sondergaard, T., Boltasseva, A., Borel, P. and Kristensen, M., *Near-field imaging of light propagation in photonic crystal waveguides: Explicit role of Bloch harmonics*, Phys. Rev. B **66** (2002)

[17] Bulovic, V., Khalfin, V., Gu, G., Burrows, P., Garbuzov, D. and Forrest, S., *Weak microcavity effects in organic light-emitting devices*, Phys. Rev. B **58** (1998) 3730.

[18] Burrows, P., Zhang, Y., Haskal, E. and Forrest, S., *Observation and modeling of quasi-epitaxial growth of a crystalline organic thin-film*, Appl. Phys. Lett. **61** (1992) 2417.

[19] Cao, L. and Brongersma, M., *Ultrafast developments*, Nature Photon. **3** (2009) 12.

[20] Celebi, K., Heidel, T. and Baldo, M., *Simplified calculation of dipole energy transport in a multilayer stack using dyadic Green's functions*, Opt. Exp. **15** (2007) 1762.

[21] Chance, R.R., Prock, A. and Silbey, R., *Molecular fluorescence and energy transfer near interfaces*, Adv. Chem. Phys. **37** 1.

[22] Chanyawadee, S., Lagoudakis, P., Harley, R., Lidzey, D. and Henini, M., *Nonradiative exciton energy transfer in hybrid organic-inorganic heterostructures*, Phys. Rev. B **77** (2008)

[23] Chen, H.Y., Mcclelland, A., Chen, Z. and Lahann, J., *Solventless adhesive bonding using reactive polymer coatings*, Anal. Chem. **80** (2008) 4119.

[24] Crone, B., Davids, P., Campbell, I. and Smith, D., *Device model investigation of bilayer organic light emitting diodes*, J. App. Phys. **87** (2000) 1974.

[25] Davis, R., Williams, C. and Neuzil, P., *Optical intensity mapping on the nanometer scale by near-field photodetection optical microscopy*, Opt. Lett. **21** (1996) 447.

[26] Denyer, M., Micheletto, R., Nakajima, K., Hara, M. and Okazaki, S., *Biological imaging with a near-field optical setup*, J. Nanosci. Nanotechnol. **3** (2003) 496.

[27] Dickson, W., Stashkevitch, A., Ben Youssef, J., Takahashi, S. and Zayats, A., *SNOM imaging of thick ferromagnetic films: Image formation mechanisms and limitation*, Opt. Comm. **250** (2005) 126.

[28] Feng, J., Okamoto, T., Naraoka, R. and Kawata, S., *Enhancement of surface plasmon-mediated radiative energy transfer through a corrugated metal cathode in organic light-emitting devices,* Appl. Phys. Lett. **93** (2008)

[29] Filinski, I., *The effects of sample imperfections on optical spectra,* Phys. Status Solidi B **49** (1972) 577.

[30] Fischer, U. and Pohl, D., *Observation of single-particle plasmons by near-field optical microscopy,* Phys. Rev. Lett. **62** (1989) 458.

[31] Ford, G. and Weber, W., *Electromagnetic-interactions of molecules with metal-surfaces,* Phys. Rep. **113** (1984) 195.

[32] Forrest, S., *Ultrathin organic films grown by organic molecular beam deposition and related techniques,* Chem. Rev. **97** (1997) 1793.

[33] Gifford, D. and Hall, D., *Emission through one of two metal electrodes of an organic light-emitting diode via surface-plasmon cross coupling,* Appl. Phys. Lett. **81** (2002) 4315.

[34] Grabiec, P., Radojewski, J., Zaborowski, M., Domanski, K., Schenkel, T. and Rangelow, I., *Batch fabricated scanning near field optical microscope/atomic force microscopy microprobe integrated with piezoresistive cantilever beam with highly reproducible focused ion beam micromachined aperture,* J. Vac. Sci. Technol. B **22** (2004) 16.

[35] Heavens, O.S., *Optical properties of thin solid films,* Dover Publication, New York, 1965

[36] Hecht, B., Bielefeldt, H., Inouye, Y., Pohl, D. and Novotny, L., *Facts and artifacts in near-field optical microscopy,* J. App. Phys. **81** (1997) 2492.

[37] Hecht, B., Sick, B., Wild, U., Deckert, V., Zenobi, R., Martin, O. and Pohl, D., *Scanning near-field optical microscopy with aperture probes: Fundamentals and applications,* J. Chem. Phys. **112** (2000) 7761.

[38] Heidel, T., Mapel, J., Celebi, K., Singh, M. and Baldo, M., *Analysis of surface plasmon polariton mediated energy transfer in organic photovoltaic devices - art. no. 66560I,* Org. Photovoltaics VIII **6656** (2007) I6560.

[39] Heisig, S., Rudow, O. and Oesterschulze, E., *Scanning near-field optical microscopy in the near-infrared region using light emitting cantilever probes,* Appl. Phys. Lett. **77** (2000) 1071.

[40] Hofmann, O., Wang, X., Demello, J., Bradley, D. and Demello, A., *Towards microalbuminuria determination on a disposable diagnostic microchip with integrated fluorescence detection based on thin-film organic light emitting diodes,* Lab Chip **5** (2005) 863.

[41] Homola, J., Yee, S.S. and Gauglitz, G., *Surface plasmon resonance sensors: review*, Sen. Actuators, B **54** (1999) 3.

[42] Hoshino, K., Rozanski, L., Bout, D. and Zhang, X., *Near-field scanning optical microscopy with monolithic silicon light emitting diode on probe tip,* Appl. Phys. Lett. **92** (2008) 131106.

[43] Huang, Q., Walzer, K., Pfeiffer, M., Lyssenko, V., He, G. and Leo, K., *Highly efficient top emitting organic light-emitting diodes with organic outcoupling enhancement layers,* Appl. Phys. Lett. **88** (2006)

[44] Inouye, Y. and Kawata, S., *Near-field scanning optical microscope with a metallic probe tip,* Opt. Lett. **19** (1994) 159.

[45] Iwata, N., Wakayama, T. and Yamada, S., *Establishment of basic process to fabricate full GaAs cantilever for scanning probe microscope applications,* Sen. Actuators, A **111** (2004) 26.

[46] Kim, J.Y., Lee, K., Coates, N.E., Moses, D., Nguyen, T.-Q., Dante, M. and Heeger, A.J., *Efficient tandem polymer solar cells fabricated by all-solution processing*, Science **317** (2007) 222.

[47] Kim, K., Liu, J., Namboothiry, M.A.G., Carroll, D.L. and Email, C., *Roles of donor and acceptor nanodomains in 6% efficient thermally annealed polymer photovoltaics*, Appl. Phys. Lett. **90** (2007)

[48] Koller, D.M., Hohenau, A., Ditlbacher, H., Galler, N., Reil, F., Aussenegg, F., Leitner, A., List, E. and Krenn, J., *Organic plasmon-emitting diode*, Nature Photon. **2** (2008) 684.

[49] Kroemer, H., *Polar-on-nonpolar epitaxy*, J. Cryst. Growth **81** (1987) 193.

[50] Larosa, A., Yakobson, B. and Hallen, H., *Origins and effects of thermal-processes on near-field optical probes,* Appl. Phys. Lett. **67** (1995) 2597.

[51] Li, L., Kooi, P., Leong, M. and Yeo, T.S., *On the eigenfunction expansion of dyalic green-function in planarly stratified media*, J. Electromagn. Wave Appl. **8** (1994) 663.

[52] Loo, Y.-L., Mcculloch, I. and Email, L., *Progress and challenges in commercialization of organic electronics*, MRS Bull. **33** (2008) 653.

[53] Lupton, J., Koeppe, R., Muller, J., Feldmann, J., Scherf, U. and Lemmer, U., *Organic microcavity photodiodes*, Adv. Mat. **15** (2003) 1471.

[54] Mapel, J., Singh, M., Baldo, M. and Celebi, K., *Plasmonic excitation of organic double heterostructure solar cells,* Appl. Phys. Lett. **90** (2007)

[55] Mihalcea, C., Scholz, W., Werner, S., Munster, S., Oesterschulze, E. and Kassing, R., *Multipurpose sensor tips for scanning near-field microscopy,* Appl. Phys. Lett. **68** (1996) 3531.

[56] Miyata, N., Suzuki, T. and Ohyama, R., *Physical properties of evaporated molybdenum oxide films,* Thin Solid Films **282** (1996) 218.

[57] Morimune, T., Kam, H. and Ohmori, Y., *High-speed organic photodetectors using heterostructure with phthalocyanine and perylene derivative,* Jpn. J. Appl. Phys., Part 1 **45** (2006) 546.

[58] Mulin, D., Girard, C., Des Francs, G.C., Spajer, M. and Courjon, D., *Near-field optical probing of two-dimensional photonic crystals: theory and experiment,* J. Microsc. **202** (2001) 110.

[59] Myers, F.B. and Lee, L.P., *Innovations in optical microfluidic technologies for point-of-care diagnostics,* Lab Chip **8** (2008) 2015.

[60] Ng, T.N., Wong, W.S., Chabinyc, M.L., Sambandan, S. and Street, R.A., *Flexible image sensor array with bulk heterojunction organic photodiode,* Appl. Phys. Lett. **92** (2008) 213303.

[61] Nie, S.M. and Emery, S., *Probing single molecules and single nanoparticles by surface-enhanced Raman scattering,* Science **275** (1997) 1102.

[62] Nirupama, V., Reddy, P., Hussain, O. and Uthanna, S., *Structural and optical characterization of DC magnetron sputtered molybdenum oxide films,* Ionics **13** (2007) 451.

[63] O'Connor, B., An, K., Pipe, K., Zhao, Y. and Shtein, M., *Enhanced optical field intensity distribution in organic photovoltaic devices using external coatings,* Appl. Phys. Lett. **89** (2006) 233502.

[64] O'Connor, B., An, K., Zhao, Y., Pipe, K.P. and Shtein, M., *Fiber shaped organic light emitting device,* Adv. Mat. **19** (2007) 3897.

[65] O'Connor, B., Haughn, C., An, K., Pipe, K. and Shtein, M., *Transparent and conductive electrodes based on unpatterned, thin metal films,* Appl. Phys. Lett. **93** (2008) 223304.

[66] O'Connor, B., *Organic electronics on fibers for energy conversion applications,* Thesis, University of Michigan (2009).

[67] Okamoto, K., Niki, I., Shvartser, A., Narukawa, Y., Mukai, T. and Scherer, A., *Surface-plasmon-enhanced light emitters based on InGaN quantum wells,* Nature Mater. **3** (2004) 601.

[68] Oliver, Hofmann, Xuhua, Wang, Alastair, Cornwell, Beecher, Stephen, Amal, Raja, C, B., Donal D., J, D., Andrew and C., D., John, *Monolithically integrated*

dye-doped PDMS long-pass filters for disposable on-chip fluorescence detection, Lab Chip **6** (2006) 981.

[69] Oyamada, T., Sugawara, Y., Terao, Y., Sasabe, H. and Adachi, C., *Top light-harvesting organic solar cell using ultrathin Ag/MgAg layer as anode*, Jpn. J. Appl. Phys., Part 1 **46** (2007) 1734.

[70] Ozbay, E., *Plasmonics: Merging photonics and electronics at nanoscale dimensions*, Science **311** (2006) 189.

[71] Pais, A., Banerjee, A., Klotzkin, D. and Papautsky, I., *High-sensitivity, disposable lab-on-a-chip with thin-film organic electronics for fluorescence detection*, Lab Chip **8** (2008) 794.

[72] Palik, D. and Ghosh, G., *Handbook of optical constants of solids*, Academic Press, 1985

[73] Pettersson, L., Roman, L. and Inganas, O., *Modeling photocurrent action spectra of photovoltaic devices based on organic thin films*, J. App. Phys. **86** (1999) 487.

[74] Peumans, P., Bulovic, V. and Forrest, S., *Efficient, high-bandwidth organic multilayer photodetectors*, Appl. Phys. Lett. **76** (2000) 3855.

[75] Peumans, P. and Forrest, S., *Very-high-efficiency double-heterostructure copper phthalocyanine/C-60 photovoltaic cells*, Appl. Phys. Lett. **79** (2001) 126.

[76] Peumans, P. and Forrest, S., *Separation of geminate charge-pairs at donor-acceptor interfaces in disordered solids*, Chem. Phys. Lett. **398** (2004) 27.

[77] Peumans, P., Uchida, S. and Forrest, S., *Efficient bulk heterojunction photovoltaic cells using small-molecular-weight organic thin films*, Nature **425** (2003) 158.

[78] Peumans, P., Yakimov, A. and Forrest, S., *Small molecular weight organic thin-film photodetectors and solar cells*, J. App. Phys. **93** (2003) 3693.

[79] Pope, M. and Swenberg, C., *Electronic processes in organic crystals*, Oxford university press, New York, 1982

[80] Ramuz, M., Buergi, L., Winnewisser, C. and Seitz, P., *High sensitivity organic photodiodes with low dark currents and increased lifetimes*, Org. Electron. **9** (2008) 369.

[81] Rand, B., Peumans, P. and Forrest, S., *Long-range absorption enhancement in organic tandem thin-film solar cells containing silver nanoclusters*, J. App. Phys. **96** (2004) 7519.

[82] Reineke, S., Lindner, F., Schwartz, G., Seidler, N., Walzer, K., Lussem, B. and Leo, K., *White organic light-emitting diodes with fluorescent tube efficiency*, Nature **459** (2009) 234.

[83] Riel, H., Karg, S., Beierlein, T., Riess, W. and Neyts, K., *Tuning the emission characteristics of top-emitting organic light-emitting devices by means of a dielectric capping layer: An experimental and theoretical study*, J. App. Phys. **94** (2003) 5290.

[84] Rothenhausler, B. and Knoll, W., *Surface-plasmon microscopy,* Nature **332** (1988) 615.

[85] Ruhstaller, B., Carter, S.A., Barth, S., Riel, H., Riess, W. and Scott, J., *Transient and steady-state behavior of space charges in multilayer organic light-emitting diodes*, J. App. Phys. **89** (2001) 4575.

[86] Saricifici, N., Smilowitz, L., Heeger, A. and Wudl, F., *Photoinduced electron-transfer from a conducting polymer to buckminsterfullerene,* Science **258** (1992) 1474.

[87] Sasaki, M., Tanaka, K. and Hane, K., *Cantilever probe integrated with light-emitting diode, waveguide, aperture, and photodiode for scanning near-field optical microscope,* Jpn. J. Appl. Phys., Part 1 **39** (2000) 7150.

[88] Scharfetter, D.L. and Gummel, H.K., *Large-signal analysis of a silicon Read diode oscillator,* IEEE Trans. Electron Devices **16** (1969) 64.

[89] Schubert, E.F., Refractive index and extinction coefficient of materials (http://www.rpi.edu/~schubert/)

[90] Scott, J.C. and Malliaras, G., *Charge injection and recombination at the metal-organic interface*, Chem. Phys. Lett. **299** (1999) 115.

[91] Seo, H., Aihara, S., Watabe, T., Ohtake, H., Kubota, M. and Egami, N., *Color sensors with three vertically stacked organic photodetectors,* Jpn. J. Appl. Phys., Part 2 **46** (2007) L1240.

[92] Shao, Y. and Yang, Y., *Efficient organic heterojunction photovoltaic cells based on triplet materials,* Adv. Mat. **17** (2005) 2841.

[93] Shiba, H., Haraguchi, M. and Fukui, M., *Propagation length of surface-plasmon polaritons propagating along air metal interface,* J. Phys. Soc. Jpn. **63** (1994) 1400.

[94] Shoustikov, A., You, Y.J. and Thompson, M., *Electroluminescence color tuning by dye doping in organic light-emitting diodes*, IEEE J. Sel. Top. Quantum Electron. **4** (1998) 3.

[95] Smolyaninov, I., I, Elliott, J., Zayats, A., V and Davis, C., C, *Far-field optical microscopy with a nanometer-scale resolution based on the in-plane image magnification by surface plasmon polaritons*, Phys. Rev. Lett. **94** (2005)

[96] Stahelin, M., Bopp, M., Tarrach, G., Meixner, A. and Zschokkegranacher, I., *Temperature profile of fiber tips used in scanning near-field optical microscopy*, Appl. Phys. Lett. **68** (1996) 2603.

[97] Suh, D. and Lee, H.H., *Sub-100 nm organic light-emitting diodes patterned with room temperature imprint lithography*, J. Vac. Sci. Technol. B **22** (2004) 1123.

[98] S.M. Sze, *Physics of semiconductor devices (2nd Edition)*, John Wiley and Sons, New York, 1981

[99] Tang, C., *2-layer organic photovoltaic cell*, Appl. Phys. Lett. **48** (1986) 183.

[100] Tang, C. and Vanslyke, S., *Organic electroluminescent diodes*, Appl. Phys. Lett. **51** (1987) 913.

[101] Wakamatsu, T., Saito, K., Sakakibara, Y. and Yokoyama, H., *Enhanced photocurrent in organic photoelectric cells based on surface-plasmon excitations*, Jpn. J. Appl. Phys., Part 2 **34** (1995) L1467.

[102] Wang, A., Kymissis, I., Bulovic, V. and Akinwande, A., *Engineering density of semiconductor-dielectric interface states to modulate threshold voltage in OFETs*, IEEE Trans. Electron Devices **53** (2006) 9.

[103] Wasey, J. and Barnes, W., *Efficiency of spontaneous emission from planar microcavities*, J. Mod. Opt. **47** (2000) 725.

[104] Wedge, S., Hooper, I.R., Sage, I. and Barnes, W., *Light emission through a corrugated metal film: The role of cross-coupled surface plasmon polaritons*, Phys. Rev. B **69** (2004)

[105] Xin, Xu, Marcelo, Davanco, Xiangfei, Qi and R., F., Stephen, *Direct transfer patterning on three dimensionally deformed surfaces at micrometer resolutions and its application to hemispherical focal plane detector arrays*, Org. Electron. **9** (2008) 1122.

[106] Xue, J.G., Uchida, S., Rand, B., Forrest, S. and Email, f., *Asymmetric tandem organic photovoltaic cells with hybrid planar-mixed molecular heterojunctions*, Appl. Phys. Lett. **85** (2004) 5757.

[107] Yamamoto, H., Wilkinson, J., Long, J., Bussman, K., Christodoulides, J.A. and Kafafi, Z., *Nanoscale organic light-emitting diodes*, Nano Lett. **5** (2005) 2485.

[108] Yao, B., Luo, G., Wang, L., Gao, Y.D., Lei, G.T., Ren, K., Chen, L., Wang, Y., Hu, Y. and Qiu, Y., *A microfluidic device using a green organic light emitting diode as an integrated excitation source*, Lab Chip **5** (2005) 1041.

[109] Zenhausern, F., Oboyle, M.P. and Wickramasinghe, H., *Apertureless near-field optical microscope*, Appl. Phys. Lett. **65** (1994) 1623.

[110] Zhao, Y., An, K., Chen, S., O'connor, B., Pipe, K. and Shtein, M., *Localized current injection and submicron organic light-emitting device on a pyramidal atomic force microscopy tip*, Nano Lett. **7** (2007) 3645.

[111] Zia, R., Selker, M. and Brongersma, M., *Leaky and bound modes of surface plasmon waveguides*, Phys. Rev. B **71** (2005) 165431.

[112] An, K.H., Pipe, K. and Shtein, M., *Electrically-pumped excitonic energy transfer across a metal film mediated by surface plasmon polaritons*, In preparation.

[113] An, K.H., Pipe, K. and Shtein, M., *High-resolution (50 nm) scanning optical microscopy based on organic photodetector*, In preparation